Laser Slowing of CaF Molecules and Progress towards a Dual-MOT for Li and CaF

A dissertation presented

by

Eunmi Chae

to

The Department of Physics

in partial fulfillment of the requirements

for the degree of

Doctor of Philosophy

in the subject of

Physics

Harvard University

Cambridge, Massachusetts

November 2015

Dissertation advisor

Prof. John M. Doyle and Prof. Wolfgang Ketterle

Author

Eunmi Chae

Laser Slowing of CaF Molecules and Progress towards a Dual-MOT for Li and CaF

Abstract

Diatomic molecules are considered good candidates for the study of strongly correlated systems and precision measurement searches due to their combination of complex internal states and strong long-range interactions. Cooling molecules down to ultracold temperatures is often a necessary step for fully utilizing the power of the molecule. This requires a trap for molecules and the ability to cool molecules to the mK regime and below. A magneto-optical trap (MOT) is a good tool for achieving mK temperatures. However, extra care is needed for molecules to form the necessary quasi-closed cycling transitions due to molecule's complicated energy structure. In our work with CaF, we use two repump lasers to block vibrational leakage and selection rules for the rotational degree of freedom to achieve about 10^5 photon cycles.

The two-stage buffer gas beam source is a general method to generate a cold and slow beam of molecules with a forward velocity of about 50 m/s. The compatibility of the buffer-gas source with a MOT is studied and we confirm that such beams can be nicely compatible with MOTs using various atomic species.

In order to load *molecules* into a MOT from even such a slow beam, additional slowing is required due to the low capture velocity of a molecular MOT (< 10 m/s). We apply a frequency-broadened "white-light" slowing on CaF from a two-stage source, demonstrating slowing of CaF below 10 m/s. An AC MOT, which provides active remixing of dark substates, is also developed and Li atoms are slowed and trapped. These are crucial ingredients for

co-trapping CaF molecules and Li atoms and study their collisional properties, which would lead to sympathetic cooling of molecules down to ultracold temperatures.

The achievement of slowing and development of this system allowed for the detailed study of the CaF laser cooling system, as well as physical processes involved with AC MOTs and the proposed MOT for CaF. Crucial knowledge of this archetypal system provides significant progress toward manipulation and control of molecules similar to what has been achieved with atoms and what is necessary for searches for new physics with ultracold molecules.

Contents

Citations to previously pulished work

Parts of this dissertaion have reported in the following paper.

- *Buffer-gas loaded magneto-optical traps for Yb, Tm, Er and Ho.* B. Hemmerling, G. K. Drayna, E. Chae, A. Ravi, and J. M. Doyle. New Journal of Physics **16**, 063070 (2014).

Acknowledgments

I would like to first thank my advisors Prof. John M. Doyle and Prof. Wolfgang Ketterle for their guide throughout my days in the lab. John provided everything that a graduate student needs - patience to wait a slow student like me, appropriate advices whenever I needed, right decisions at the right timings, great lab environment, etc. Without his guidance, I would not be able to finish my thesis work. Wolfgang always gave great comments about the experiment when I struggled. His insight helped me a lot to overcome a lot of difficulties during the experiment.

I appreciate Prof. Markus Greiner and Prof. Matthew D. Schwartz for kindly accepting my request to be my committee. They were ready to help me out regarding my research and my life in the graduate school. They asked great questions so that I could learn more about my research as I explained to them about it.

Colin and Yat taught me tremendous things from general Physics topics to miscellaneous properties of materials. They helped me settle in the lab as well and gave various advices regarding the graduate student life.

Laser coolers - Boerge, Aakash, Loic, Ben, Garrett, and Nick -, It is inexpressible how much I thank them for everything. We spent most of the time together in the lab, day and night, learning and teaching each other. I grew as a researcher thanks to them and my best hope is that I would share what I have earned here wherever I go.

I also thank other Doylies. They provided everything - from an expensive equipment to daily snacks - whenever I needed. I learned and laughed a lot with them. The time spent with all of the Doylies is one of my precious moments in my life.

The engineering staff members - Stan, Steve, Jim, and Al - taught me essential skills needed as an experimental physicist. We are blessed that we have these wonderful staff members when we need them. Their technical knowledge is priceless and saved a lot of time during my research. Jan, Sheila, Lisa, and Silke allowed me concentrating on my research and took care of all the annoying paper work and I would like to thank them for their

amazing help.

Meeting with my Korean friends in Physics - Junhyun, Yejin, Jungook, and Jaehoon - was my best break-time outside of the lab. Having friends with similar concerns has been great help to live through some hard moments. I also appreciate my church friends to distract me from Physics.

Finally, I would like to thank Eun-Gook, my husband. Throughout the entire period here, he encouraged and supported me as a partner as well as a mentor. His earnestness and passion for Physics also have been a good lesson for me.

To my family

Chapter 1

Introduction

In this thesis, MOTs for various atoms (Yb, Tm, Er, and Ho) are directly loaded from the slow buffer-gas beam source, confirming the low forward velocity of the beam and the compatibility of the buffer-gas beam source with a MOT. Also, laser slowing of CaF molecules down to the capture velocity of an AC MOT for CaF (about 10 m/s) and an AC MOT for Li atoms are achieved, paving the way towards collisional studies of CaF molecules and Li atoms in a trap. The effects of the various internal rotational and vibrational states on photon cycling are studied and understood, shedding light on the intricacies of laser cooling of diatomic molecules, in particular the archetypal case of CaF. These are the fundamental steps toward studying ultracold collisions in the CaF-Li system loaded from a MOT, as well as the CaF-CaF system. Ultimately, if the Li-CaF properties are good, then high phase space density ultracold gases of CaF should be possible through sympathetic cooling with Li atoms. In this chapter, a brief description of the purpose of cold and ultracold molecular studies, various strategies toward ultracold regime, and current status of research in the field are summarized.

1.1 Why ultracold molecules?

Since the achievement of the first atomic BECs in 1995 [1, 2], there has been a tremendous amount of research using ultracold atoms to explore new physical systems, including quantum simulation of condensed matter system, thermodynamics of mesoscopic ensembles, quantum information, and precision measurements [3–6]. Part of the utility of ultracold atomic gases is due to their relative simplicity and the controllability of atomic systems compared to solid-state systems. Surprisingly, atoms with the simplest internal structure give rich Hamiltonians to play with. By changing the interaction strength using Feshbach resonances, putting atoms in lattices with different height and geometries, applying external fields, and even rotating the whole cloud [7–11], a host of new phenomena were studied, as well as the creation of tunable archetypal systems that were originally discovered in liquid or solid systems.

However, atoms have some limitations due to their simple structure. Even with the exceptional tunability of the strength of the interaction between atoms, it is dominated by the short-range contact interactions in nearly all systems studied so far. A strong, long-range interaction is a possible key to opening the door to a plethora of extensions to condensed matter physics and also an important ingredient for quantum information. A few atoms have high magnetic moments, but the magnetic dipole-dipole interaction strength is still similar to or weaker than the contact interaction strength [12, 13]. Rydberg atoms have strong dipole-dipole interaction which makes them as a strong candidate for quantum information [5], but their limited lifetime and density due to Rydberg blockade is a limitation.

Diatomic molecules have more internal degrees of freedom - rotations and vibrations - and their electric moments could open a way to overcome these challenges. If we can achieve same controllability of diatomic molecules as we have achieved with atoms, and utilize their additional properties, the physics we can explore would expand incredibly. Also, molecules provide the richness for chemical reactions. By putting the molecules in a single quantum state at ultracold temperature, a controlled study of chemistry can be conducted. Many proposals and experiments have been made regarding manipulating diatomic polar molecules

[14] for quantum simulation with long-range interaction [15–17], quantum information [18–20], precision measurements [21, 22], and controlled chemistry [23–25].

1.2 The way to ultracold molecules

Of course, nothing comes for free. There are two major challenges when working with diatomic molecules. Production and cooling of the molecules must be realized. This is relatively simple with atoms since an oven with reasonable operating temperatures (usually a few hundreds of Kelvin) produces enough flux of atoms in a single or just a few internal quantum states. In particular, thanks to the simple energy structure, all the generated atoms are in the electronic ground state with, perhaps, hyperfine structure. All one needs to do is cool the translational temperature, which is now simple for atoms since one can apply laser cooling with only one or no repump lasers. After sufficient cooling, one can trap the atoms in various traps and start further cooling using evaporative or sympathetic cooling.

Diatomic molecules that are interesting to study are, on the other hand, radicals and producing them using an oven requires temperatures well above a thousand Kelvin. At this high temperature, thousands of rotational and vibrational quantum states are populated, as well as producing a velocity profile with high translational temperature. To achieve high phase density in a single internal quantum state, one needs to cool the vibrational, rotational, and the translational temperatures all together, which is challenging.

There are two ways to overcome these challenge. One is taking advantage of simplicity of atoms and combining two ultracold atoms to generate a ultracold molecule (indirect method). The other is starting with the molecular beam which is already cold and further cooling them (direct method).

1.2.1 Indirect methods

The generation of the ground state molecules by combining two ultracold atoms was first realized with KRb molecules [26]. In that experiment, two nearby ultracold atoms of ^{40}K and ^{87}Rb were transferred to the ground state of the molecular potential via stimulated Raman adiabatic passage (STIRAP), reaching the peak density of 10^{12} cm^{-3} with the temperature of 350 nK. The molecules have been loaded to optical lattices to suppress the chemical reaction and were used to study dipole-dipole interactions in the lattice system [27]. In recent experiments, authors improved the filling factor in the lattice up to 25 % [28]. The ground state molecules of NaK and RbCs have been realized using similar methods recently [29, 30].

This approach has been a great success, starting to study dipolar physics with ultracold molecules. This method, however, is limited to a handful number of molecular species since one first needs ultracold atoms, easily achievable with only the metals, and only a few at that. To take advantage of the diversity of molecular species, a general method to cool the molecules is desired.

1.2.2 Direct methods

1.2.2.1 Production of molecules and initial cooling down to ~ K regime

One can approach from the other direction - generate the molecule you want first, and cool them down later. Ablation, where a high energy pulsed laser hits a solid precursor target to generate molecules, is a common method to produce radicals with a good amount of flux. The generated molecules are at very high temperatures of several hundreds up to a thousand Kelvin and a cooling mechanism is necessary to have good amount of usable molecules before they are lost.

Traditionally, supersonic jets have been used to produce internally cold beams of radicals, with the rotational temperature about 1 K, but the packet of molecules moves in the lab

frame with forward velocities of several hundreds m/s, which is hard but not impossible to slow down by Stark deceleration and trap [31–34]. Unlike atoms, Zeeman slower is not practical for molecules due to their complex internal energy states.

The buffer-gas beam, which is used throughout this experiment, uses elastic collisions with cold inert gas (buffer-gas) at 4 K (He as buffer-gas) or 15 K (Ne as buffer-gas) to cool the molecules rotationally and translationally down to several Kelvin in ms time scale with high flux. This gives an excellent starting point of the experiment with a peak forward velocity of about 60 - 200 m/s and flux of $10^9 - 10^{13}$ sr^{-1} per state per pulse, depending of the molecular species and the cell geometry [35]. Trapping molecules inside a magnetic trap directly from the slow buffer-gas beam source has been realized recently [36]. The slow beam of lanthanide atoms also has been directly loaded to magneto-optical traps without further slowing [37]. The generality of the buffer-gas source allowed us to make MOTs for several different species by only tuning the MOT laser frequency. Co-trapping different species would not be a difficult task for the buffer-gas beam source, which makes this source a strong candidate to study collisions between molecules and atoms.

1.2.2.2 Trapping : Bridge between cold and ultracold

To reach ultracold temperatures, the molecules need to be trapped so that they can be evaporatively or sympathetically cooled. Considering molecules' low flux compared to atoms and possible chemical reactions and increased inelastic collisions among molecules, sympathetic cooling of molecules with atoms could be a good strategy once one finds a good collisional partner for the molecules. Recent theoretical calculations makes one optimistic about this approach [38, 39].

Trapping molecules in an electric/magnetic trap has been demonstrated with various species of molecules using their electric/magnetic dipole moments. Metastable NH molecules [32], OH molecules [40], and CH_3F molecules [41] have been trapped in an electric trap, with temperatures around 50 - 500 mK. More species have been trapped in a magnetic trap.

NH molecules [31, 42, 43], CaH molecules [44], CrH and MnH molecules [45], OH molecules [46, 47], and CaF molecules [36]. Among these, authors have demonstrated evaporative cooling only of OH molecules in the magnetic trap, reaching temperatures of 5 mK [47]. There is also a proposal to trap polar molecules in a microwave trap [48].

Magneto-optical trap (MOT) Unlike the conservative traps mentioned above, a magneto-optical trap (MOT) is a dissipative trap where the particle's energy is being removed continuously in the trap. In principle, this is an effective first step to grab particles that are flying by the area, unlike the conservative traps which would let them just go through. The MOT will also cool them so that they remain in the trap. In atomic experiments, MOTs are used right after a Zeeman slower for the initial trapping of atoms. After the MOT, atoms are transferred to a conservative trap - magnetic or dipole trap - and are further cooled there by evaporative or sympathetic cooling. From natural expansion from the atomic world, molecular MOTs were proposed [49].

However, there is a big challenge to make a MOT for molecules - finding a strong closed optical transition. With the large number of rotational and vibrational states, it is impossible to find a simple closed transition for molecules. Nevertheless, people have found a number of molecules that can cycle reasonable number of photons with a few repump lasers [50]. After demonstrating optical cycling [51], transverse cooling [52, 53], and longitudinal slowing of diatomic molecules with lasers [54–56], finally a MOT for SrF molecules was achieved recently, demonstrating temperature down to 400 μK [57–59], paving a way towards ultracold molecules for certain selected species. However, not only can we use such species to do new physics, it is also likely that this initial step will lead to unforeseen improvements in a suite of techniques to bring, perhaps, any molecule into the ultracold regime. Extending these basic methods to the lighter, archetypal CaF system would be an important step toward mastery of molecules in general.

1.2.2.3 Collisional studies

Once molecules are trapped in the MOT, a fruitful approach to further cooling and phase space compression is to load them into a conservative trap. Finding a good atomic collisional partner would be the most promising way. However, calculating collision properties between an atom and a molecule at this temperature regime (around mK down to μK) is a quite challenging task since the potentials are not well know and one needs to include many quantum states for the calculation. As a result, only a handful of cases have been studied theoretically [38, 39, 43, 60, 61]. There are quantitative studies underway for the CaF-Li systems and initial results look promising. Also, there are several experimental results, many from the Doyle lab, that include collisions with He and in one case with N atoms [43], and CaH + Li from the Weinstein lab [62]. Although not fully developed, there is an overall sense that sympathetic cooling is a promising approach.

1.3 Summary of the experiments in this thesis

In this thesis, we pursue a direct method to produce ultracold molecules. Our target species are CaF molecules and Li atoms due to their excellent electronic and vibrational energy state properties, and enough flux out of our source. We use a buffer-gas beam source which produce a slow beam of CaF molecules with the forward velocity at around 50 m/s as our starting point. We demonstrate MOTs for Yb, Tm, Er, and Ho atoms directly loaded from the buffer-gas beam source. This achievement confirms the slow forward velocity of the source and the compatibility of the buffer-gas technique with a MOT. To load the molecules into a magneto-optical trap, we slow the molecules below 10 m/s using frequency-broadened lasers counter-propagating to the molecular beam. We develop an AC MOT for co-trapping the CaF molecules and atoms, and successfully slow and trap ^{6}Li atoms in it. We can co-trap the CaF molecules in the near future to study their collisional properties.

Chapter 2

Molecular Structure and Properties of CaF Molecules and ^{6}Li Atoms

Diatomic molecules have additional internal degrees of freedom compared to atoms - rotations and vibrations. These give new quantum numbers to the system. Also, there is a new symmetry with respect to the molecular axis which connects the two nuclei. Due to this new symmetry, all angular momentums should be divided into two components - along the molecular axis and perpendicular to the molecular axis - and the two components should be treated separately. Depending on how strong the electron's orbital and spin angular momentum couple to the molecular axis, one can group molecular states into about 5 groups (Hund's cases). In this chapter, a brief description about molecular structures and the properties of a CaF molecule and a ^{6}Li atoms are summarized.

2.1 Brief summary of the structure of diatomic molecules

Here, we follow the conventions in Ref. [63].

2.1.1 Additional degrees of freedom - vibration and rotation

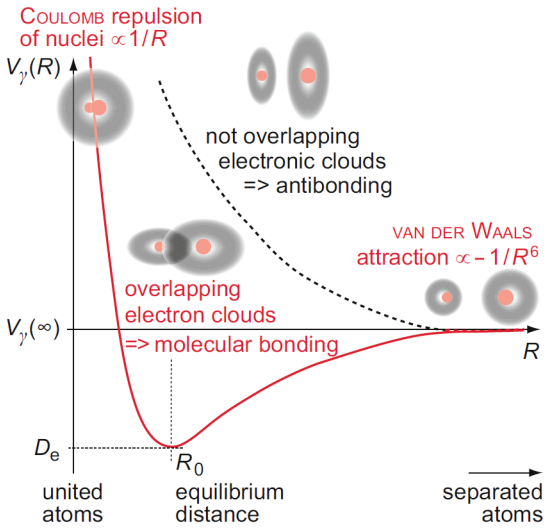

Figure 2.1.1: Molecular potential as a function of nuclei distance. Figure taken from Fig. 3.4. in Ref. [64].

Vibration Using Born-Oppenheimer approximation, we can separate the electron's motion and the nuclei's motion since the nuclei is a lot heavier than the electron. The bounding energy for a diatomic molecule is a function of the distance between the two nuclei and has a minimum at the equilibrium distance (Fig. 2.1.1). Near the minimum of the potential, it can be approximated as a harmonic potential and the vibrational energy levels can be described as eigenstates of the harmonic potential

$$E_v = \omega_e(v + \frac{1}{2}) \tag{2.1.1}$$

, where v is the vibrational quantum number.

The real molecules are anharmonic oscillators and the higher order terms are needed to describe the vibrational energy more accurately.

$$E_v = \omega_e(v + \frac{1}{2}) - \omega_e x_e(v + \frac{1}{2})^2 + \omega_e y_e(v + \frac{1}{2})^3 + ... \tag{2.1.2}$$

In most of the cases, T_e indicates the energy at the bottom of the potential (indicated as D_e in Fig. 2.1.1). T_0 is the energy of the molecule with the vibrational zero mode energy. Therefore, $T_0 = T_e + \frac{1}{2}\omega_e - \frac{1}{4}\omega_e x_e + \frac{1}{8}\omega_e y_e + ...$ Some literatures use ΔG to indicate the energy spacing between adjacent vibrational levels.

Each electronic state has a set of vibrational states and the wavefunction overlap squared $|\langle\psi_{v'}|\psi_{v''}\rangle|^2$ is called Franck-Condon factor. This factor is a key for selecting molecules that could be easier to be laser cooled.

Rotation The rotation of a diatomic molecule can be approximated as a rigid rotor.

$$H_R = B \cdot \mathbf{R}^2 \tag{2.1.3}$$

$$E_R = B\,R(R+1) \tag{2.1.4}$$

$$= \quad B_v R(R+1) - D_v R^2(R+1)^2 + H_v R^3(R+1)^3 + ... \tag{2.1.5}$$

R is the quantum number for the nuclei rotation. Each constant above depends on the vibrational quantum number v.

$$B_v = B_e - \alpha_e(v+\frac{1}{2}) + \gamma_e(v+\frac{1}{2})^2 + ... \tag{2.1.6}$$

$$D_v = D_e + \beta_e(v+\frac{1}{2}) + ... \tag{2.1.7}$$

Dunham notation Combining the vibration and the rotation degrees of freedom, Dunham showed that the rovibrational energy could be expressed as a double power series [65].

$$E = \sum_{kl} Y_{kl}(v+\frac{1}{2})^k [R(R+1)]^l \tag{2.1.8}$$

The Dunham coefficients and the standard spectroscopic parameters are very closely related to each other as

$$Y_{10} \approx \omega_e,\ Y_{20} \approx -\omega_e x_e,\ Y_{01} \approx B_e,\ Y_{02} \approx -D_e,\ Y_{11} \approx -\alpha_e,\ Y_{21} \approx \gamma_e\ Y_{12} \approx -\beta_e \tag{2.1.9}$$

.

2.1.2 Quantum numbers and state notations

Quantum numbers In diatomic molecules, quantum numbers explained below are used to define a state.

- **v** : vibration of the bare nuclei
- **R** : rotational angular momentum of the bare nuclei

- $\mathbf{L}$: electronic orbital angular momentum
- $\mathbf{S}$: electronic spin angular momentum
- $\mathbf{I}$: nuclear spin angular momentum
- $\mathbf{J}_a = \mathbf{L} + \mathbf{S}$: total electronic angular momentum
- $\mathbf{J}$: total angular momentum except nuclear spin
- $\mathbf{N} = \mathbf{J} - \mathbf{S}$: rotation + electronic angular momentum
- $\mathbf{F} = \mathbf{J} + \mathbf{I}$: total angular momentum including hyperfine interaction

The vibrational levels of diatomic molecules can be approximated using energy levels of a harmonic potential. The coupling between $\mathbf{v}$ and $\mathbf{R}$ has taken into account as vibrational level dependent rotational constant B. The coupling between the vibration and and other angular momentum except $\mathbf{R}$ is quite small compared to other energy scales and we ignore them here.

Each angular momentum can couple to each other via various interactions and below are the possible interactions and their names.

- $\mathbf{L}$ and $\mathbf{S}$: spin-orbit coupling (coupling constant A)
- $\mathbf{L}$ and $\mathbf{R}$: rotational electronic interaction
- $\mathbf{L}$ and $\mathbf{I}$: hyperfine interaction between the electron orbital and nuclear spin magnetic moment
- $\mathbf{S}$ and $\mathbf{I}$: hyperfine interaction between the electron and nuclear spin magnetic moments
- $\mathbf{S}$ and $\mathbf{R}$: interaction between electron spin and rotational magnetic moment
- $\mathbf{I}$ and $\mathbf{R}$: interaction between nuclear spin and rotational magnetic moment

Also, electronic orbital angular momentum couples to the internuclear axis (strength denoted as ΔE_{el}). When the coupling is strong, the projection of the angular momentum onto the internuclear axis is conserved and is a good quantum number. When the coupling is weak, the angular momentum and the internuclear axis can move independently and the projection of the angular momentum onto the internuclear axis is not conserved anymore. Depending on the strength of the coupling among each angular momentum, we can define groups of molecules which are summarized in the next subsection.

The projection onto the internuclear axis for each angular momentum is named as follows. The nuclear spin coupling to the internuclear axis is not considered here since its energy scale is a lot smaller than others. The nuclei rotation $\mathbf{R}$ is by definition always perpendicular to the internuclear axis for diatomic molecules.

- Λ : Projection of $\mathbf{L}$ onto the internuclear axis
- Σ : Projection of $\mathbf{S}$ onto the internuclear axis
- Ω : Projection of $\mathbf{J}$ onto the internuclear axis

State notations The notations for energy levels of molecules are quite different than the ones for atoms. Some of the frequently used ones are summarized here.

The name of the ground state is usually denoted as X. The excited singlet states are named using capital letters as A, B, C, $D, ...$ from the lowest energy. The excited triplet states are named using lower cases as a, b, c, $d, ...$ from the lowest energy.

The quantum numbers describing a certain states are denoted in a similar way to atoms, where one writes ${}^{2S+1}L_J$ (S, P, D, $F, ...$ for $L = 0, 1, 2, 3, ...$). For diatomic molecules we deal with here, the electron's angular momentum is strongly coupled to the internuclei axis so that the projection Λ is a good quantum number instead of L. Therefore, the states are labeled as ${}^{2S+1}\Lambda$ (Σ, Π, Δ, $\Phi, ...$ for $\Lambda = 0, 1, 2, 3, ...$). Note that Σ here is different from the projection of electron spin $\mathbf{S}$ onto the molecular axis which is also denoted as Σ. When

Ωis a good quantum number, like Hund's case (a) which is described in the next subsection, the states are denoted as ${}^{2S+1}\Lambda_\Omega$.

Molecular fixed frame VS Lab fixed frame Unlike atoms, who do not have a particular axis in itself and spatially symmetric around its center, diatomic molecules have a symmetry breaking axis - internuclear axis. When dealing with the molecular energy structure, it is convenient to use molecule-fixed axis (molecular frame) where the nuclei are positioned in a fixed position. On the other hand, it is good to use space-fixed coordinates (lab frame) when the molecule interacts with the external environment. Usually, capital letters X, Y, Z are used to indicate lab frame coordinates and small letters x, y, z are used for molecular frame. The spherical operator for a Hamiltonian is expressed with the element label p in the lab frame like$\mathrm{T}^k_p(\mathbf{A})$ and with element label q in the molecular frame ($\mathrm{T}^k_q(\mathbf{A})$). The transformation between different frames is expressed as below using rotation matrix $\mathfrak{D}^{(k)}_{pq}(\omega)$.

$$\mathrm{T}^k_p(\mathbf{A}) = \sum_q \mathfrak{D}^{(k)}_{pq}(\omega) * \mathrm{T}^k_q(\mathbf{A}) \tag{2.1.10}$$

, where ω indicates the Euler angles between the space-fixed coordinates and the molecule-fixed coordinates.

The projection of a certain angular momentum onto the molecular axis is named using Greek letters Λ, Σ, Ω, ..., where the projection onto the space-fixed Z direction is named as M_L, M_S, M_J, ...

2.1.3 Hund's cases

When we think about the eigenstates of a certain system, it is convenient to first consider the stronger energy scales and weaker ones later. Depending on the relative coupling strength, diatomic molecules are grouped into 5 classes by Friedrich Hund,[66] and the classification is called Hund's cases. The good quantum numbers and the requirements for each class are summarized in Table 2.1. Hund's case (a) and Hund's case (b) are the most common cases

Coupling cases	Good quantum numbers	Requirements
(a)	η, Λ, S, Σ, J, Ω	$\Delta E_{el} \gg A\,\Lambda \gg B\,J$
(b)	η, Λ, N, S, J	$\Delta E_{el} \gg B\,J \gg A\,\Lambda$
(c)	η, (J_a), Ω, J	$A\,\Lambda > B\,J \gg \Delta E_{el}$
(d)	η, L, R, N, S, J	$B\,J > A\,\Lambda \gg \Delta E_{el}$
(e)	η, J_a, R, J	$A\,\Lambda \gg B\,J \gg \Delta E_{el}$

Table 2.1: Hund's coupling cases adopted from Ref. [63]. η indicates all quantum numbers that are not specified, like electronic and vibrational ones.

and the relevant ones for the states of CaF molecules that we treat here. For other cases, Ref. [63] has a good summary.

2.1.3.1 Hund's case (a)

Hund's case (a) is a good case when the strong electrostatic force fixes the projection of the electronic orbital angular momentum onto the molecular axis and the spin-orbit coupling is much stronger than the nuclei rotational energy. Therefore, we should consider coupling of $\mathbf{L}$ onto the internuclear axis first, spin-orbit coupling next, and nuclei rotational angular momentum later. This is a good representative for the CaF first electronic excited state $A\,^2\Pi$.

In this case, the electronic orbital momentum ($\mathbf{L}$) is strongly coupled to the internuclear axis by electrostatic forces and the projection of $\mathbf{L}$ onto the molecular axis (Λ) is well defined. Also, the electron spin momentum $\mathbf{S}$ is strongly couple to $\mathbf{L}$ via spin-orbit coupling and the projection of $\mathbf{S}$ onto the molecular axis(Σ) is also well defined. As a consequence, the sum $\Omega = \Lambda + \Sigma$ is a good quantum number. The total angular momentum except the nuclear spin ($\mathbf{J}$) is the sum of the nuclei rotation $\mathbf{R}$ and $\mathbf{\Omega}$, which is a vector point along the molecular axis with the amplitude Ω. The lowest value that $\mathbf{J}$ can have is Ω. This case is also called as "decoupled basis" since $\mathbf{L}$ and $\mathbf{S}$ are decoupled along the molecular axis.

Rotational energy in Hund's case (a) The rotational Hamiltonian can be written as follows using good quantum numbers.

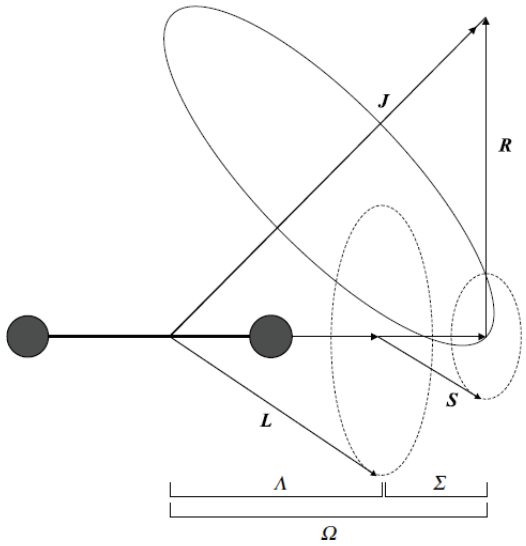

Figure 2.1.2: Angular momentum coupling in Hund's case (a) from Ref. [63]

$$
\begin{aligned}
H_{rot} &= B\,\mathbf{R}^2 \\
&= B\,(\mathbf{J}-\mathbf{\Omega})^2 \\
&= B\,(\mathbf{J}^2+\mathbf{\Omega}^2-2\mathbf{J}\cdot\mathbf{\Omega}) \\
&= B\,(\mathbf{J}^2-\mathbf{\Omega}^2) \\
&= B\,(J(J+1)-\Omega(\Omega-1)) \qquad (2.1.11)
\end{aligned}
$$

Here we use $\mathbf{J}\cdot\mathbf{\Omega}=\mathbf{\Omega}^2$ by the definition of $\mathbf{J}$. The rotational energy changes with the value of J.

Λ doubling in Hund's case (a) molecules When $|\Lambda|\neq 0$, the Λ can be either positive or negative, and same for Σ and Ω. The eigenstates of the parity operator are formed therefore as

$$
\begin{aligned}
|+\rangle &= \frac{1}{\sqrt{2}}\left(|+|\Lambda|,+|\Sigma|,+|\Omega|\rangle+(-1)^{J-S}|-|\Lambda|,-|\Sigma|,-|\Omega|\rangle\right) \qquad (2.1.12)\\
|-\rangle &= \frac{1}{\sqrt{2}}\left(|+|\Lambda|,+|\Sigma|,+|\Omega|\rangle-(-1)^{J-S}|-|\Lambda|,-|\Sigma|,-|\Omega|\rangle\right) \qquad (2.1.13)
\end{aligned}
$$

. These two states are degenerate when the molecule is not rotating. However, when the molecules is rotating, these two states are split due to adjacent Σ states and this phenomenon is called Λ doubling (or Ω doubling). There are three parameters o, p, and q to describe the Λ doubling and only p and q are non-zero for doublet diatomic molecules like CaF. The Λ doubling splitting for ${}^2\Pi_{1/2}$ states are

$$
\begin{aligned}
E_+ &= -(-1)^{J-1/2}\frac{1}{2}(p+2q)(J+\frac{1}{2}) \qquad (2.1.14)\\
E_- &= (-1)^{J-1/2}\frac{1}{2}(p+2q)(J+\frac{1}{2}) \qquad (2.1.15)
\end{aligned}
$$

.

The constants p and q, and the spin-rotation coupling constant γ which is described in the Hund's case (b) subsection all arise from the coupling between adjacent Π and Σ states. They depend on the vibrational quantum number v and can be partitioned into two parts - one from coupling of same vibrational states of the Π and Σ states ($\Delta v = 0$), and the other from coupling of different vibrational states of the Π and Σ states ($\Delta v \neq 0$) [67].

$$x_v = x_v^{\Delta v=0} + x_v^{\Delta v\neq 0} \tag{2.1.16}$$

, where $x = p$, q, or γ. Details about how to express each terms using $^2\Sigma \sim {}^2\Pi$ interaction constants a and b are well described in Ref. [67].

2.1.3.2 Hund's case (b)

Hund's case (b) is a case that the strong electrostatic force fixes the projection of the electronic orbital angular momentum onto the molecular axis and the nuclei rotational energy is much bigger than the spin-orbit coupling. Consequently, we should consider coupling of $\mathbf{L}$ onto the internuclear axis first, then coupling between the nuclei rotation angular momentum $\mathbf{R}$ and the Λ, and spin-orbit coupling at the last. This is a good representative for the CaF electronic ground state $X\,^2\Sigma$.

In this case, the projection of $\mathbf{L}$ onto the molecular axis (Λ) is well defined. This $\mathbf{\Lambda}$(vector along the internuclear axis with the amplitude Λ) combined with the nuclei rotation angular momentum $\mathbf{R}$ forms $\mathbf{N}$. Note that the projection of $\mathbf{N}$ onto the internuclear axis is also Λ since $\mathbf{R}$ is perpendicular to the internuclear axis and the lowest value that $\mathbf{N}$ can take is Λ. $\mathbf{J}$ is the sum of $\mathbf{N}$ and $\mathbf{S}$. Since $\mathbf{S}$ is freely rotating regardless of the molecular axis, the projection of $\mathbf{S}$ and $\mathbf{J}$ along the molecular axis are not well defined.

Rotation energy in Hund's case (b) The rotational Hamiltonian can be written as follows using good quantum numbers.

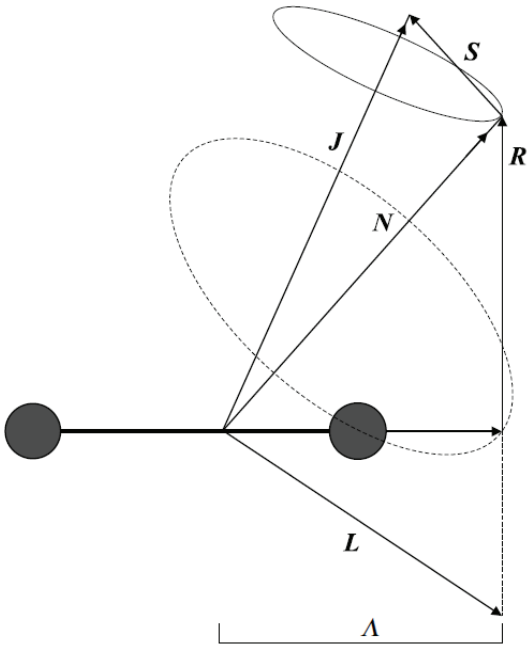

Figure 2.1.3: Angular momentum coupling in Hund's case (b) from Ref. [63]

$$
\begin{aligned}
H_{rot} &= B\,\mathbf{R}^2 \\
&= B\,(\mathbf{N}-\mathbf{\Lambda})^2 \\
&= B\,(\mathbf{N}^2+\mathbf{\Lambda}^2-2\mathbf{N}\cdot\mathbf{\Lambda}) \\
&= B\,(\mathbf{N}^2-\mathbf{\Lambda}^2) \\
&= B\,(N(N+1)-\Lambda(\Lambda-1)) \qquad (2.1.17)
\end{aligned}
$$

Here we use $\mathbf{N}\cdot\mathbf{\Lambda}=\mathbf{\Lambda}^2$ by the definition of $\mathbf{N}$. The rotational energy changes with the value of N.

Spin-rotation coupling and hyperfine interaction in Hund's case (b) The coupling between the electron spin and the rotation of the nuclei is

$$H_{spin-rotation}=\gamma_{vN}\mathbf{S}\cdot\mathbf{N} \qquad (2.1.18)$$

, where γ_{vN} can be expressed in a similar way to the Dunham coefficient.

$$\gamma_{vN}=\sum_{l\,m}\gamma^{l\,m}(v+\frac{1}{2})^l\,(N(N+1))^m \qquad (2.1.19)$$

When a molecule has its nuclear spin, the nuclear spin couples to the molecule's electron spin and the nuclei rotation via hyperfine interaction. Hyperfine interaction Hamiltonian is written as

$$H_{hf}=b_{vN}\mathbf{S}\cdot\mathbf{I}+c_{vN}S_zI_z+C_{vN}\mathbf{N}\cdot\mathbf{I} \qquad (2.1.20)$$

, where the first term describes the isotropic coupling between the electron and the nuclear spins, the second term the anisotropic coupling between the two, and the last one the coupling between the nuclei rotation and the nuclear spin. Each parameter here ($P=b$, c, or C) again

can be described as a sum

$$P_{vN} = \sum_{l\,m} P^{l\,m}(v+\frac{1}{2})^l\,(N(N+1))^m \tag{2.1.21}$$

.

2.1.3.3 Transform Hund's case (b) basis to Hund's case (a) basis

To transform Hund's case (b) basis to Hund's case (a) basis, we use corrected Eq. (6.149) in Ref. [63] .

$$\begin{aligned} |\Lambda, N, S, J, I, F, M_F\rangle \;=\; & \sum_{\Omega}\sum_{\Sigma}(-1)^{N-S+\Omega}\sqrt{2N+1} \\ & \times \begin{pmatrix} J & S & N \\ \Omega & -\Sigma & -\Lambda \end{pmatrix} |\Lambda, S, \Sigma, J, \Omega, I, F, M_F\rangle \end{aligned} \tag{2.1.22}$$

A detailed calculation to derive above is in Append. A.

2.2 Properties of CaF

2.2.1 Summary of constants for CaF

The important constants of CaF are summarized in this chapter.

2.2.1.1 General properties

- Electric dipole moment of the ground $X\,^2\Sigma^+$ state : 3.07 Debye [68]
- Magnetic dipole moment : 1 Bohr magneton
- lifetime of excited states : $A\,^2\Pi^+$ 19.2 ns [69], $B\,^2\Sigma^+$ 25.1 ns [70]

2.2.1.2 $X\,^2\Sigma$ state energy constants

Vibrational and rotational structure constants (Table 2.2)

Dunham Coefficient	(cm^{-1})	in Frequency
Y_{10}	588.64512	17.647137 THz
Y_{20}	-2.912508	-87.31479 GHz
Y_{30}	8.5215×10^{-3}	255.47 MHz
Y_{40}	-6.20×10^{-6}	186 kHz
Y_{01}	0.343709272	10.3041447 GHz
Y_{11}	-2.444414×10^{-3}	-73.28169 MHz
Y_{21}	4.9299×10^{-6}	147.79 kHz
Y_{31}	2.584×10^{-8}	774.7 Hz
Y_{02}	-4.68878×10^{-7}	-14.0566 kHz
Y_{12}	-1.633×10^{-10}	-4.896 Hz
Y_{22}	2.497×10^{-11}	0.7486 Hz

Table 2.2: $X\,^2\Sigma$ state rovibrational constants from Ref. [71, 72]

Spin-rotation coupling and hyperfine interaction constants (Table 2.3)

Constant	(MHz)
γ^{00}	39.65895
γ^{01}	1.0258×10^{-5}
γ^{02}	-5.462×10^{-10}
γ^{03}	-7.5×10^{-16}
γ^{10}	-3.21727×10^{-1}
γ^{11}	-2.102×10^{-6}
γ^{20}	-5.494×10^{-4}
γ^{21}	2.024×10^{-8}
b^{00}	109.1840
b^{01}	-5.1116×10^{-4}
b^{10}	-1.41529
c^{00}	40.1182
c^{10}	1.0567
C^{00}	2.907×10^{-2}

Table 2.3: Spin-rotation coupling and hyperfine interaction constants from Ref. [73]

2.2.1.3 $A\,^2\Pi$ and $B\,^2\Sigma$ states energy constants

Hyperfine interaction for these states are not known very much. The only reported values so far is $A\,^2\Pi(v = 0,\ J = 1/2,\ -)$ state value of 4.8 MHz, which is smaller than the linewidth

of the state (8.29 MHz) [69].

Vibrational and rotational structure constants (Table 2.4)

Constant	$A\,^2\Pi$		$B\,^2\Sigma$	
	(cm^{-1})	in frequency	(cm^{-1})	in frequency
T_e	16526.750	495.45950 THz	18840.190	564.81469 THz
A_e	71.429	2.1414 THz		
A_v	0.123	3.69 GHz		
ω_e	594.513	17.8231 THz	572.424	17.1608 THz
$\omega_e x_e$	3.031	90.87 GHz	3.101	92.97 GHz
B_e	0.348781	10.4562 GHz	0.342345	10.2632 GHz
α_e	2.526×10^{-3}	75.73 MHz	2.577×10^{-3}	77.26 MHz
D_e	4.8078×10^{-7}	14.413 kHz	4.815×10^{-7}	14.44 kHz

Table 2.4: $A\,^2\Pi$ and $B\,^2\Sigma$ state energy constants from Ref. [67] . Zero is defined as $T_e(X\,^2\Sigma^+) = 0$.

Λ doubling and spin-rotation coupling constants (Table 2.5, 2.6)

Constant	$A\,^2\Pi(v=0)$		$B\,^2\Sigma(v=0)$	
	(cm^{-1})	in frequency	(cm^{-1})	in frequency
p	-0.044517	-1.3346 GHz	NA	NA
q	-2.916×10^{-4}	-8.742 MHz	NA	NA
γ	NA	NA	-0.045770	-1.3722 GHz

Table 2.5: Measured Λ doubling, spin-rotation coupling constants for $A\,^2\Pi$ and $B\,^2\Sigma$states from Ref. [74]

$A\,^2\Pi$						
Constants	$v=0$		$v=1$		$v=2$	
	(cm^{-1})	in frequency	(cm^{-1})	in frequency	(cm^{-1})	in frequency
$p_v^{\Delta v=0}$	-4.38×10^{-2}	-1.31 GHz	-4.06×10^{-2}	-1.22 GHz	-3.75×10^{-2}	-1.12 GHz
$p_v^{\Delta v\neq 0}$	-0.166×10^{-2}	-49.8 MHz	-0.490×10^{-2}	-147 MHz	-0.808×10^{-2}	-242 MHz
p_v	-4.54×10^{-2}	-1.36 GHz	-4.55×10^{-2}	-1.36 GHz	-4.56×10^{-2}	-1.37 GHz
$q_v^{\Delta v=0}$	-2.17×10^{-4}	-6.51 MHz	-2.01×10^{-4}	-6.03 MHz	-1.84×10^{-4}	-5.52 MHz
$q_v^{\Delta v\neq 0}$	-0.104×10^{-4}	-0.312 MHz	-0.262×10^{-4}	-0.785 MHz	-0.417×10^{-4}	-1.25 MHz
q_v	-2.28×10^{-4}	-6.84 MHz	-2.27×10^{-4}	-6.81 MHz	-2.26×10^{-4}	-6.78 MHz
$B\,^2\Sigma$						
Constants	$v=0$		$v=1$		$v=2$	
	(cm^{-1})	in frequency	(cm^{-1})	in frequency	(cm^{-1})	in frequency
$\gamma_v^{\Delta v=0}$	-4.38×10^{-2}	-1.31 GHz	-4.06×10^{-2}	-1.22 GHz	-3.75×10^{-2}	-1.12 GHz
$\gamma_v^{\Delta v\neq 0}$	-0.164×10^{-2}	-49.2 MHz	-0.489×10^{-2}	-147 MHz	-0.879×10^{-2}	-264 MHz
γ_v	-4.54×10^{-2}	-1.36 GHz	-4.55×10^{-2}	-1.36 GHz	-4.63×10^{-2}	-1.39 GHz

Table 2.6: $A\,^2\Pi$ and $B\,^2\Sigma$state Λ doubling, spin-rotation coupling constants from Ref. [67]

2.2.1.4 $C\,^2\Pi$ and $D\,^2\Sigma$ states energy constants

Hyperfine interaction for these states have not been studied yet.

Vibrational and rotational structure constants (Table 2.7)

Constant	$C\,^2\Pi$		$D\,^2\Sigma^+$	
	(cm^{-1})	in frequency	(cm^{-1})	in frequency
T_e	30269.21	907.4481 THz	30124.33	903.1047 THz
A_e[1]	29.149	873.87 GHz		
A_v[??]	0.342	10.3 GHz		
ω_e	481.78	14.443 THz	657.33	19.706 THz
$\omega_e x_e$	1.95	58.5 GHz	2.85	85.4 GHz
B_e	0.32439	9.7250 GHz	0.3656	10.96 GHz
α_e	0.00205	61.5 MHz	0.002	60 MHz

Table 2.7: $C\,^2\Pi$ and $D\,^2\Sigma$ state energy constants from Ref. [75]. Zero is defined as $T_e(X\,^2\Sigma^+) = 0$.

Λ doubling and spin-rotation coupling constants (Table 2.8, 2.9)

Constant	$C\,^2\Pi(v=0)$		$D\,^2\Sigma(v=0)$	
	(cm^{-1})	in frequency	(cm^{-1})	in frequency
p	-0.00846	-254 MHz	NA	NA
γ	NA	NA	-0.00899	-270 MHz

Table 2.8: Measured Λ doubling, spin-rotation coupling constants for $C\,^2\Pi$ and $D\,^2\Sigma$states from Ref. [74]

Constants	$C\,^2\Pi$ $v=0$		Constants	$D\,^2\Sigma$ $v=0$	
	(cm^{-1})	in frequency		(cm^{-1})	in frequency
$p_v^{\Delta v=0}$	-8.8×10^{-3}	-260 MHz	$\gamma_v^{\Delta v=0}$	-8.8×10^{-3}	-260 MHz
$p_v^{\Delta v\neq0}$	1.1×10^{-3}	33 MHz	$\gamma_v^{\Delta v\neq0}$	0.3×10^{-3}	9 MHz
p_v	-7.7×10^{-3}	-230 MHz	γ_v	-8.5×10^{-3}	-250 MHz

Table 2.9: $C\,^2\Pi$ and $D\,^2\Sigma$state Λ doubling, spin-rotation coupling constants from Ref. [75]

2.2.1.5 Franck-Condon factors

$X\,^2\Sigma$ to $A\,^2\Pi_{1/2}$ transition (Table 2.10)

v''	$v'=0$	$v'=1$	$v'=2$
0	0.9643, 0.987^2	0.0359	1.934×10^{-4}
1	0.0344	0.8957	0.0696
2	0.0013	0.0647	0.8304
3	3.943×10^{-5}	0.0037	0.0920
4	1.206×10^{-6}	1.786×10^{-4}	0.0073

Table 2.10: Franck-Condon factors for $X\,^2\Sigma(v'')-A\,^2\Pi_{1/2}(v')$ transitions adapted from Ref. [76]

$X\,^2\Sigma$ to $B\,^2\Sigma$ transition (Table 2.11)

v''	$v'=0$	$v'=1$	$v'=2$
0	0.999	0.00137	
1	0.00134	0.995	0.00333
2		0.00321	0.991
3			0.00566

Table 2.11: Franck-Condon factors for $X\,^2\Sigma(v'')-B\,^2\Sigma(v')$ transitions adapted from Ref. [77]

2.2.2 Energy level structure of CaF molecules

The two electronic states that we use as the quasi-closed transition are the ground state $X\,^2\Sigma$ and the first electronic excited state $A\,^2\Pi_{1/2}$. In this section, eigenstates of these two electronic states are described.

2.2.2.1 $X\,^2\Sigma$ state Basis

Eigenstates of CaF $X\,^2\Sigma(v=0)$ states using Hund's case (b) basis

Full Hamiltonian for $X\,^2\Sigma(v=0)$ states Full Hamiltonian for CaF X states within the vibrational ground states is

$$H = B\mathbf{N}^2 + \gamma\mathbf{S}\cdot\mathbf{N} + b\mathbf{I}\cdot\mathbf{S} + cI_zS_z + C\mathbf{I}\cdot\mathbf{N} \tag{2.2.1}$$

, which describes rotational energy, spin-rotation interaction, and three hyperfine structure terms. We ignore the nuclear spin-rotation coupling (the last term) here since the constant C is only ~ 10^{-2} MHz and negligible in this calculation.

We use Hund's case (b) basis to calculate the matrix elements of this Hamiltonian. Relevant states are summarized in Table 2.12. We consider $F = 0, 1, 2$ states only in the lowest N states since those are the relevant states for laser cooling. CaF $X\,^2\Sigma$ states have $\Lambda = 0$, $S = 1/2$, and $I = 1/2$.

Quantum number	N	J	F
	3	5/2	2
	2	5/2	2
		3/2	2
			1
	1	3/2	2
			1
		1/2	1
			0
	0	1/2	1
			0

Table 2.12: Relevant $X\,^2\Sigma(v=0)$ states

The format we use to indicate CaF $X\,^2\Sigma$ states is $|\Lambda, N, J, F, M_F\rangle$ since both S and I are $1/2$ throughout the calculation. All magnetic sub-states are degenerate here.

Rotational Energy This part is already diagonal in this basis and has energy of $BN(N+1)$ where B is the rotational constant .

Spin-rotation interaction This part is also diagonal and has energy of

$$\frac{\gamma}{2}\left(J(J+1) - N(N+1) - S(S+1)\right) \tag{2.2.2}$$

, where γ is the spin-rotational coupling constant.

Hyperfine structure To calculate hyperfine structure matrix elements, we need to decompose **S** and **I** from **J** and **F**. For clarification, we use $|\Lambda, N, S, J, I, F, M_F\rangle$ to indicate states here.

1. $\mathbf{I}\cdot\mathbf{S}$ Using Ref. [63] Eq. (5.173), (5.174) and (5.179), we get

$$\langle \Lambda', N', S', J', I', F', M_F'|\,\mathbf{I}\cdot\mathbf{S}\,|\Lambda, N, S, J, I, F, M_F\rangle = \delta_{F'F}\delta_{M_F' M_F}(-1)^{J+F+I'}\begin{Bmatrix} I & J & F \\ J' & I' & 1 \end{Bmatrix}$$

$$
\begin{aligned}
& \times \langle N', S', J' \| \mathbf{S} \| N, S, J \rangle \langle I' \| \mathbf{I} \| I \rangle \\
= \; & \delta_{F'F} \delta_{M'_F M_F} (-1)^{J+F+I'} \left\{ \begin{array}{ccc} I & J & F \\ J' & I' & 1 \end{array} \right\} \\
& \times \delta_{N'N} (-1)^{J+N'+S'+1} \sqrt{(2J'+1)(2J+1)} \\
& \times \left\{ \begin{array}{ccc} S & J & N' \\ J' & S' & 1 \end{array} \right\} \langle S' \| \mathbf{S} \| S \rangle \langle I' \| \mathbf{I} \| I \rangle \\
= \; & \delta_{F'F} \delta_{M'_F M_F} \delta_{N'N} \delta_{S'S} \delta_{I'I} (-1)^{F+I'+N'+S'+2J+1} \\
& \times \sqrt{(2J'+1)(2J+1)} \sqrt{S(S+1)(2S+1)} \\
& \times \sqrt{I(I+1)(2I+1)} \\
& \times \left\{ \begin{array}{ccc} I & J & F \\ J' & I' & 1 \end{array} \right\} \left\{ \begin{array}{ccc} S & J & N' \\ J' & S' & 1 \end{array} \right\}. \qquad (2.2.3)
\end{aligned}
$$

2. $I_z = \mathbf{I} \cdot \mathbf{k}'$ **(k′: molecular axis unit vector)** Similarly,

$$
\begin{aligned}
\langle \Lambda', N', S', J', I', F', M'_F | \, \mathbf{I} \cdot \mathbf{k}' \, | \Lambda, N, S, J, I, F, M_F \rangle \; = \; & \delta_{F'F} \delta_{M'_F M_F} (-1)^{J+F+I'} \left\{ \begin{array}{ccc} I & J & F \\ J' & I' & 1 \end{array} \right\} \\
& \times \langle N', S', J' \| \mathbf{k}' \| N, S, J \rangle \langle I' \| \mathbf{I} \| I \rangle \\
= \; & \delta_{F'F} \delta_{M'_F M_F} (-1)^{J+F+I'} \left\{ \begin{array}{ccc} I & J & F \\ J' & I' & 1 \end{array} \right\} \\
& \times \delta_{S'S} (-1)^{J+N'+S'+1} \sqrt{(2J'+1)(2J+1)} \\
& \times \left\{ \begin{array}{ccc} N & J & S' \\ J' & N' & 1 \end{array} \right\} \langle N' \| \mathbf{k}' \| N \rangle \langle I' \| \mathbf{I} \| I \rangle \\
= \; & \delta_{F'F} \delta_{M'_F M_F} \delta_{S'S} \delta_{I'I} (-1)^{F+I'+N'+S'+2J+1+N-\Lambda} \\
& \times \sqrt{(2J'+1)(2J+1)} \sqrt{I(I+1)(2I+1)} \\
& \times \sqrt{(2N'+1)(2N+1)} \left\{ \begin{array}{ccc} I & J & F \\ J' & I' & 1 \end{array} \right\} \\
& \left\{ \begin{array}{ccc} N & J & S' \\ J' & N' & 1 \end{array} \right\} \left(\begin{array}{ccc} N' & 1 & N \\ -\Lambda & 0 & \Lambda \end{array} \right) \qquad (2.2.4)
\end{aligned}
$$

.

For the last part, we use Ref. [63] (5.186) to get

$$\langle N' \| \mathbf{k}' \| N \rangle = (-1)^{N-\Lambda} \sqrt{(2N'+1)(2N+1)} \begin{pmatrix} N' & 1 & N \\ -\Lambda & 0 & \Lambda \end{pmatrix}. \quad (2.2.5)$$

3. $S_z = \mathbf{S} \cdot \mathbf{k}'$ **(k′: molecular axis unit vector)** Here, since S_z does not operate on nuclear spin, we use Ref. [63] Eq. (5.176) and get

$$\begin{aligned} \langle \Lambda', N', S', J', I', F', M_F' | \mathbf{S} \cdot \mathbf{k}' | \Lambda, N, S, J, I, F, M_F \rangle &= \delta_{F'F} \delta_{M_F' M_F} \delta_{I'I} \langle N', S', J' | \mathbf{S} \cdot \mathbf{k}' | N, S, J \rangle \\ &= \delta_{F'F} \delta_{M_F' M_F} \delta_{I'I} \delta_{J'J} (-1)^{N+S'+J} \begin{Bmatrix} S & N & J \\ N' & S' & 1 \end{Bmatrix} \\ &\quad \times \langle S' \| \mathbf{S} \| S \rangle \langle N' \| \mathbf{k}' \| N \rangle \\ &= \delta_{F'F} \delta_{M_F' M_F} \delta_{I'I} \delta_{J'J} \delta_{S'S} (-1)^{2N+S'+J-\Lambda} \\ &\quad \times \sqrt{S(S+1)(2S+1)} \sqrt{(2N'+1)(2N+1)} \\ &\quad \times \begin{Bmatrix} S & N & J \\ N' & S' & 1 \end{Bmatrix} \begin{pmatrix} N' & 1 & N \\ -\Lambda & 0 & \Lambda \end{pmatrix}. \end{aligned} \quad (2.2.6)$$

Isotropic part of the hyperfine interaction mixes different J states within the same N states. Anisotropic part of it mixes N states that differ by 2. The results are confirmed using a different method described in Ref. [78].

Matrix Elements and eigenstates of the X state The matrix elements of the full Hamiltonian are summarized in Table 2.13. The states are sorted by the parity.

By diagonalizing this matrix, the eigenstates of the X states can be calculated and they are summarized in Append. B.

2.2.2.2 $A\,^2\Pi^+$state Basis

Eigenstates of CaF $A\,^2\Pi_{\frac{1}{2}}(v=0)$ **states using Hund's case (a) basis** The excited states that we care in this calculation are $A\,^2\Pi_{1/2}(v=0,\ J=1/2)$ states. Since the A state

$\left\vert 3,\frac{5}{2},2\right\rangle$	$\left\vert 1,\frac{3}{2},2\right\rangle$	$\left\vert 1,\frac{3}{2},1\right\rangle$	$\left\vert 1,\frac{1}{2},1\right\rangle$	$\left\vert 1,\frac{1}{2},0\right\rangle$	$\left\vert 2,\frac{5}{2},2\right\rangle$	$\left\vert 2,\frac{3}{2},2\right\rangle$	$\left\vert 2,\frac{3}{2},1\right\rangle$	$\left\vert 0,\frac{1}{2},1\right\rangle$	$\left\vert 0,\frac{1}{2},0\right\rangle$
$12B-2\gamma$ $+\frac{b}{4}-\frac{c}{20}$ $\frac{1}{5}\sqrt{\frac{3}{2}}c$	$\frac{1}{5}\sqrt{\frac{3}{2}}c$ $2B+\frac{\gamma}{2}$ $+\frac{b}{4}+\frac{c}{20}$								
		$2B+\frac{\gamma}{2}$ $-\frac{5}{12}b-\frac{c}{12}$ $-\frac{\sqrt{2}}{3}b+\frac{c}{3\sqrt{2}}$	$-\frac{\sqrt{2}}{3}b+\frac{c}{3\sqrt{2}}$ $2B-\gamma$ $-\frac{b}{12}+\frac{c}{12}$						
				$2B-\gamma$ $+\frac{b}{4}-\frac{c}{4}$					
					$6B+\gamma$ $-\frac{7}{20}b-\frac{c}{20}$ $-\frac{\sqrt{6}}{5}b+\frac{1}{5}\sqrt{\frac{3}{2}}c$	$-\frac{\sqrt{6}}{5}b+\frac{1}{5}\sqrt{\frac{3}{2}}c$ $6B-\frac{3}{2}\gamma$ $-\frac{3}{20}b+\frac{c}{20}$			
							$6B-\frac{3}{2}\gamma$ $+\frac{b}{4}-\frac{c}{12}$ $\frac{c}{3\sqrt{2}}$	$\frac{c}{3\sqrt{2}}$ $\frac{b}{4}+\frac{c}{12}$	$-\frac{3}{4}b-\frac{c}{4}$

Table 2.13: Matrix elements of full Hamiltonian for CaF $X\,^2\Sigma(v=0)$ state. The basis is described by 3 quantum numbers $|N,J,F\rangle$. The blank indicates zero.

is a $^2\Pi_{1/2}$ state, $|\Lambda| = 1$. Again, S and I are $\frac{1}{2}$ for all states. In Hund's case (a) basis, all relevant states are

$$\begin{aligned}
&\left|\Lambda = 1, \Sigma = -\tfrac{1}{2}, J = \tfrac{1}{2}, \Omega = \tfrac{1}{2}, F = 1, M_F = 1\right\rangle \\
&\left|\Lambda = 1, \Sigma = -\tfrac{1}{2}, J = \tfrac{1}{2}, \Omega = \tfrac{1}{2}, F = 1, M_F = 0\right\rangle \\
&\left|\Lambda = 1, \Sigma = -\tfrac{1}{2}, J = \tfrac{1}{2}, \Omega = \tfrac{1}{2}, F = 1, M_F = -1\right\rangle \\
&\left|\Lambda = 1, \Sigma = -\tfrac{1}{2}, J = \tfrac{1}{2}, \Omega = \tfrac{1}{2}, F = 0, M_F = 0\right\rangle \\
&\left|\Lambda = -1, \Sigma = \tfrac{1}{2}, J = \tfrac{1}{2}, \Omega = -\tfrac{1}{2}, F = 1, M_F = 1\right\rangle \\
&\left|\Lambda = -1, \Sigma = \tfrac{1}{2}, J = \tfrac{1}{2}, \Omega = -\tfrac{1}{2}, F = 1, M_F = 0\right\rangle \\
&\left|\Lambda = -1, \Sigma = \tfrac{1}{2}, J = \tfrac{1}{2}, \Omega = -\tfrac{1}{2}, F = 1, M_F = -1\right\rangle \\
&\left|\Lambda = -1, \Sigma = \tfrac{1}{2}, J = \tfrac{1}{2}, \Omega = -\tfrac{1}{2}, F = 0, M_F = 0\right\rangle
\end{aligned} \tag{2.2.7}$$

To form the basis of the excited states which are eigenstates of parity, we transform the above states as below.

$$\begin{aligned}
|+, F = 1, M_F = 1\rangle &= \frac{1}{\sqrt{2}}\left|\Lambda = 1, \Sigma = -\frac{1}{2}, J = \frac{1}{2}, \Omega = \frac{1}{2}, F = 1, M_F = 1\right\rangle \\
&\quad + \frac{1}{\sqrt{2}}\left|\Lambda = -1, \Sigma = \frac{1}{2}, J = \frac{1}{2}, \Omega = -\frac{1}{2}, F = 1, M_F = 1\right\rangle \\
|+, F = 1, M_F = 0\rangle &= \frac{1}{\sqrt{2}}\left|\Lambda = 1, \Sigma = -\frac{1}{2}, J = \frac{1}{2}, \Omega = \frac{1}{2}, F = 1, M_F = 0\right\rangle \\
&\quad + \frac{1}{\sqrt{2}}\left|\Lambda = -1, \Sigma = \frac{1}{2}, J = \frac{1}{2}, \Omega = -\frac{1}{2}, F = 1, M_F = 0\right\rangle \\
|+, F = 1, M_F = -1\rangle &= \frac{1}{\sqrt{2}}\left|\Lambda = 1, \Sigma = -\frac{1}{2}, J = \frac{1}{2}, \Omega = \frac{1}{2}, F = 1, M_F = -1\right\rangle \\
&\quad + \frac{1}{\sqrt{2}}\left|\Lambda = -1, \Sigma = \frac{1}{2}, J = \frac{1}{2}, \Omega = -\frac{1}{2}, F = 1, M_F = -1\right\rangle \\
|+, F = 0, M_F = 0\rangle &= \frac{1}{\sqrt{2}}\left|\Lambda = 1, \Sigma = -\frac{1}{2}, J = \frac{1}{2}, \Omega = \frac{1}{2}, F = 0, M_F = 0\right\rangle \\
&\quad + \frac{1}{\sqrt{2}}\left|\Lambda = -1, \Sigma = \frac{1}{2}, J = \frac{1}{2}, \Omega = -\frac{1}{2}, F = 0, M_F = 0\right\rangle \\
|-, F = 1, M_F = 1\rangle &= \frac{1}{\sqrt{2}}\left|\Lambda = 1, \Sigma = -\frac{1}{2}, J = \frac{1}{2}, \Omega = \frac{1}{2}, F = 1, M_F = 1\right\rangle
\end{aligned}$$

$$
\begin{aligned}
& & -\frac{1}{\sqrt{2}}\left|\Lambda=-1,\Sigma=\frac{1}{2},J=\frac{1}{2},\Omega=-\frac{1}{2},F=1,M_F=1\right\rangle \\
|-,F=1,M_F=0\rangle &= & \frac{1}{\sqrt{2}}\left|\Lambda=1,\Sigma=-\frac{1}{2},J=\frac{1}{2},\Omega=\frac{1}{2},F=1,M_F=0\right\rangle \\
& & -\frac{1}{\sqrt{2}}\left|\Lambda=-1,\Sigma=\frac{1}{2},J=\frac{1}{2},\Omega=-\frac{1}{2},F=1,M_F=0\right\rangle \\
|-,F=1,M_F=-1\rangle &= & \frac{1}{\sqrt{2}}\left|\Lambda=1,\Sigma=-\frac{1}{2},J=\frac{1}{2},\Omega=\frac{1}{2},F=1,M_F=-1\right\rangle \\
& & -\frac{1}{\sqrt{2}}\left|\Lambda=-1,\Sigma=\frac{1}{2},J=\frac{1}{2},\Omega=-\frac{1}{2},F=1,M_F=-1\right\rangle \\
|-,F=0,M_F=0\rangle &= & \frac{1}{\sqrt{2}}\left|\Lambda=1,\Sigma=-\frac{1}{2},J=\frac{1}{2},\Omega=\frac{1}{2},F=0,M_F=0\right\rangle \\
& & -\frac{1}{\sqrt{2}}\left|\Lambda=-1,\Sigma=\frac{1}{2},J=\frac{1}{2},\Omega=-\frac{1}{2},F=0,M_F=0\right\rangle
\end{aligned}
$$

$|+\rangle$ states are even parity and $|-\rangle$ states are odd parity.

2.2.2.3 Schematic energy levels

The energy eigenstates from above are depicted in Fig. 2.2.1. Only frequently used states in this thesis are shown here.

2.2.3 Branching ratio

Here, we calculate the branching ratios from the $A\,^2\Pi_{1/2}(v=0,\ J=1/2,\ p=\pm,\ F=0,1)$ states of CaF to the $X\,^2\Sigma(v=0,\ F=0,1,2)$ states of CaF.

The Overall process is

- describe eigenstates of the ground $X\,^2\Sigma$ states in Hund's case (b) basis (Subsection 2.2.2.1),
- transform Hund's case (b) basis to Hund's case (a) basis (Subsection 2.2.2.2),
- describe eigenstates of the excited $A\,^2\Pi_{1/2}$ states in Hund's case (a) basis (Subsection 2.1.3.3),
- and calculate ratios of matrix elements of electric dipole transition operator in Hund's case (a) basis (Subsection 2.2.3.1).

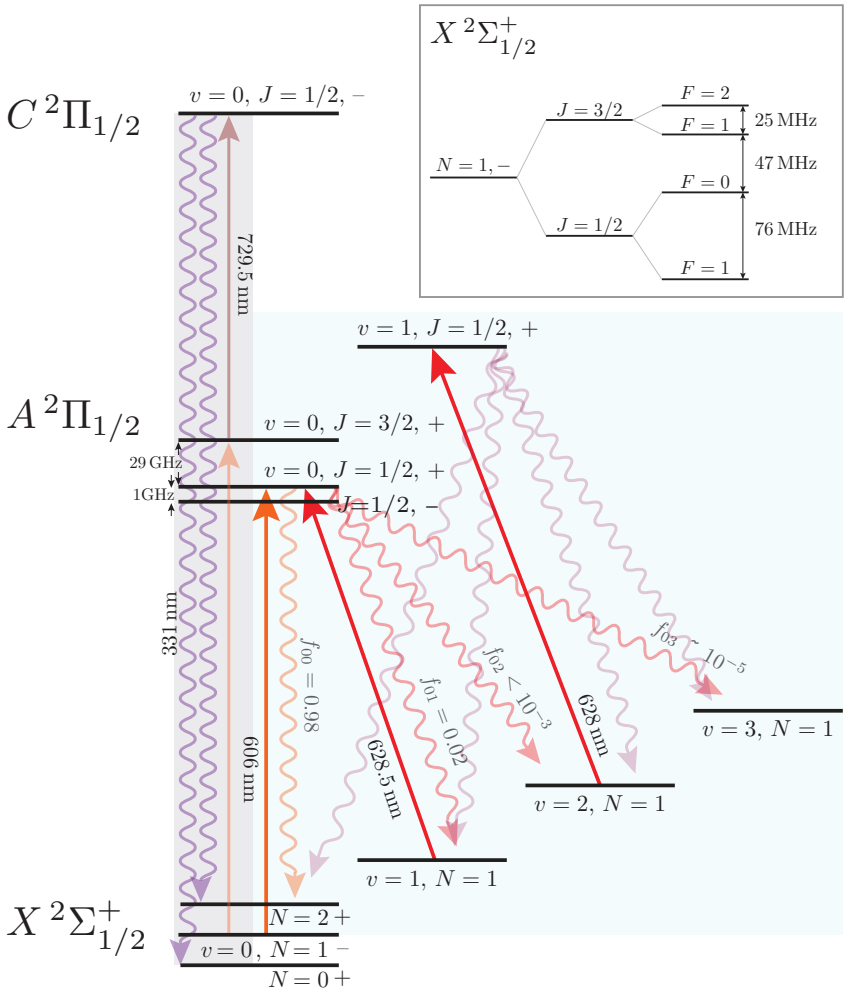

Figure 2.2.1: Relevant energy levels of CaF molecules. The inset shows the spin-rotation and hyperfine splittings in the ground state $X\,^2\Sigma(N = 1)$.

2.2.3.1 Electric Dipole Transition Operator in Hund's case (a) Basis

In this chapter, we calculate ratios of matrix elements of the electric dipole transition operator in Hund's case (a) basis $|\Lambda, \Sigma, J, \Omega, F, M_F\rangle$ following Appendix in Ref. [69]. Below is the equation to calculate the elements. Quantum numbers for the excited $A\,^2\Pi_{1/2}$ states has $'$ on them.

$$\begin{aligned}
\langle A'|\, T_p^{(1)}(\mathbf{d})\,|X\rangle &= (-1)^{F'-M_F'+F+2J'+I+1-\Omega'}\sqrt{(2F'+1)(2F+1)}\sqrt{(2J'+1)(2J+1)} \\
&\quad\times \begin{Bmatrix} J & F & I \\ F' & J' & 1 \end{Bmatrix} \begin{pmatrix} F' & 1 & F \\ -M_F' & p & M_F \end{pmatrix} \\
&\quad\times \sum_{q=-1}^{1} \begin{pmatrix} J' & 1 & J \\ -\Omega' & q & \Omega \end{pmatrix} \langle \Lambda', \Sigma' \|\, T_q^{(1)}(\mathbf{d})\, \|\Lambda, \Sigma\rangle \\
&= (-1)^{F'-M_F'+F+2J'+I+1-\Omega'}\sqrt{(2F'+1)(2F+1)}\sqrt{(2J'+1)(2J+1)} \\
&\quad\times \begin{Bmatrix} J & F & I \\ F' & J' & 1 \end{Bmatrix} \begin{pmatrix} F' & 1 & F \\ -M_F' & p & M_F \end{pmatrix} \\
&\quad\times \sum_{q=-1}^{1} \begin{pmatrix} J' & 1 & J \\ -\Omega' & q & \Omega \end{pmatrix} \delta_{\Sigma'\Sigma} \langle \Lambda' \|\, T_q^{(1)}(\mathbf{d})\, \|\Lambda\rangle
\end{aligned} \tag{2.2.8}$$

Since the electric dipole transition cannot change electron spin and thus its projection, $\Sigma' = \Sigma$ should be satisfied. The reduced matrix element $\langle \Lambda' \|\, T_q^{(1)}(\mathbf{d})\, \|\Lambda\rangle$ is common for all transitions does not affect to the branching ratios.

2.2.3.2 Results

The branching ratio results are summarized here. There are two cases - from the odd parity excited states to the even parity ground states, and from the even parity excited states to the odd parity ground states. All polarizations of the emitted photons are considered. If you want to know the results for one particular polarization, please see the Mathematical code

that is described in Append. C. These results agree to the ones in Ref. [69].

2.2.4 Saturation Intensity of the laser cooing main transition

Saturation intensity is defined as

$$I_s = \frac{\pi h\, c}{\lambda^3 \tau}\,\frac{1}{r} \tag{2.2.9}$$

where r is branching ratio back to the original state [69][3].

With $\lambda = 606$ nm and $\tau = 19.48$ ns, and vibrational branching ratio 0.987[69], the saturation intensity for $X\,(N=1)$ to $A\,(J=1/2,+)$ main transition is $I_s = 13.0$ mW/cm^2.

2.2.5 Zeeman shifts of the $X\,^2\Sigma$ ground state

The energy shift due to the external magnetic field ($\mathbf{B}$), called Zeeman shift, is determined by the Hamiltonian

$$H_{Zeeman} = -\boldsymbol{\mu}\cdot\mathbf{B} \tag{2.2.10}$$

, where $\boldsymbol{\mu} = -g_S\mu_B\mathbf{S} - g_L\mu_B\mathbf{L} + g_I\mu_N\mathbf{I}$. The field is fixed in the lab frame and we need to use lab fixed frame in this calculation. For a MOT, we are in the weak field regime where the F and M_F are still the good quantum numbers. Using the Hund's case (b) basis, the Zeeman Hamiltonian matrix elements for CaF $X\,^2\Sigma(N=1)$ states can be written as follows from Eq. (8.183) - (8.185) of Ref. [63][4].

$$\begin{aligned}\langle \Lambda, N, S, J, I, F, M_F |\, g_S\mu_B B_Z T^{(1)}_{p=0}(\mathbf{S})\,| \Lambda, N, S, J', I, F', M_F\rangle &= g_S\mu_B B_Z (-1)^{F-M_F}\begin{pmatrix} F & 1 & F' \\ -M_F & 0 & M_F\end{pmatrix} \\ &\quad\times(-1)^{F'+J+1+I}\sqrt{(2F'+1)(2F+1)}\end{aligned}$$

[3]There is a different definition $I_s = \frac{\pi h\, c}{3\lambda^3\tau}$ in Ref. [79]. There, they assume a particular magnetic substate and polarization so that the absorption cross section is maximum there.

[4]Note that there is a typo in Eq. (8.183) of Ref. [63].

	$\lvert -, F=1, M_F=1\rangle$	$\lvert -, F=1, M_F=0\rangle$	$\lvert -, F=1, M_F=-1\rangle$	$\lvert -, F=0, M_F=0\rangle$
$\lvert N=2, J=\frac{5}{2}, F=2, M_F=2\rangle$	0.0296894	0	0	0
$\lvert N=2, J=\frac{5}{2}, F=2, M_F=1\rangle$	0.0148447	0.0148447	0	0
$\lvert N=2, J=\frac{5}{2}, F=2, M_F=0\rangle$	0.00494824	0.019793	0.00494824	0
$\lvert N=2, J=\frac{5}{2}, F=2, M_F=-1\rangle$	0	0.0148447	0.0148447	0
$\lvert N=2, J=\frac{5}{2}, F=2, M_F=-2\rangle$	0	0	0.0296894	0
$\lvert N=2, J=\frac{3}{2}, F=1, M_F=1\rangle$	0.027754	0.027754	0	0.111159
$\lvert N=2, J=\frac{3}{2}, F=1, M_F=0\rangle$	0.027754	0	0.027754	0.111159
$\lvert N=2, J=\frac{3}{2}, F=1, M_F=-1\rangle$	0	0.027754	0.027754	0.111159
$\lvert N=2, J=\frac{3}{2}, F=2, M_F=2\rangle$	0.136977	0	0	0
$\lvert N=2, J=\frac{3}{2}, F=2, M_F=1\rangle$	0.0684886	0.0684886	0	0
$\lvert N=2, J=\frac{3}{2}, F=2, M_F=0\rangle$	0.0228295	0.0913182	0.0228295	0
$\lvert N=2, J=\frac{3}{2}, F=2, M_F=-1\rangle$	0	0.0684886	0.0684886	0
$\lvert N=2, J=\frac{3}{2}, F=2, M_F=-2\rangle$	0	0	0.136977	0
$\lvert N=0, J=\frac{1}{2}, F=1, M_F=1\rangle$	0.222246	0.222246	0	0.222175
$\lvert N=0, J=\frac{1}{2}, F=1, M_F=0\rangle$	0.222246	0	0.222246	0.222175
$\lvert N=0, J=\frac{1}{2}, F=1, M_F=-1\rangle$	0	0.222246	0.222246	0.222175
$\lvert N=0, J=\frac{1}{2}, F=0, M_F=0\rangle$	$\frac{2}{9}$	$\frac{2}{9}$	$\frac{2}{9}$	0

Table 2.14: Branching ratio from the odd parity states of $A\,^2\Pi_{1/2}$ to the even parity states of $X\,^2\Sigma$.

	$\|+, F=1, M_F=1\rangle$	$\|+, F=1, M_F=0\rangle$	$\|+, F=1, M_F=-1\rangle$	$\|+, F=0, M_F=0\rangle$
$\|N=3, J=\frac{5}{2}, F=2, M_F=2\rangle$	1.48975×10^{-9}	0	0	0
$\|N=3, J=\frac{5}{2}, F=2, M_F=1\rangle$	7.44873×10^{-10}	7.44873×10^{-10}	0	0
$\|N=3, J=\frac{5}{2}, F=2, M_F=0\rangle$	2.48291×10^{-10}	9.93164×10^{-10}	2.48291×10^{-10}	0
$\|N=3, J=\frac{5}{2}, F=2, M_F=-1\rangle$	0	7.44873×10^{-10}	7.44873×10^{-10}	0
$\|N=3, J=\frac{5}{2}, F=2, M_F=-2\rangle$	0	0	1.48975×10^{-9}	0
$\|N=1, J=\frac{3}{2}, F=2, M_F=2\rangle$	0.166667 ($\sim\frac{1}{6}$)	0	0	0
$\|N=1, J=\frac{3}{2}, F=2, M_F=1\rangle$	0.0833333 ($\sim\frac{1}{12}$)	0.0833333 ($\sim\frac{1}{12}$)	0	0
$\|N=1, J=\frac{3}{2}, F=2, M_F=0\rangle$	0.0277778 ($\sim\frac{1}{36}$)	0.111111 ($\sim\frac{1}{9}$)	0.0277778 ($\sim\frac{1}{36}$)	0
$\|N=1, J=\frac{3}{2}, F=2, M_F=-1\rangle$	0	0.0833333 ($\sim\frac{1}{12}$)	0.0833333 ($\sim\frac{1}{12}$)	0
$\|N=1, J=\frac{3}{2}, F=2, M_F=-2\rangle$	0	0	0.166667 ($\sim\frac{1}{6}$)	0
$\|N=1, J=\frac{3}{2}, F=1, M_F=1\rangle$	0.18327	0.18327	0	0.00175166
$\|N=1, J=\frac{3}{2}, F=1, M_F=0\rangle$	0.18327	0	0.18327	0.00175166
$\|N=1, J=\frac{3}{2}, F=1, M_F=-1\rangle$	0	0.18327	0.18327	0.00175166
$\|N=1, J=\frac{1}{2}, F=0, M_F=0\rangle$	$\frac{2}{9}$	$\frac{2}{9}$	$\frac{2}{9}$	0
$\|N=1, J=\frac{1}{2}, F=1, M_F=1\rangle$	0.0667298	0.0667298	0	0.331582
$\|N=1, J=\frac{1}{2}, F=1, M_F=0\rangle$	0.0667298	0	0.0667298	0.331582
$\|N=1, J=\frac{1}{2}, F=1, M_F=1\rangle$	0	0.0667298	0.0667298	0.331582

Table 2.15: Branching ratio from the even parity states of $A\,^2\Pi_{1/2}$ to the odd parity states of $X\,^2\Sigma$. These are the relevant states for laser cooling.

$$
\begin{aligned}
&\times(-1)^{J'+N+1+S}\sqrt{(2J'+1)(2J+1)} \\
&\times\sqrt{S(S+1)(2S+1)}\begin{Bmatrix} F & J & I \\ J' & F' & 1 \end{Bmatrix} \\
&\times\begin{Bmatrix} J & S & N \\ S & J' & 1 \end{Bmatrix} \qquad (2.2.11)
\end{aligned}
$$

$$
\begin{aligned}
\langle \Lambda, N, S, J, I, F, M_F | \, g_L \mu_B B_Z T^{(1)}_{p=0}(\mathbf{L}) \, | \Lambda, N', S, J', I, F', M_F \rangle \;=\;& g_L \mu_B B_Z (-1)^{F-M_F} \begin{pmatrix} F & 1 & F' \\ -M_F & 0 & M_F \end{pmatrix} \\
&\times(-1)^{F'+J+1+I}\sqrt{(2F'+1)(2F+1)} \\
&\times(-1)^{J'+N+1+S}\sqrt{(2J'+1)(2J+1)} \\
&\times(-1)^{N-\Lambda}\sqrt{(2N+1)(2N'+1)} \\
&\times\begin{Bmatrix} F & J & I \\ J' & F' & 1 \end{Bmatrix}\begin{Bmatrix} J & N & S \\ N' & J' & 1 \end{Bmatrix} \\
&\times\begin{pmatrix} N & 1 & N' \\ -\Lambda & 0 & \Lambda \end{pmatrix} \Lambda \qquad (2.2.12)
\end{aligned}
$$

$$
\begin{aligned}
\langle \Lambda, N, S, J, I, F, M_F | -g_I \mu_N B_Z T^{(1)}_{p=0}(\mathbf{I}) \, | \Lambda, N, S, J, I, F', M_F \rangle \;=\;& -g_I \mu_N B_Z (-1)^{F-M_F} \begin{pmatrix} F & 1 & F' \\ -M_F & 0 & M_F \end{pmatrix} \\
&\times(-1)^{F'+J+1+I}\sqrt{(2F'+1)(2F+1)} \\
&\times\sqrt{(I(I+1)(2I+1)} \\
&\times\begin{Bmatrix} F & I & J \\ I & F' & 1 \end{Bmatrix} \qquad (2.2.13)
\end{aligned}
$$

By diagonalizing this matrix at each B field strength, we can calculate the energy shift of each hyperfine state due to the magnetic field (Fig. 2.2.2). Up to 5 Gauss, the total angular momentum F is a good quantum number and we can approximate the energy shift using Lande-g factor of F states (g_F).

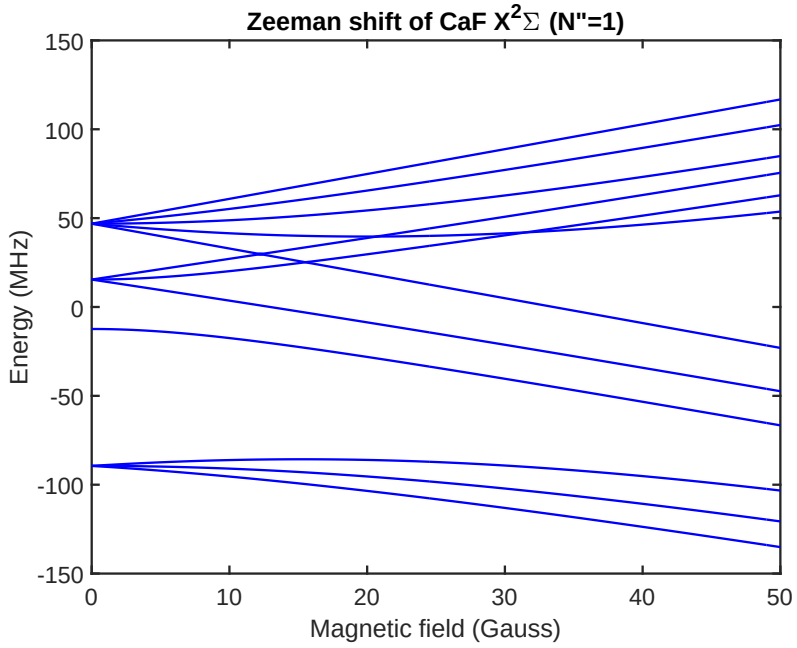

Figure 2.2.2: Zeeman shift of $X\,^2\Sigma(N = 1)$ states. The splitting at zero field is due to the spin-rotation coupling and the hyperfine interaction. From the highest energy state, the states are $(J,\, F) = (\frac{3}{2},\, 2)$, $(\frac{3}{2},\, 1)$, $(\frac{1}{2},\, 0)$, and $(\frac{1}{2},\, 1)$.

2.2.6 Laser configuration for CaF : forming a quasi-closed optical cycle

To slow molecules and trap them using photon scattering, one needs a closed cycle so that the molecule can scatter many photons and still in the same state. However, internal degrees of freedom in diatomic molecular structure hinders the molecules from scattering photons continuously. One needs to carefully select a molecule, block the leakage to the higher vibrational states, and choose the right rotational states to work with to cycle reasonable number of photons. More details for each component are summarized in this section.

2.2.6.1 Vibrational repump laser

For diatomic molecules, there is one vibrational mode which is the stretching mode of the two nuclei. Each electronic state has a series of vibrational excited states. When you excite a molecule to a certain vibrational state in the electronic excited state, it can decay back

to any vibrational state in the electronic ground state. The probability of the decay is determined only by the wavefunction overlap squared $|\langle\psi_{e,v'}|\psi_{g,v''}\rangle|^2$, which is the Franck-Condon factor. After scattering a few photons, some molecules decay to higher vibrational states even though the all the molecules start from a single vibrational state in the ground state and those vibrationally excited molecules are out of the cycling transition. To pump the molecules back to the cycling transition, a repump laser is necessary. In principle, the molecule can scatter infinite number of photons if infinite number of repump lasers are applied. In reality, one wants to select a molecule with diagonal Franck-Condon factors so that one needs the minimum number of repump lasers.

CaF has fairly diagonal Franck-Condon factors (Table 2.10) that it can scatter ~ 10^5 photons with 2 repump lasers before falling into the third vibrational state. The main transition ($X\,^2\Sigma(v=0)$ to $A\,^2\Pi_{1/2}(v=0)$) is at 606 nm, the first repump frequency from $X\,^2\Sigma(v=1)$ to $A\,^2\Pi_{1/2}(v=0)$ is 628.5 nm, and the second repump ($X\,^2\Sigma(v=2)$ to $A\,^2\Pi_{1/2}(v=1)$) is at 628.1 nm.

2.2.6.2 Selection rules for rotational states

The wavefunctions of the rotation of the nuclei can be described in the same way as the electron's angular momentum. Consequently, the transitions between the rotational states obey the same selection rules for the transitions between the electronic states. The leading order of the interaction between the photon (electromagnetic field) and the molecule is the electric dipole (E1) transition where we assume the molecule's size is a lot smaller than the wavelength of the light so that we can think the molecule as a point particle. The selection rules for the E1 transition is

1. only one electron changes its n, L state
2. parity must change
3. $\Delta J = 0, \pm 1$ ($J = 0 \leftrightarrow 0$ is not allowed)

4. $\Delta M_J = 0, \pm 1$.

For evaporation cooling or sympathetic cooling in the future, it is good to have molecules in the absolute ground state to reduce possible inelastic collisional channels. However, when the $X\,^2\Sigma(v = 0,\, N = 0,\, J = \frac{1}{2},\, +)$ absolute ground state molecule is pumped to the $A\,^2\Pi_{1/2}(v = 0,\, J = 1/2,\, -)$ excited state, the molecule will decay to the rotationally excited $X\,^2\Sigma(v = 0,\, N = 2,\, J = \frac{3}{2},\, +)$ state with about $1/3$ probability. This prevents to form a closed transition unless this state is repumped with another laser. One can use instead the next rotational state $X\,^2\Sigma(v = 0,\, N = 1,\, J = \frac{1}{2}, \frac{3}{2},\, -)$ [49]. When a molecule in this state is pumped to the $A\,^2\Pi_{1/2}(v = 0,\, J = 1/2,\, +)$ excited state, it can only decay back to the state where it started and this forms a closed transition. With this choice, only one laser is required per vibrational level.

So far, the discussion has been restricted to the E1 transition. For the cases when the molecules scatter a lot of photons, one needs to consider the next order terms, the magnetic dipole (M1) transition and the electric quadrupole (E2) transition strength from the excited state $A\,^2\Pi_{1/2}$. The M1 transition is from the magnetic dipole matrix element $\boldsymbol{\mu} = \mathbf{L} + 2\mathbf{S}$ and cannot change the electronic configuration. Therefore, all M1 transitions from the $A\,^2\Pi_{1/2}$ state are happening within the A state, and the wavelength of these M1 transitions are much longer than the E1 transitions (THz vs. 100s of THz). Also, μ is $\sim \alpha^2 \sim 5 \times 10^{-5}$ times smaller than the electric dipole moment $\mathbf{d}$, leading to the fact that the M1 transitions from the A states have $\sim \omega_{M1}^3 \alpha^2 / \omega_{E1}^3 \sim 10^{-9}$ weaker strength than the E1 transition and we can ignore it.

The E2 transition selection rules allows transitions with $\Delta J = 0, \pm 1, \pm 2$, $\Delta M_J = 0, \pm 1, \pm 2$ when the initial and final states have the same parity ($J = 0 \leftrightarrow 0$, $0 \leftrightarrow 1$, $1/2 \leftrightarrow 1/2$ are forbidden). Therefore, The excited state $A\,^2\Pi_{1/2}(v = 0,\, J = 1/2,\, +)$ can decay to $X\,^2\Sigma(v = 0,\, N = 2,\, J = 3/2, +)$ states via the E2 transition. The relative strength of the E2 transition to the E1 transition is

$$\begin{aligned} \frac{A_{E2}}{A_{E1}} &\sim \frac{\omega^2}{c^2}\frac{\langle f|\, r^2|i\rangle}{\langle f|r|i\rangle} \\ &\sim \left(\frac{a}{\lambda}\right)^2 \\ &\sim 4\times 10^{-8} \end{aligned} \tag{2.2.14}$$

. Here we assumed the molecules' size $a \sim 0.1$ nm and the transition wavelength $\lambda = 606$ nm. This ratio is smaller than the possibility of the decay to the 3rd vibrational excited state ($\sim 10^{-5}$).

From the above discussion, we can conclude that the selection rules for the E1 transition would allow us to select rotationally closed cycling transition within our photon budget from the vibrational states.

2.2.6.3 Spin-rotation and hyperfine splitting

The ground state $X\,^2\Sigma(N=1)$ splits into four states due to the spin-rotation and hyperfine interactions from the electron spin $S = 1/2$ and nuclei spin $I = 1/2$. One needs to address all these states in order to form a closed cycling transition. Fortunately, these splittings are on the order of 10s of MHz (Fig. 2.2.1) and multiple acousto-optic modulators (AOMs) or an electro-optic modulator (EOM) with right frequencies can be implemented to split one laser to address all the states.

2.2.6.4 Dark magnetic substates

Since our ground state has $J = 1/2$, $3/2$ and the excited state has $J = 1/2$, there are more number of states in the ground state than in the excited state. This configuration forms dark magnetic substates when the molecule scatters multiple photons with a fixed polarization. Fig. 2.2.3 depicts the case for σ^+ polarization light and the same thing happens for any fixed polarization. Once molecules are in the dark states, they can no longer absorb any photons

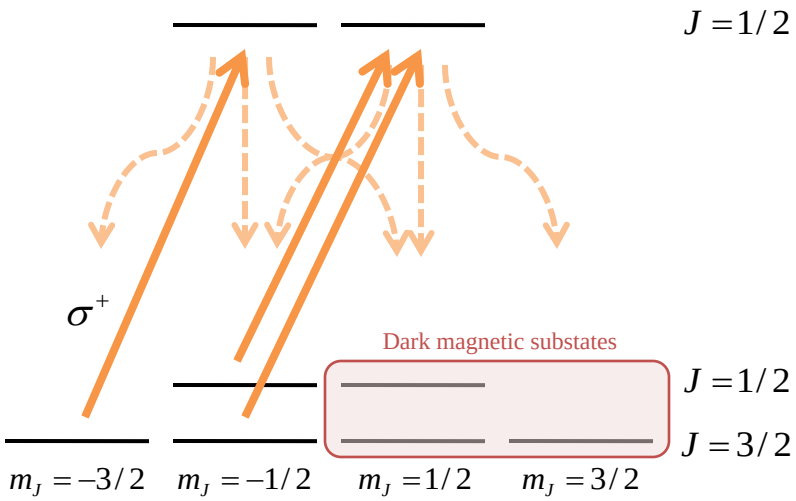

Figure 2.2.3: Dark magnetic substates for σ^+ light.

and the photon cycling ceases. To overcome this issue without coupling to other states which would increase the number of involved states involved, two methods can be implemented [80]. One is by applying a transverse magnetic field that are angled ($\theta \neq 0, 90$) with respect to the polarization. This would lift the degeneracy of the substates slightly and the dark states would precess to be bright states again [52]. The precess should be fast enough so that the time it takes for the dark state to be bright again is comparable to the excited state lifetime. A magnetic field of a few Gauss is enough to achieve this. This scheme is used for the laser slowing in this experiment as well.

Another way to overcome the dark state problem is to make the dark state bright by switching the polarization of light [53]. In Fig. 2.2.3, the dark states of σ^+ light are bright states of σ^- light. By switching the polarization of the light at the time scale of the excited state lifetime, all magnetic substates can scatter photons continuously. This method is used to make a MOT for ^{6}Li with D1 transition, which has dark magnetic substates, and will be used for CaF MOT as well.

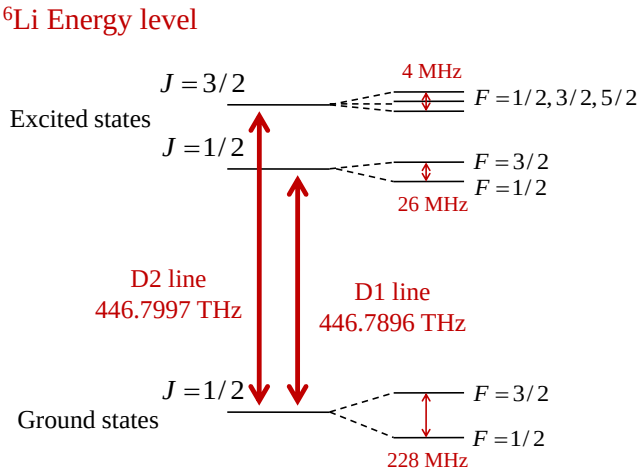

Figure 2.3.1: Energy level of ^{6}Li atoms.

2.3 Level structure of ^{6}Li atoms

As a first step towards the co-trapping of atoms and molecules, we trapped ^{6}Li atoms in an AC MOT. We chose ^{6}Li since it has smaller hyperfine splittings (228 MHz) in the electronic ground state than more abundant ^{7}Li (803 MHz) which makes it easy to address both hyperfine states using an AOM.

^{6}Li has two strong cycling transitions. The transition from the $J = 1/2$ ground state to the $J = 3/2$ excited state is named as D2 line (linewidth $\gamma = 2\pi \times 5.9$ MHz, saturation intensity = 2.54 mW) and is typically used to make a MOT since it forms a type I MOT without any dark substates. The transition between the $J = 1/2$ ground state and the $J = 1/2$ excited state is called D1 line and has a linewidth (γ)of $2\pi \times 5.9$ MHz and the saturation intensity of 7.59 mW [81]. This is the transition we used to make a AC MOT for ^{6}Li. D2 line is used for the white-light slowing.

2.3.1 Laser setup for ^{6}Li atoms

The wavelength of ^{6}Li transition is 671 nm. These days, people combine a diode laser and a tapered amplifier to generate 671 nm light with a lot of power. Here, we used two dye lasers with Rhodamine 640 instead due to the availability in the lab. One dye laser was used as a white-light slowing laser and the other dye laser was used as MOT beams. Each laser went through an AOM to imprint a sideband at 228 MHz for the hyperfine splitting.

After the AOM for hyperfine splitting, the slowing laser went through the white-light EOM to be broadened according to the RF driving power to the EOM. The slowing laser power going into the chamber was 27 mW for the $F = 1/2$ ground state and 11 mW for the $F = 3/2$ ground state.

The output of the MOT dye laser was divided into three beams using beam splitters to form three orthogonal MOT beams, x, y, and z beams. The x and y beams are 45 degrees to the molecular beam direction and the z beam is perpendicular to the molecular beam. The MOT laser powers were 14 mW, 17 mW, and 6 mW for x, y, and z beams with the powers equally distributed to both of the hyperfine states. These powers correspond to saturation parameters of about 2 for the x, y beams and 1 for the z beam.

Chapter 3

Experimental Setup

Most of the experimental setup for all the experiments in this thesis is described in this chapter. There are a few generations for the vacuum chambers and the two-stage cell and the changes made on each step are summarized as well.

3.1 two-stage buffer-gas cell

The two-stage cell design is described in detail in Ref. [82]. The main body is made out of highly pure copper with good thermal conductivity (Cu101) to maintain the low temperature during the generation of molecules. The whole cell is assembled as a set of stacked pieces using four 8-32 brass threaded rods with Belleville washers and stainless steal nuts through four holes on the corners of each part. The cell parts and molecular beam generation sequence are described here, from the upstream of the buffer-gas beam.

- Buffer-gas line : The buffer-gas line is made out of 1/8" outer diameter copper tube, which is connected to the room temperature He gas cylinder via several VCR joints and different kinds of tubes, is brazed to the copper plate. The buffer-gas line is heat-sunk to every stage of temperature (70 K, 4 K, and 1.5 K) before connected to the cell. The heat-sink parts are made out of Cu101 and the parts between components with

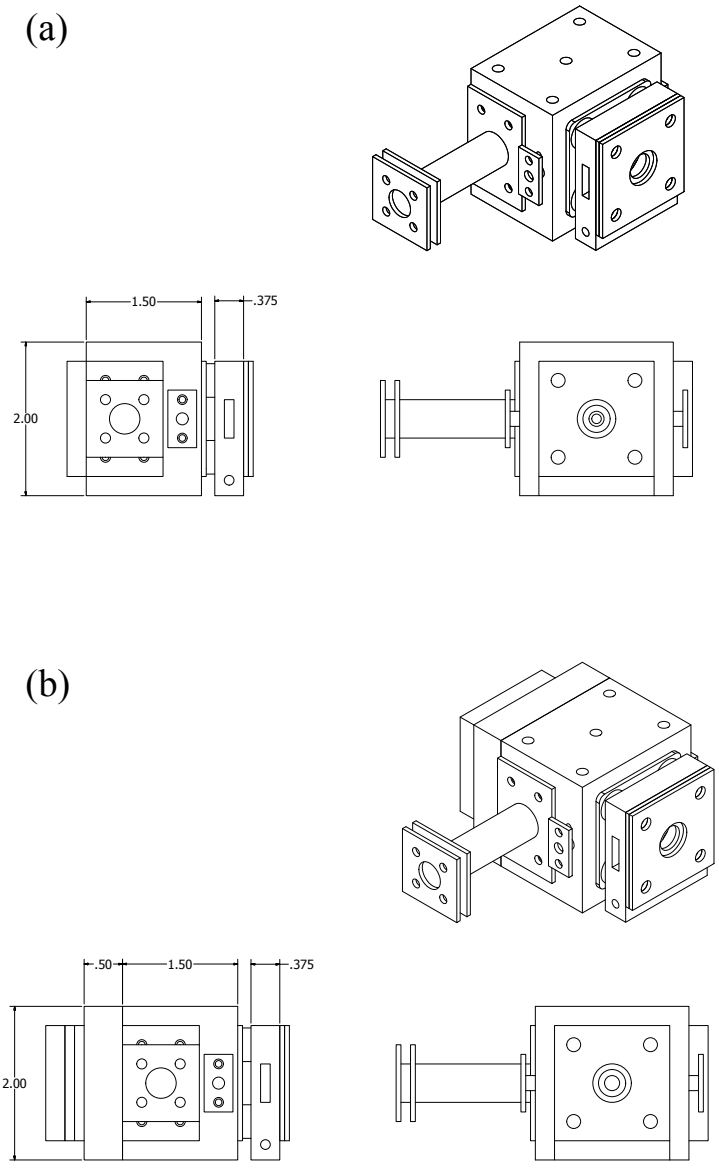

Figure 3.1.1: Two-stage cell. The dimensions are in inches. (a) the "old" cell which has been modified from the design in Ref. [82]. All ^{6}Li data are taken with his version. (b) the modified 'new' version which is used for taking all CaF data. The modification between the two are described in the text. The buffer-gas beam flows from left to right.

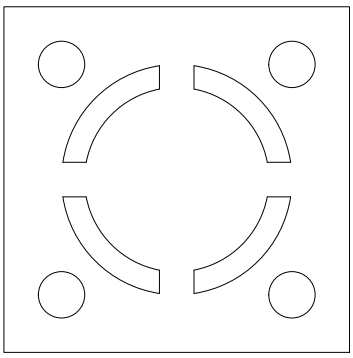

Figure 3.1.2: Diffuser. It is made out of 1.5" by 1.5" Cu101 with 1/8" thickness.

different temperatures are made out of SS316.

- Diffuser and 0.5" spacer (only for the new cell) : The new cell has a 1/8" thick diffuser (Fig. 3.1.2), placed about 1/8 inches from the buffer-gas line to prevent He gas from moving ballistically inside the cell. At the same time we also lengthened the distance between the buffer-gas line and the target by inserting a 0.5" thick spacer between the main body of the cell and the diffuser. These two features ensure that the buffer-gas thermalizes and uniformly fills the cell before colliding with the molecules.

- Main body (1st stage cell) : Most of the buffer-gas cooling takes place in this part. It is made out of Cu101 and the outer dimension is 2" by 2" by 1.5". The inner geometry is 1" diameter cylindrical hole with the length of 1.5" through the center of the body block. It has multiple holes on the side for in-cell absorption windows, a YAG window, and a target holder. The 1st stage aperture has 5 mm diameter. The He density in the 1st stage cell is on the order of $n \sim 10^{-15}$ cm^3.

- Target holder : Ablation targets sit about 0.5 inches (old cell) or 1.25 inches (new cell) from the buffer-gas line, glued to a copper target holder inside the main cell by Stycast 2850. Molecules and atoms generated by ablation thermalize with the cold ^{4}He buffer-gas at 1.5 K and come out through the 1st aperture.

- Snorkel : It is known in the group that the YAG window becomes contaminated by dust after a few days of run, which causes molecular beam degradation (faster forward velocity, less flux, etc.). To prevent this, a snorkel with the length of 1.5" is added to move the YAG window far from the target, which is the source of the dust.

- 2nd stage cell : The 2nd stage cell is designed to achieve an order of magnitude lower He density ($n \sim 10^{-14}$ cm^3) inside to give molecules a few more collisions with the buffer-gas. The molecules and the buffer-gas pass the gap between the main cell and the 2nd stage cell, which is set by three brass washers (∼3 mm), and enter the 2nd stage cell. The 2nd stage cell is 1" diameter cylinder with 0.375" long and has mesh-covered elongate holes on the side. The molecules exit the second aperture with 9 mm diameter which is covered by a mesh (47 % transparency) and form a molecular beam.

The beam properties are very sensitive to the cell geometry and some parameters were varied in the Ref.[83]. Still, many of the parameters' importances are unknown and we tried two different configurations (old and new) of the cell geometry and found differences in the forward velocity, which is described in Sec. 4.1.

3.2 Vacuum chamber

For the molecular MOT, we wanted to improve our setup in three ways from the previous setup described in Ch. 4.2.1. First, a colder base temperature was needed in order to get slower forward velocity and more population in the low rotational states. Second, we wanted to have a longer run-time for the experiment. The beam flux when generating molecules is about an order of magnitude lower than when generating atoms so that more averages are required. The new setup is designed for a run-time of 6 - 8 hours, compared to the previous generation run-time of 2 hours. The last improvement is lower background pressure which we would need to get a longer lifetime of the MOT. The pressure of 10^{-7} Torr we had in the previous setup would give ∼200 ms of the background gas limited lifetime assuming

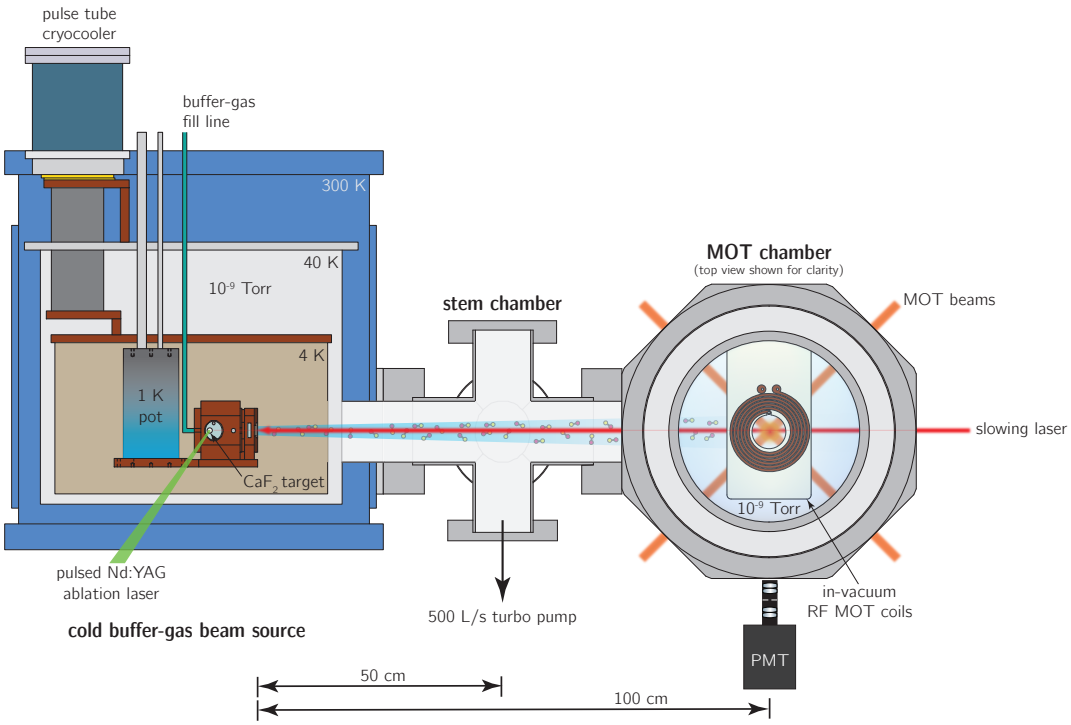

Figure 3.2.1: Overview of the experimental setup with stem region. ^{6}Li data were taken in this configuration. The figure is not to scale.

the dominant background gas is helium at room temperature. These led us to make a new chamber which could achieve all three goals above.

Fig. 3.2.1 depicts the overall schematic of the 2nd generation vacuum chamber setup. To reach the colder base temperature for the cell, we have a 1 K pot, which is same in principle to the helium bath in the previous setup. Here, however, the radiation shields are cooled by a commercial pulse tube cryocooler (Cryomech PT415) down to ∼4 K and ∼75 K. The 1 K pot and the cell are placed inside the 4 K shields and protected from the blackbody radiation so that the cell could reach down to ∼1.5 K when the pot is pumped by a vacuum pump. The MOT region is made out of S.S. CF-flanged components to get better base pressure with one (with stem region) or two (without stem region) large turbo pumps (TV-551 from Agilent Technologies). Fig. 3.2.2 is the Autodesk Inventor view of the actual chamber with stem region. Gate valves are places between different regions so that each region can be isolated when we make changes to one of the regions.

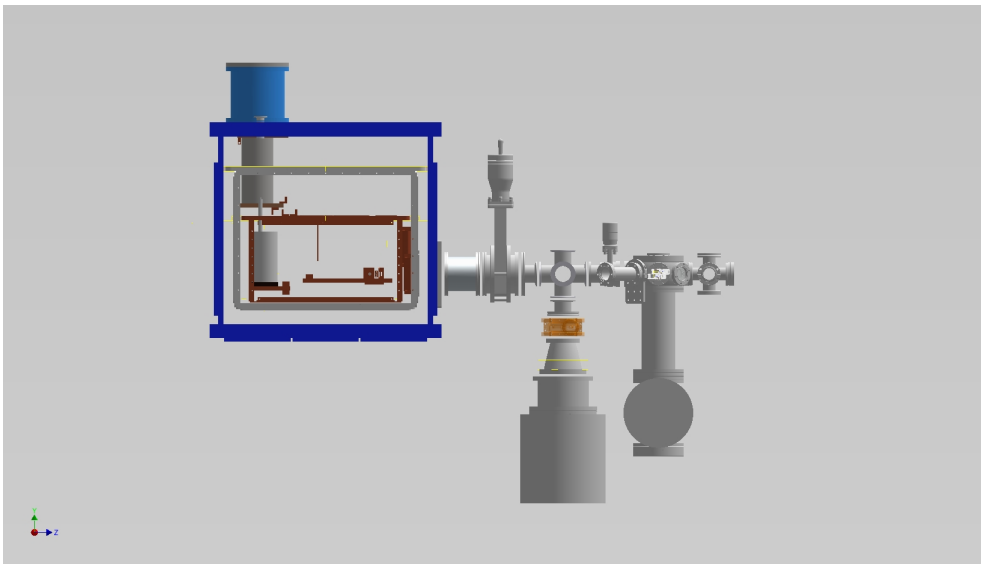

Figure 3.2.2: Real chamber setup from Autodesk Inventor program.

3.2.1 Blue beam box - cryogenic region

The buffer-gas beam intrinsically requires cryogenic temperatures to operate. The required temperature depends on the species of the buffer-gas (4 K or below for He, about 15 K for Ne) and to get the best out of the slow two-stage cell beam, ∼1.5 K is required. To achieve this low temperature, one needs to take care of the black-body radiation from the room temperature and reduce it as much as possible. We have two radiation shields - one at about 75 K and the other at about 4 K - to protect the two-stage cell located in the inner-most part of the blue beam box. The shields are cooled by a two-stage pulsed tube cryocooler PT415 from Cryomech. The first stage of the pulse tube has 40 W cooling power at 45 K and the second stage has 1.5 W cooling power at 4.2 K.

Fig. 3.2.3 shows each layer of the beam box from the outer most layer to the inner most. The chamber is a standard Doyle group design square chamber with lots of top ports to be used flexibly. All sealing is done with o-ring seals and we achieve $\sim 10^{-9}$ Torr inside the chamber thanks to the cryopumping.

The next layer is the 75 K shields (aluminum 6061), which are connected to the first stage of the pulse tube by about forty 10 cm long Cu101 flexible thermal heat links. The

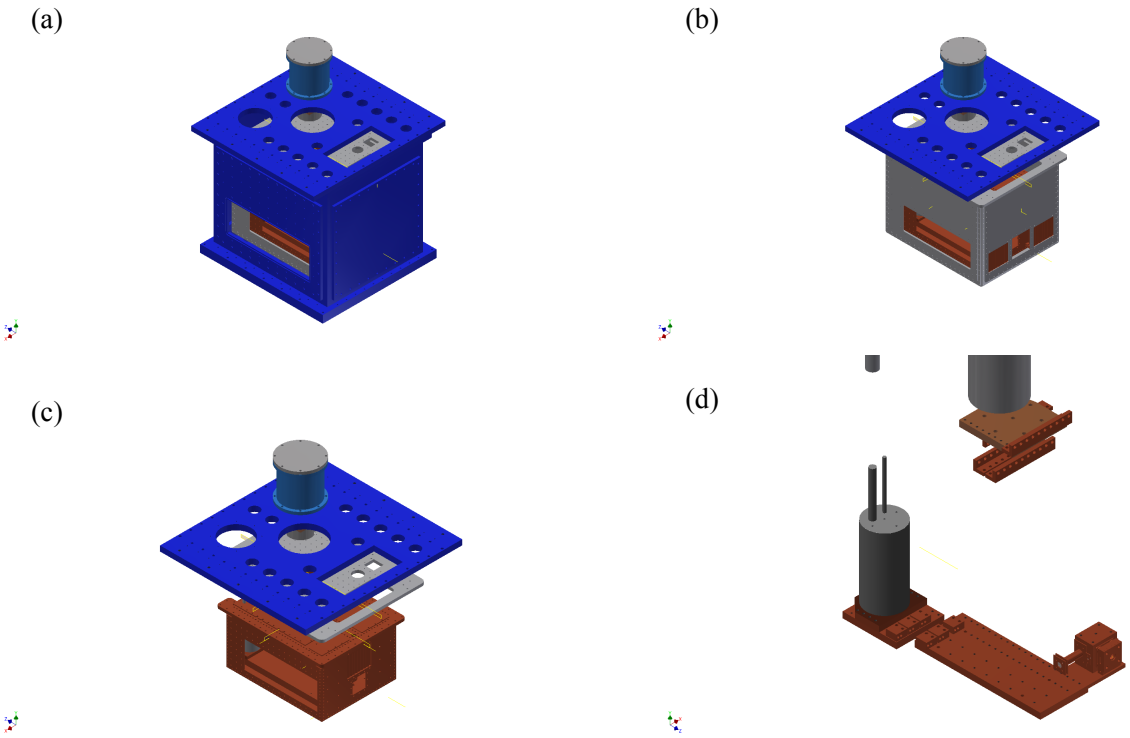

Figure 3.2.3: Beam Box view for each layer. (a) Blue beam box (o-ring sealed vacuum chamber). (b) 75 K shields. (c) 4 K shields. (d) 1 K pot, 1 K plate, and the two-stage cell.

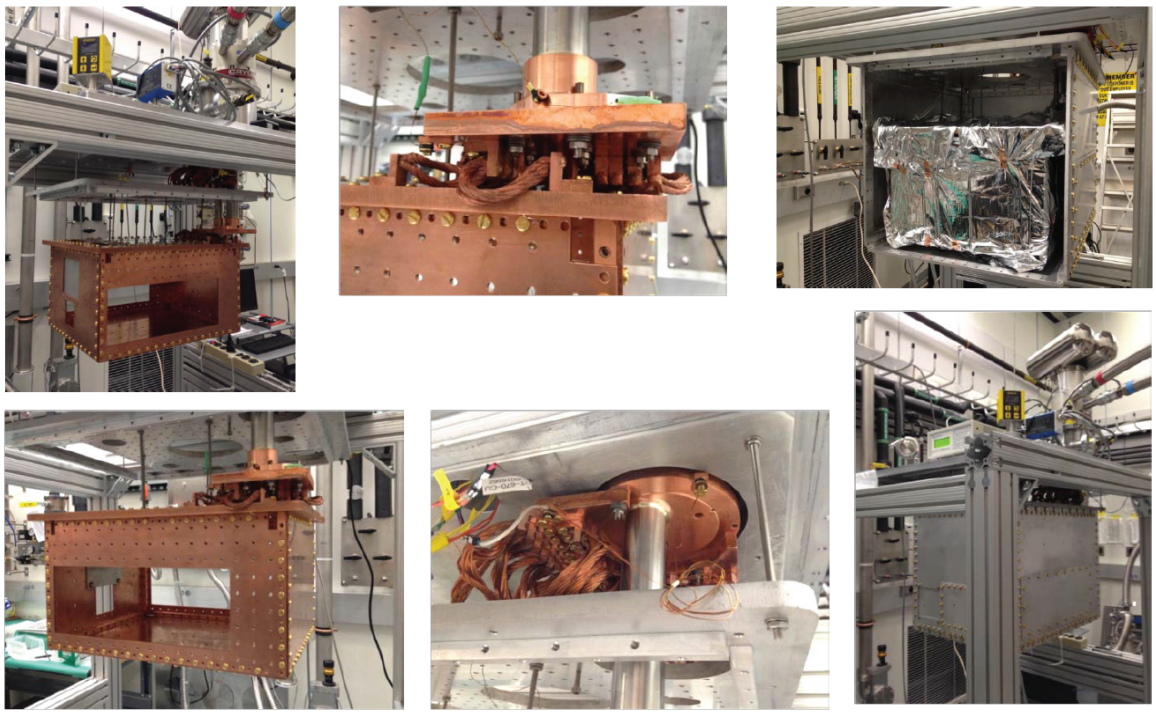

Figure 3.2.4: Photos of the radiation shields

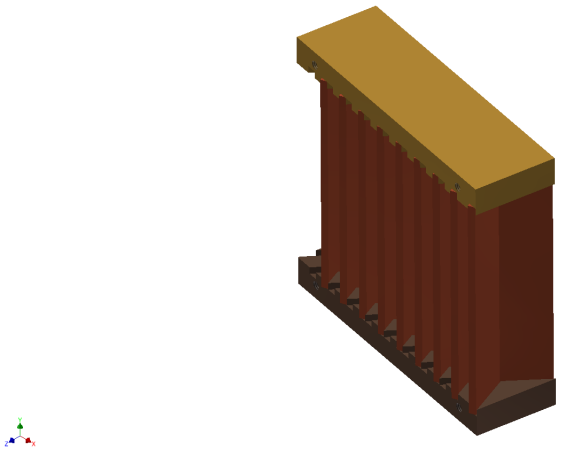

Figure 3.2.5: Chevron baffle assembly for gas conductance between shields

temperature difference across the flexible heat links is estimated to be about 6 K with 45 W heat load. The warmest part of the 75 K shields is at around 75 - 80 K. We use brass screws for assembling and the thermal expansion is matched with one titanium washer for 1/4" thick aluminum plates and two SS316 washers for 1/8" thick aluminum plates.

The 4 K shields are made out of Cu101 and connected to the second stage of the pulse tube by also about twenty 7 cm long flexible copper thermal heat links. The temperature difference across the thermal heat links is calculated to be about 0.75 K with 1.5 W heat load. We made the 4 K shields as big as possible to get the maximum volume possible at the cold temperature. Super-insulation with very high reflectivity is wrapped around both the 75 K shields and the 4 K shields to reduce the heat-load from the blackbody radiation on the shields.

The number of holes on the radiation shields is minimized to prevent leakage of blackbody radiation from the warmer side. This, however, interrupts the gas flow between layers and the pressure between the shields could be higher to diminish or destroy the buffer-gas beam. To maximize the gas conductance while blocking the blackbody radiation, we put several (two on the 75 K shields and one on the 4 K shields) chevron baffle assemblies on the shields (Fig. 3.2.5). Each baffle is bent 120 degrees and 9 baffles are stacked with just enough separation to block any line-of-sight from outside to inside, forming one assembly. The conductance of

one assembly for He gas at 4 K is ∼60 liters/second. To minimize blackbody radiation from the chevron and to prevent helium atoms from heating, it is made out of Cu101 for good thermal conductivity to the shields and throughout the assembly.

Pumping of the residual He buffer-gas, which is hard to pump out due to its light mass, in the cryogenic section was achieved with activated charcoal cryo-pumping. Charcoal sorbs have huge surface area and absorb He gas effectively at 4 K. We glued a lot of charcoal sorbs on Cu101 plates using Stycast 2850 to ensure good thermal conductivity and bolted the sorb plates inside the 4 K shields (Fig. 3.2.6).

The 1 K pot is the coldest spot in the chamber and we would like to keep the thermal load on it at the minimum level for a long run time and a lowest possible base temperature. To thermally isolate the pot, it is hung from the top flange of the blue beam box via a stainless steel tube (VCR connections). The tube is heat-sunk to 75 K shields and 4 K shields by clamping flexible heat links around it. To use the big space inside the 4 K shields efficiently, we have a 10.5" long Cu101 plate (0.5" thick) that is heat-sunk to the 1 K pot using flexible copper heat-links so that we can move the buffer-gas cell ∼8" along the beam line if you want. The cell is attached to this 1 K copper plate via another copper plate. The 1 K pot hold-time is ∼5-8 hours with typical heat load of the experiment (7 mJ YAG at 2 Hz, 4 sccm buffer-gas flow, with or without slowing lasers).

3.2.2 Stem region - intermediate region between the cryo-region and the MOT region

Between the beam box and the MOT chamber, we had a intermediate region (called "stem region") for better pressure in the MOT chamber and beam diagnostics. It consists of a 6-way cross with KF fittings and a turbo pump (TV-551 from Agilent) with compression ratio of 10^7 for He gas. The typical vacuum in this region is 10^{-7} Torr. This region is design so that it can be easily removed. ^{6}Li data are taken with the stem region and the CaF data are taken without the stem region.

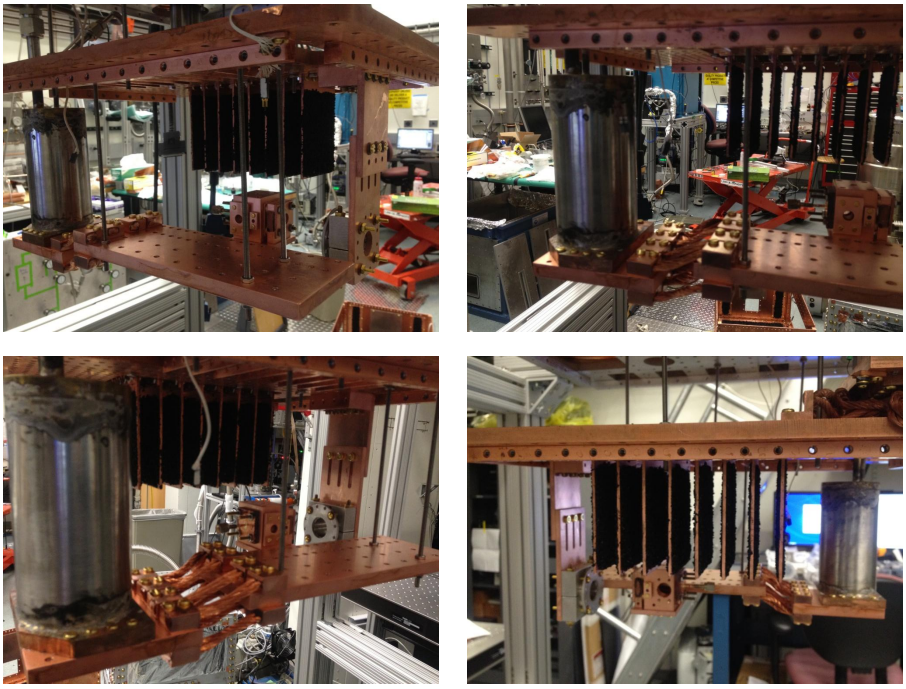

Figure 3.2.6: Photos of the 1 K pot, the 1 K plate, sorb plates, and the cell

3.2.3 MOT chamber - the MOT region where the MOT is located

Located after the stem region is the MOT chamber with CF sealings where the MOT is located. The main body is a standard stainless steel 6" spherical octagon vacuum chamber from Kimball physics, so that we have enough ports to send all the MOT laser beams. Each port for the MOT beams has a nipple on it and that reduces scattered light from the windows to the MOT center. The chamber is also connected to a turbo pump (TV-551 from Agilent) to get rid of any remaining buffer-gas inside the chamber. The typical vacuum when we are running is $\sim 2 \times 10^{-8}$ Torr with the stem region which gives a background gas limited lifetime of $\tau > 1$ s.

Later on, we removed the stem region to shorten the distance between the cell and the MOT center for brighter beam (Fig. 3.2.7). In return, the background pressure went up slightly to 5×10^{-8} Torr since more buffer-gas is present near the MOT center. The lifetime with this pressure would be $\tau \sim 450$ ms.

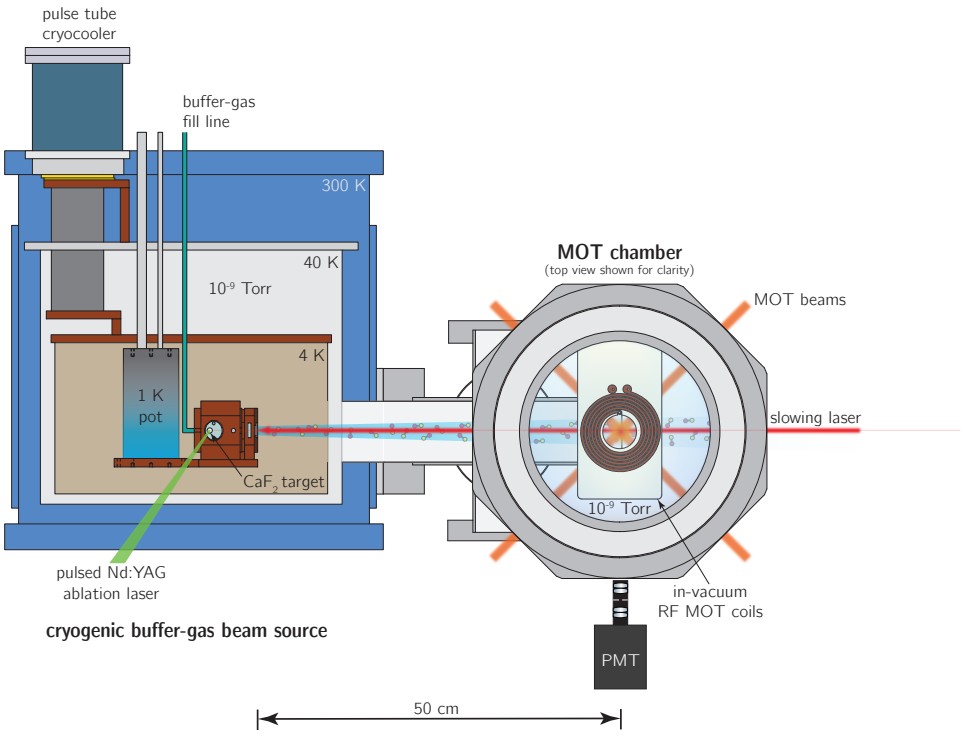

Figure 3.2.7: Overview of the experimental setup without stem region. It is not to scale.

3.3 Lasers

The wavelengths we need for CaF molecules are 606 nm (main), 628.5 nm (1st repump), and 628.1 nm (2nd repump). Additionally, the main and the 1st repump lasers need to produce high power. Unfortunately, none of these are convenient wavelengths where one can use diode lasers easily. There are many diodes at around 637 nm (even at 633 nm from 2014) with relatively high power of up to 200 mW which can be cooled down to about -20 C (∼0 C for 633 nm diodes) and would lase at around 628 nm. To get the wavelengths we need, we setup several dye lasers and cold external-cavity diode lasers (ECDLs). We also bought an OPO (optical parametric oscillator) + SFG (sum frequency generation) laser system at 606 nm as the main laser for the MOT beams. To detect slowed molecules, we also use two-photon transition where a Ti:sapph laser is used to pump molecules from the excited state $A\,^2\Pi_{1/2}$ to a higher excited state $C\,^2\Pi_{1/2}$. All the lasers are locked to the wavemeter using Labview PID program. The lasers and their roles are summarized in Table 3.1.

	MOT	Slowing
Main	OPO + SFG	Dye
1st repump	Dye	Dye
2nd repump	cold ECDL	cold ECDL
A-C		Ti:sapph

Table 3.1: List of lasers for CaF molecule.

3.3.1 Dye lasers and Ti:sapph laser

We have five 899 ring cavities - four dye and one Ti:sapph - that are pumped by three Verdi lasers. Two 10 W Verdi lasers (V-10) pump two dye lasers (the main and the 1st repump slowing lasers) and one 18 W Verdi (V-18) laser is shared by two dye lasers (the 1st repump MOT laser and a backup laser) and the Ti:sapph laser for the A-C transition or other atomic transitions. Rhodamine 590 (Rhodamine 6G) dye from Exciton is used to generate 606 nm light, and Rhodamine 610 (Rhodamine B) dye from Exciton for 628.5 nm. We usually get about 1 W at 606 nm out of the laser and 400 mW at 628.5 nm.

3.3.2 Cold external cavity diode lasers

The 2nd repump laser is not required to be as high power as other lasers and ∼100 mW output power is enough. High power 626 nm light has been obtained by cooling a diode laser down to around -31 C [84] and we followed their example to generate 628 nm light from cold ECDLs. We are using HL63133DG (637 nm, 170 mW, single mode) diode lasers from Thorlabs and cooled them down to -20 to -30 C depending on diodes and getting ∼100 mW at 628 nm. Recently, HL63163DG (633 nm, 100 mW, single mode) has become available also from Thorlabs. Temperatures about 0 C is enough to get 628 nm using this diode.

3.3.3 OPO + SFG laser

Dye lasers have great advantages of tuning ability, wide spectrum, and high power. However, due to the liquid media inside the cavity, it has more power fluctuation than solid state lasers. Also, the maintenance is time-consuming. People have been developing solid state

laser systems for orange colors which diode lasers don't provide. There are two main ways to generate 606 nm using solid systems. One is the second harmonic generation from 1212 nm (for example, TA-SHG pro from Toptica) and ∼800 mW at 606 nm has been achieved. The other option uses two stages of non-linear process - OPO + SFG, the one that we are currently using (Argos^{TM} Orange Model 2400 CW OPO from Lockheed Martin Aculight Corp.). Here, 1064 nm fiber laser is amplified and divided into two colors by OPO - 1408 nm and 4355 nm. 606 nm light is generated by summing the pump laser 1064 nm and the signal 1408 nm. The output power is $>$ 1.2 W at 606 nm with reasonable mode-hop free tuning range (about 20 GHz in spec, about 5 GHz easily achieved on daily basis).

3.3.4 White-light electro-optical modulator

Instead of a Zeeman slower, we use frequency-broadened "white-light" slowing laser to slow down the molecules. Frequencies of the slowing lasers are broadened using a home-built resonant electro-optical modulator (EOM) with the resonance at 7 MHz (for ^{6}Li) or 4.5 MHz (for CaF) and Q of about 50. This EOM, named as "white-light EOM", is designed to be over-driven to form about 50 sidebands.

The EOM crystal is Mg doped lithium niobate ($LiNbO_3$) with dimension of 1 mm thickness and 6 cm length to increase the modulation depth. Sides of the crystal are coated with Au and Cu electrodes are plated on top of it. A tunable resonant circuit (4 MHz up to 8 MHz resonant frequency) is connected to the crystal and we can put several hundreds of mW power into the crystal. Fig. 3.3.2 shows the sidebands of the slowing laser generated by the white-light EOM. Here, the EOM resonance is at 4.5185 MHz and the overall frequency broadening is ∼200 MHz.

3.3.5 Pockels cell for polarization switching

To depopulate the dark magnetic substates during the photon cycling, we implemented polarization switching of the lasers for MOT beams using a Pockels cell (Model 350-160-01-

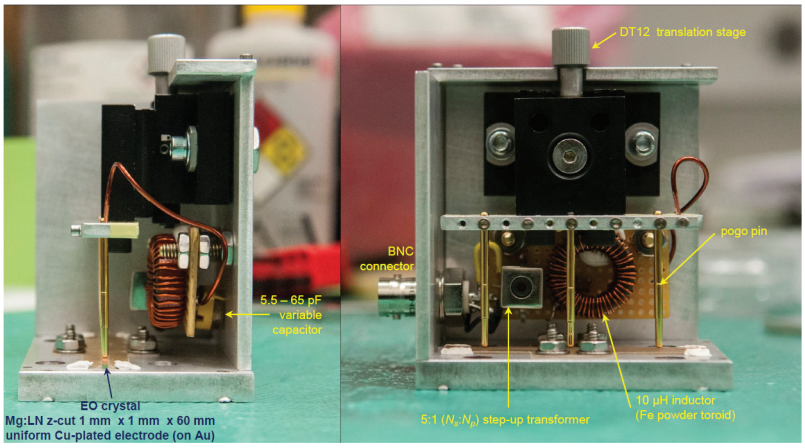

Figure 3.3.1: Photo of the white-light EOM assembly (Courtesy of A. Ravi)

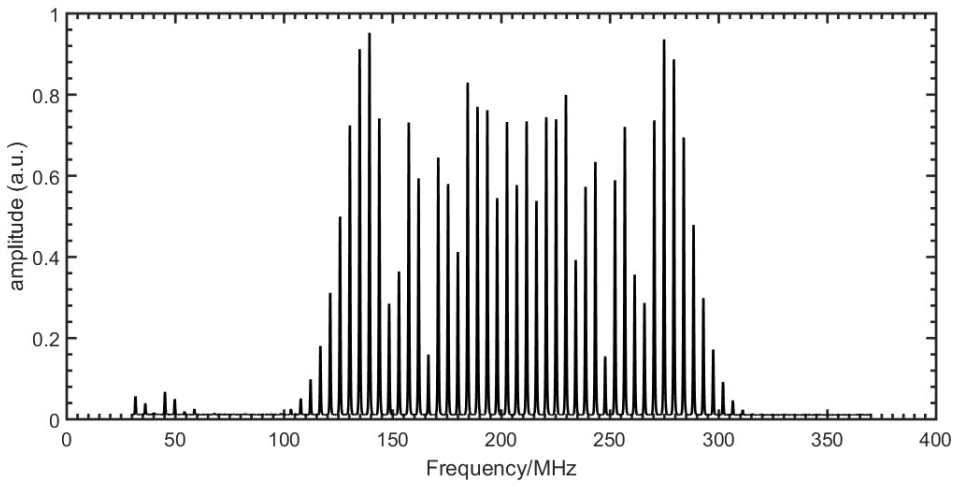

Figure 3.3.2: Spectrum of slowing laser after the white-light EOM from a beat-note measurement. The modulated light by the white-light EOM is beat with the unmodulated light shifted by about 207.1 MHz. 0 MHz in this plot is the unmodulated laser frequency.

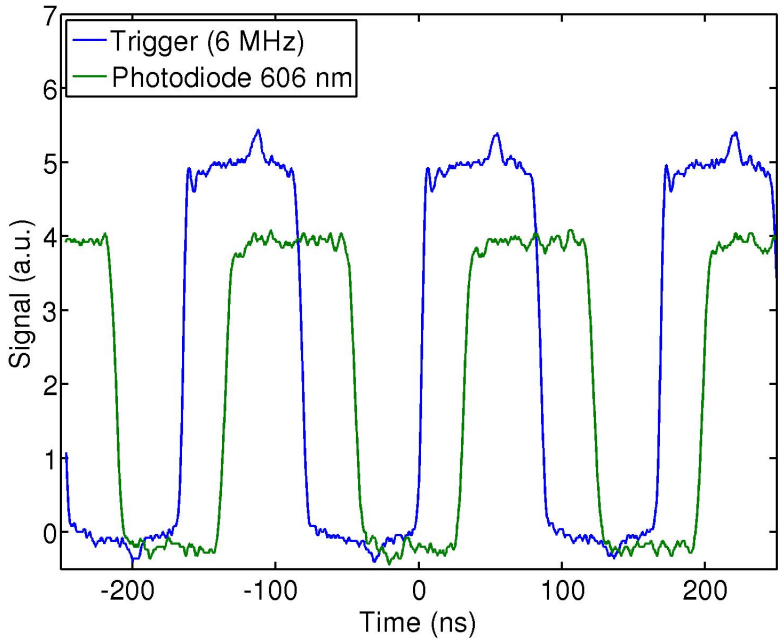

Figure 3.3.3: Polarization switching test using a Pockels cell. The polarization of 606 nm laser is switched at 6 MHz and the transmitted beam through a polarizing beam cube is detected by a fast photodiode.

RP EO Modulator with Model 25D driver from Conoptics). We tested the Pockels cell at the switching frequency of 6 MHz by sending 606 nm light through. The beam then passed a polarizing beam cube and the transmitted beam is focused onto a fast photodiode (Thorlabs PDA10A). Fig. 3.3.3 reveals that the Pockels cell works fine at 6 MHz.

3.4 Transverse magnetic field

A transverse magnetic field is used to let the dark magnetic substates precess back to bright states for the white-light slowing. We had two home-made coil bundles in Helmholtz configuration between the blue beam box and the MOT chamber and one L shaped coil bundle on top of the MOT chamber for slowing. All coils are connected in series and 4 Amp current is being used. The measured transverse magnetic field we used/will use to mix the magnetic dark substates are summarized here. We calibrated "0 Gauss" using the Earth field so that it reads same value with opposite sign when we flip the hall probe. The Earth field we measure

Position	B_x (Gauss)	B_y (Gauss)	B_z (Gauss)
1 cm from gate valve	10.2	1.8	NA
~ 10 cm from gate valve	9.3	1.5	NA
center of MOT chamber	-2.3	-5	-1.6

Table 3.2: Transverse magnetic field for mixing dark states used in the CaF slowing experiment.

with this probe was 0.4 Gauss, which is off by ∼0.1 Gauss. All the measurements below are trustful ± 0.1 Gauss. The definition of the coordinates are as follows.

- Definition of direction : using slowing laser axis
  - +z : toward the beam box
  - +y : toward the ceiling
  - +x : toward the machine shop

3.4.1 Slowing configuration : with two parallel coils around the gate valve + 90 degree bent L shape top coil on the MOT chamber

This is the transverse field configuration we used when we took the slowing data in Ch. 6. The measured B field values are summarized in Table 3.2. The $\sqrt{2.3^2 + 5^2 + 1.6^2} = 5.7$ Gauss offset in the MOT chamber is not good for the AC MOT and we decided to run without the top coils when we look for the MOT for CaF.

3.4.2 MOT configuration : with only two parallel coils around the gate valve

Table 3.3 is the summary of the magnetic field without the L shaped top coil. The same 4 Amp current was put through the two Helmholtz coil bundles. We don't have a substantial magnetic field gradient in the MOT changer without the top coil while keeping reasonable field strength between the cell and the MOT chamber. We successfully repeated white-light

Position	B_x (Gauss)	B_y (Gauss)	B_z (Gauss)
1 cm from gate valve	10	-3	NA
~ 10 cm from gate valve	3.5	-1.6	NA
center of MOT chamber	-0.7	-0.2	-0.2
+2 cm in y from MOT	-0.5	-0.37	-0.06
-2 cm in y from MOT	-0.6	-0.53	-0.3
+2 cm in z from MOT	-0.7	-0.3	-0.32
-2 cm in z from MOT	-0.65	-0.34	-0.2
+2 cm in x from MOT	-0.65	-0.42	-0.19
-2 cm in x from MOT	-0.48	-0.42	-0.23

Table 3.3: Transverse magnetic field for mixing dark states without the L shaped top coils for the MOT experiment.

slowing of CaF with this transverse field configuration, confirming weakened field strength near the MOT center doesn't harm the experiment.

3.5 In-vacuum AC MOT coils

The polarization switching of the lasers to depopulate the dark states is not enough to make an AC MOT. The switching of the anti-Helmholtz magnetic field (MOT field) is also required for the detuning of the magnetic substates to be matched properly. As a consequence, one needs to change the direction of the current going through the coils rapidly (at MHz), which is an engineering challenge. For fast switching, the coils should have small inductance and capacitance, which leads to a small size. As a result, the coils should be inside the vacuum chamber and be UHV compatible. We collaborated Jun Ye's group at JILA to design in-vacuum coils that can switch the MOT field direction at MHz frequencies without outgassing.

The coils are made out of 0.85 mm thick copper sheet that was cut to a spiral coil shape by an electrical discharge machine. The inner diameter of the coils is about 15 mm and the outer diameter is about 30 mm. There are 6 turns for each coil and the width of the coil is 1 mm. The coils are bonded to 1.5 mm thick Alumina boards by Stycast 2850. There are 4 coils total - 2 on the upper board and 2 on the lower board. The coils on the same board are attached on each side of the board and wired to Helmholtz configuration inside

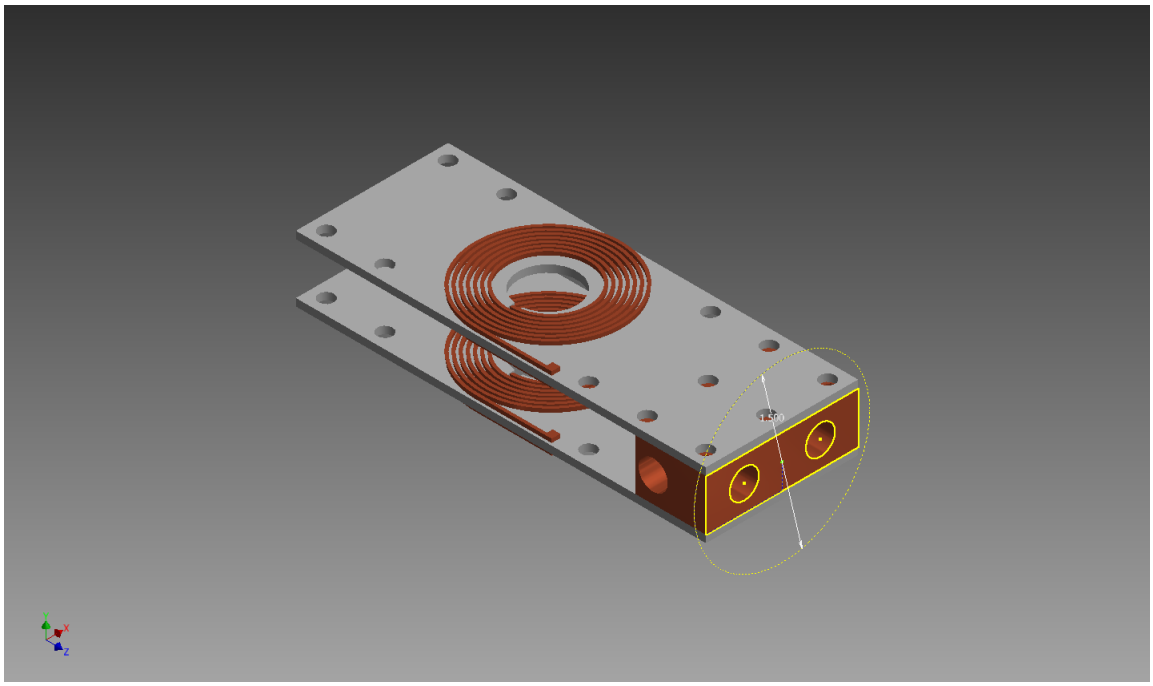

Figure 3.5.1: Design of AC MOT coils (Courtesy of N. R. Hutzler)

the vacuum. Each board has wires connected to the outside of the chamber through an electrical feedthrough so that we can wire the two boards in any way externally - in series, in parallel, Helmholtz, or anti-Helmholtz. We used in-series anti-Helmholtz configuration for ^{6}Li AC MOT and are planning to use the same configuration for CaF AC MOT too.

The alumina board were chosen as a substrate for two reasons - low outgassing rate and good thermal conductivity. As a ceramic, alumina does not outgas much. It is still porous and can absorb water, which takes a long time to pump out. We bake the whole coil assembly in an oven at 120 C for a few hours before putting it in the MOT chamber.

When the current through the coils is switched at high frequencies, substantial heat is generated. High thermal conductivity of Alumina helps to carry the heat out of the chamber effectively. The Alumina boards are mounted on a aluminum block, which is mounted to a copper block feedthrough (power feedthrough for 600 Amp, 3000 Volts, EFT0313753 from Kurt-Lesker). On the air-side of the feedthrough, we put a small passive heat sink to further increase the cooling power. With this setup, we barely observe temperature increase when we run the coils in AC mode at 1 MHz.

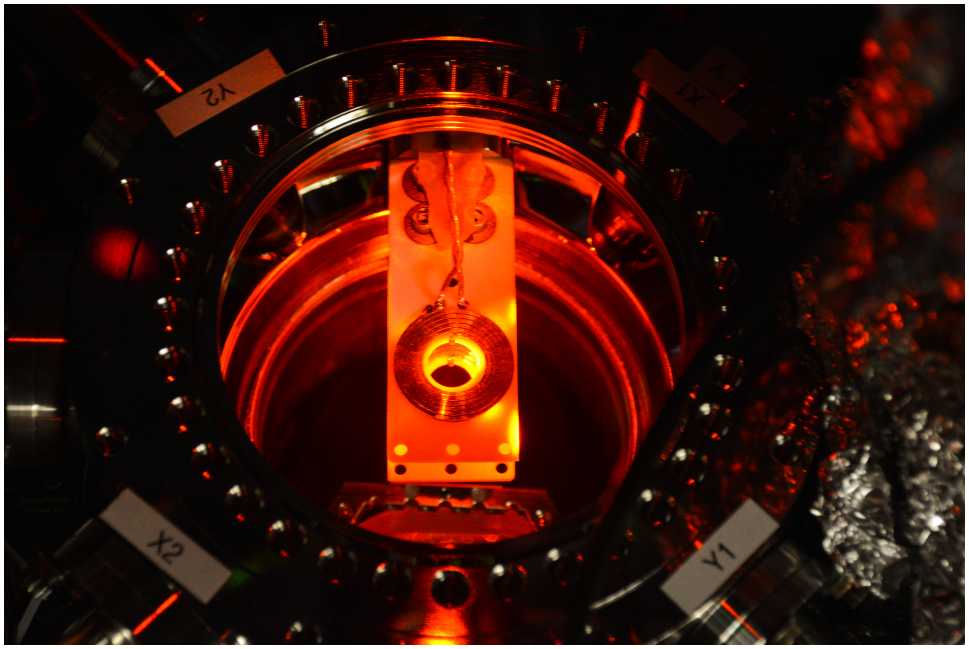

Figure 3.5.2: Photo of the AC MOT coils inside the MOT chamber illuminated by the MOT beams

There is a resonant circuit outside of the chamber to tune the resonant frequency of the switching. We estimated that the MOT coil assembly has 100 pF, 2.8 μH, and 0.3 Ω by comparing the real resonant frequencies with the simulation. At around 1 MHz switching frequency, 2 Amp input currently gives peak to peak voltage of 55 Volts.

To confirm the magnetic field generated by the MOT coils, we measured the field between the coils in DC mode with 1 Amp current using a hall probe. The data is shown in Fig. 3.5.3. The coils with 1 Amp current form nice quadrupole magnetic field with about 10 (5) Gauss/cm for axial (radial) direction.

3.6 Detection

We detect the fluorescence from molecules or atoms using two detectors - a camera and a photomultiplier tube (PMT). The EM CCD (electron multiplying charge coupled device) camera from Andor (DL-604M-OEM) is used to take pictures for various MOTs for atoms throughout the experiment. We use two PMTs in this experiment. One is Hamamatsu

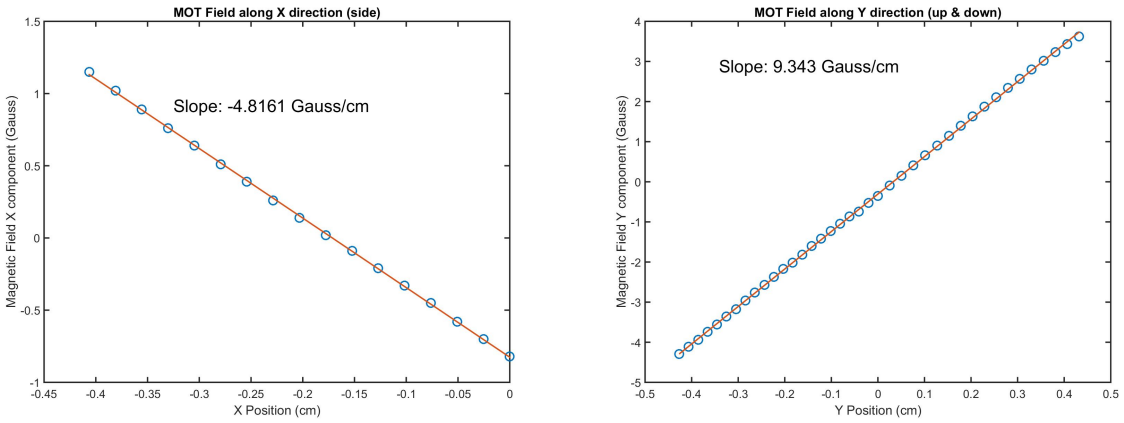

Figure 3.5.3: Magnetic field generated by the MOT coils with 1 Amp current. X direction is the radial axis and Y direction is the axial direction.

R8900U-20 for visible photons and the other is Hamamatsu R7600P for UV or blue photons.

The two detectors have their own advantage - the camera has the spatial information and the PMT has the time information. To use both of them, we combined the two detectors using either a 50:50 beam splitter or a dichroic mirror (Fig. 3.6.1). The 50:50 beam splitter ensures that the signal we see on one detector is the same signal on the other so that we can extract both spatial and temporal information of the signal at the same time. We also have an iris on the image plane so that we can cut unnecessary part of the image by closing the iris looking at the camera. A dichroic mirror that reflects UV light is in place when we want to detect the two-photon UV signal from CaF molecules using PMT and detect 606 nm fluorescence using the camera. All light-collecting optics and detectors are connected using lens tubes to be light-tight.

3.6.1 Light collection and imaging

We use four lenses (two for image the MOT center onto a plane where the iris is, the other two to image the iris and the MOT center onto the detectors) to image near the MOT center area onto the camera or PMT. For ^{6}Li data, we had the first 1" lens right outside of the MOT chamber, collecting $\sim$3 out of 1000 photons emitted from the MOT center area. To

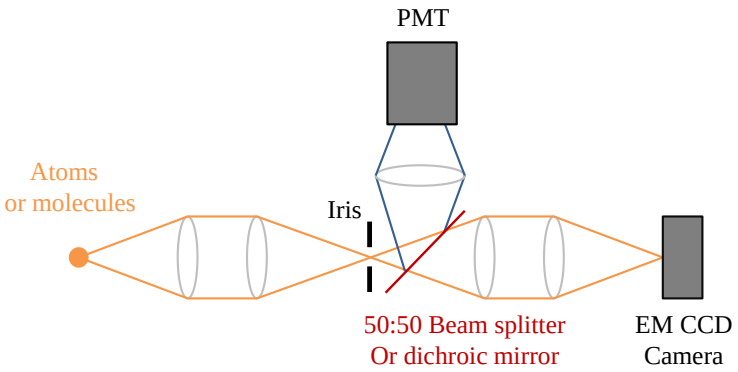

Figure 3.6.1: Schematic of the Detector assembly.

improve the collection efficiency for molecules, we put a 2" lens inside the vacuum chamber (Fig. 3.6.2) and the collection efficiency increased to 1/50.

3.6.2 Two-photon detection

We use two-photon absorption ($X\,^2\Sigma(N=1)$ - $A\,^2\Pi_{1/2}(J=3/2,+)$ - $C\,^2\Pi_{1/2}(J=1/2,-)$) to excited molecules to the C state and collect blue photons emitted when the molecules decay from the C state to the X state (Fig. 2.2.1). This gives us minimal background scattering. This process is not a closed cycle and we expect < 1 photon per molecule. Once the molecule emit the blue photon, it is lost to $X\,^2\Sigma(N=0,2)$ states.

We chose $A\,^2\Pi_{1/2}(J=3/2,+)$ states as intermediate states so that the slowing lasers which address molecules to the $A\,^2\Pi_{1/2}(J=1/2,+)$ states don't alter the UV signal other than actual slowing and optical pumping among ground states.

In the experimental setup, we send the $X-A$ laser transverse to the molecular beam and the $A-C$ laser 45 degree to the molecular beam (Fig. 3.6.3). The $A-C$ transition, which has no hyperfine splittings bigger than linewidth, gives us a clear molecules' velocity information from the Doppler shift.

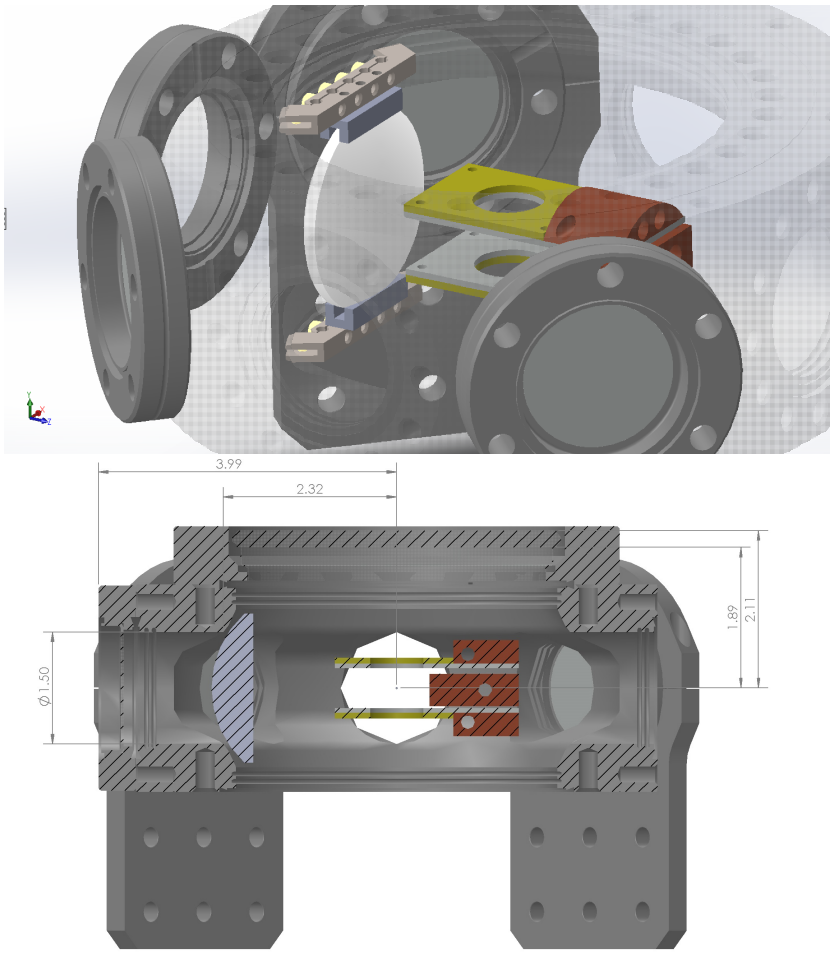

Figure 3.6.2: Image of the in-vacuum 2" lens. (Courtesy of L. Anderegg)

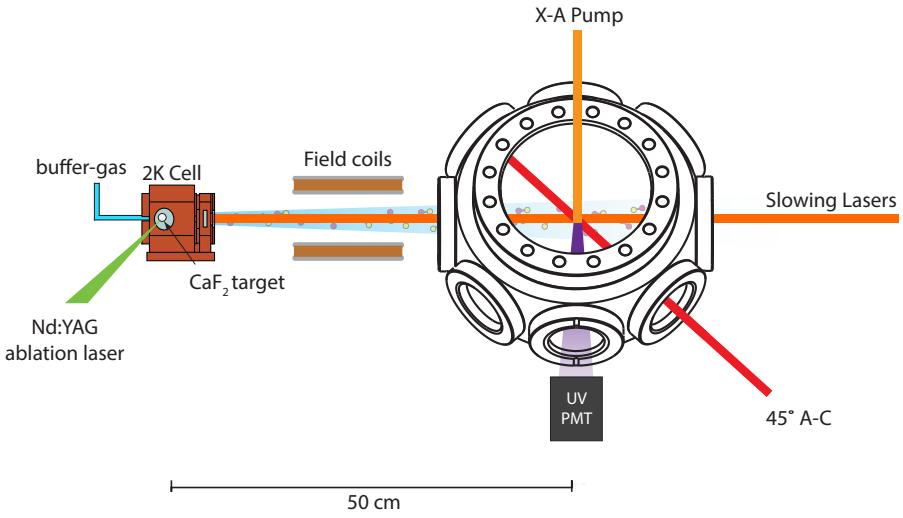

Figure 3.6.3: Experimental Setup for two photon detection.

3.6.2.1 Two photon absorption probability

Assuming a single intermediate state k between the initial state i and the final state f, the transition rate for two photon absorption is [85]

$$W_{2\gamma} \sim \frac{1}{2\,\hbar^4\Gamma_f}\left(\frac{(d_{ik}E_1 d_{kf}E_2)^2}{\Delta^2 + (d_{ik}E_1/\hbar)^2}\right) \tag{3.6.1}$$

, where $E_{1,2}$ denotes the electric field from each laser coupling the initial state i and the intermediate state k (E_1), the intermediate state k and the final state f (E_2). Γ_f is the linewidth of the final state f.

The four hyperfine states in the ground $X\,^2\Sigma(N=1)$ state complicates the two-photon absorption spectra. As visible in Fig. 3.6.4, we see four peaks from the four hyperfine states in $X\,^2\Sigma(N=1)$ state when the $A-C$ laser is fixed and the $X-A$ laser is scanned. The $X\,^2\Sigma(N=1) - C\,^2\Pi_{1/2}(J=1/2,-)$ energy separations are measured as 905.402197 THz, 905.402230 THz, 905.402275 THz, and 905.402354 THz.

We also see four peaks, which corresponds to the ground X state's hyperfine splittings, in the other case, where we scan the $A-C$ laser while setting the $X-A$ laser fixed in frequency

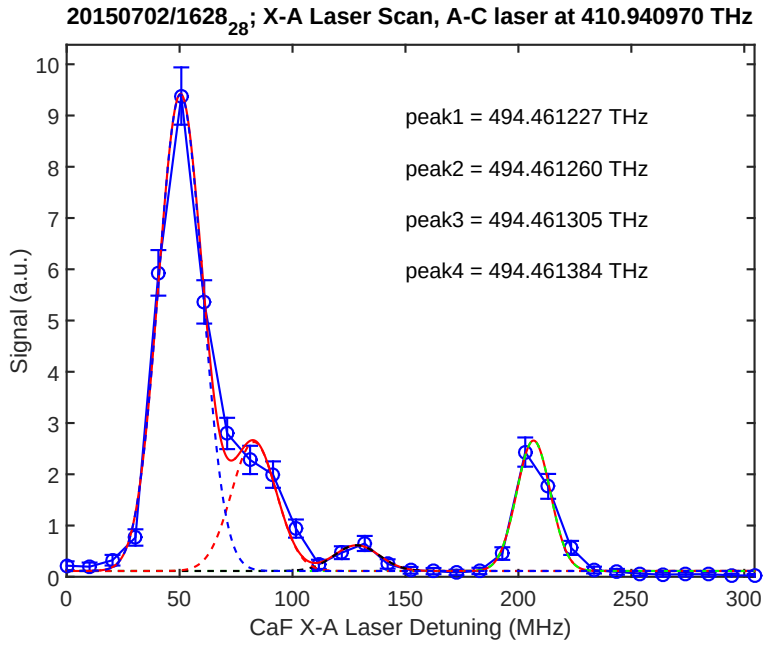

Figure 3.6.4: UV signal (blue line) as a function of the $X - A$ laser frequency, integrated from 1.25 ms to 12.25 ms after the YAG. The red line is a fitted line using four Gaussian functions where each Gaussian function is depicted as a dotted line. The errorbar shows the shot noise.

(Fig. 3.6.5), even though both the $A\,^2\Pi_{1/2}$ and the $C\,^2\Pi_{1/2}$ states' hyperfine structures are narrower than the linewidth. This is because a two photon transition can happen whenever the laser frequencies sum up to the separation between the initial and the final states with the strength determined by the detuning from the intermediate state (Δ in Eq. (3.6.1)).

These multiple resonances in the $A - C$ frequency for two photon transition complicates our velocity analysis since we are relying on the Doppler shifts of the $A - C$ transition, which are similar order as the splittings. A signal change due to slowing lasers could be either from Doppler shift of slowing effect or from optical pumping to other hyperfine states with same velocity. To get the clearest information regarding molecules' velocity, we use the bluest transition (905.402354 THz) to measure the slowing effect. If molecules in this state are slowed by the slowing lasers, they should emit bluer photons than the beam signal from any hyperfine states and this cannot be explained by other mechanism.

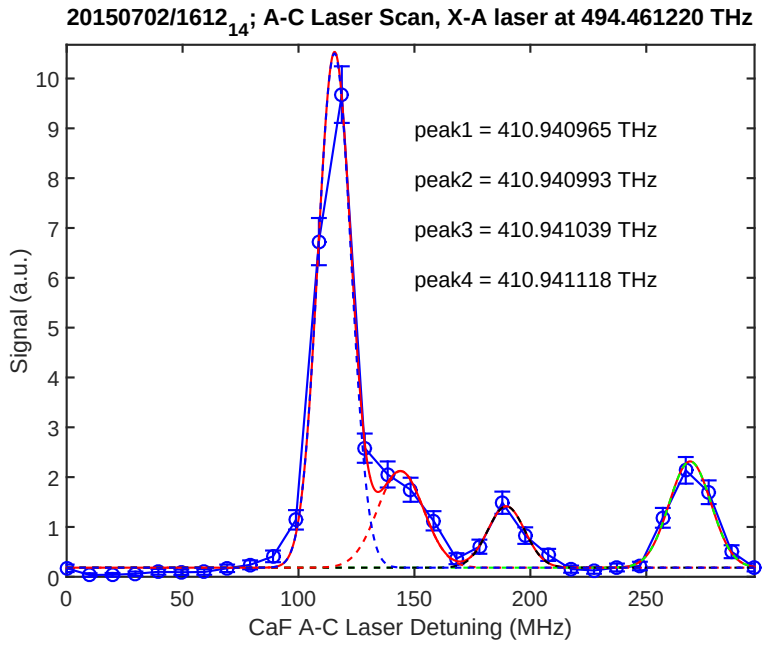

Figure 3.6.5: UV signal (blue line) as a function of the $A - C$ laser frequency, integrated from 1.25 ms to 12.25 ms after the YAG. The red line is a fitted line using four Gaussian functions where each Gaussian function is depicted as a dotted line. The errorbar shows the shot noise.

3.6.2.2 Error bar

We are using photon counting mode of our PMT (Hamamatsu R7600P) which has a low dark count rate (45 Hz spec, about 5 photons/130 ms). Our dominant source of signal intensity error is quantum fluctuations in the total number of photons we counted. We average our signal and the error is reduced down to $\sqrt{N/n}$, where N is the total number of photons and n is the number of average that varies from 30 to 1000 usually. The statistical errorbars in Fig. 3.6.4 and Fig. 3.6.5 are calculated in this way.

3.6.2.3 Saturation intensity estimation

The dipole transition moment between the $A\,^2\Pi_{1/2}$ state and the $C\,^2\Pi_{1/2}$ state is unknown, but people have observed that it is weaker than $B\,^2\Sigma - C\,^2\Pi_{1/2}$ and $B'\,^2\Delta - C\,^2\Pi_{1/2}$ transitions [74]. We need to well saturate the $A - C$ transition so that we can promote as many molecules in the excited A state as possible within the short lifetime of the A state, which is about 19

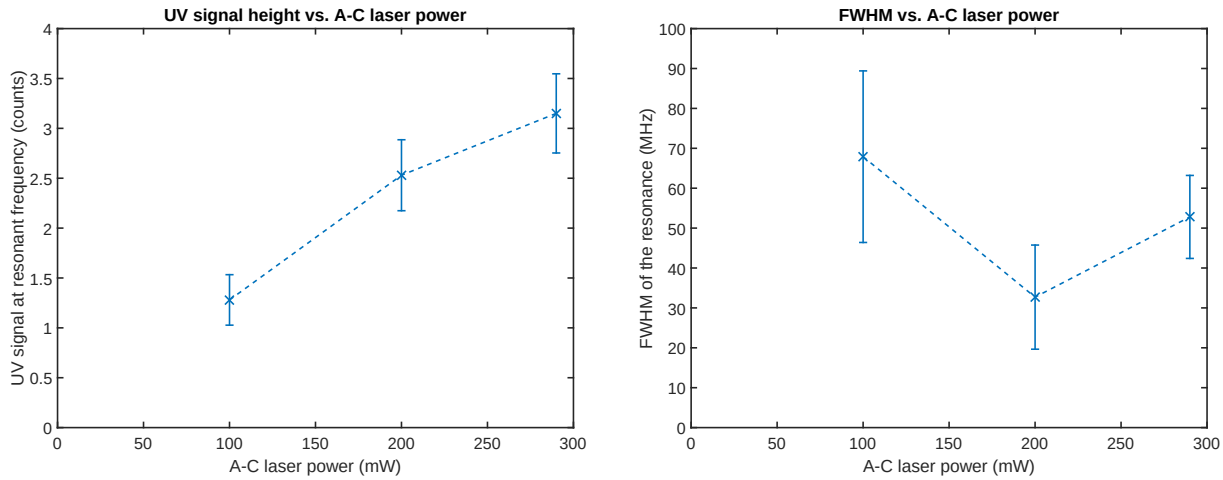

Figure 3.6.6: UV signal dependence on A-C laser power from data taken on 20150409. The FWHM error bar indicates 95% confidence values.

ns. We measured the UV signal dependence on the A-C laser power. When the A-C laser power increased from 100 mW out of fiber to 200 mW, the signal height linearly increased indicating that we are not saturated yet. However, the size of the UV signal with 290 mW of the A-C laser didn't change much compared to 200 mW one. The linewidth also didn't change much, indicating that this transition is not actually saturated but some other factors - like the interaction time between the A state molecules and the laser - are limiting the signal. We also checked the $X - A$ laser power dependence and 1 mW is enough to saturation the signal height for that transition. Unfortunately, we don't have the linewidth measurement of that line so far. We usually use 10 mW for that transition in the experiments.

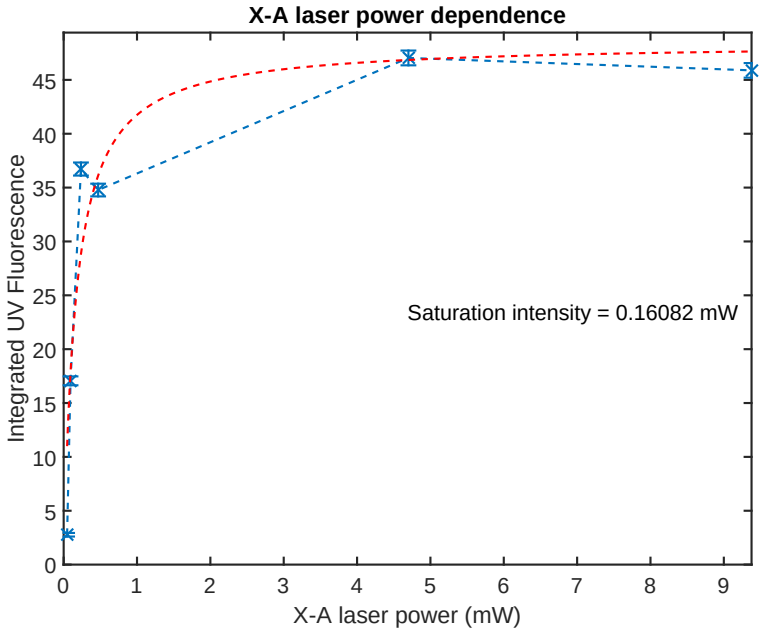

Figure 3.6.7: UV signal height dependence on X-A laser power from data taken on 20150427. 100 m/s molecules were monitored.

Chapter 4

Slow Beam Source : Two-Stage Buffer-Gas Beam Source

4.1 Beam velocity measurement

The procedure to measure the beam forward velocity is as follows. We first find the resonance of the transition that we use for detection from a transverse laser scan in the MOT chamber. The 1 cm aperture on the 75 K radiation shields collimates the atomic/molecular beam so that the Doppler broadening due to transverse velocity is negligible (transverse velocity less than 1 m/s for 50 m/s forward velocity object). An example of a typical transverse scan is shown in Fig. 4.1.1.

The natural linewidth of the transition is one of the sources of the uncertainty of the velocity measurement. Another possible cause is the laser frequency instability. Fig. 4.1.2 shows an example of the laser stability during the scan. Since we took 20 averages for the scan in Fig. 4.1.1, the averaged FWHM goes down to $7.5723/\sqrt{20} \sim 1.7$ MHz, which is smaller than the natural linewidth of the atoms/molecules we use (7 - 30 MHz). This is the case through out this thesis and the dominant reason for the uncertainty of the velocity is the natural linewidth of the transition.

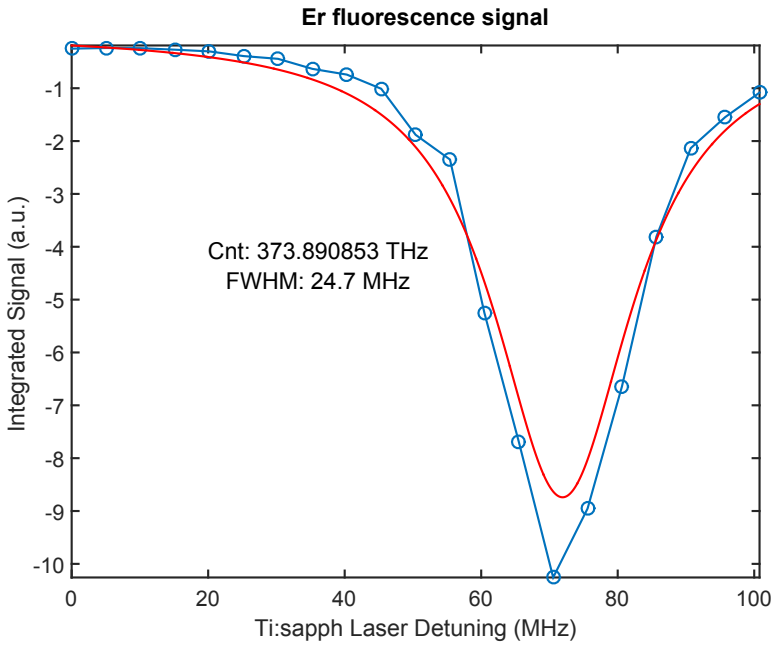

Figure 4.1.1: Transverse laser scan for Er 400 nm transition in MOT chamber 50 cm downstream. The red curve shows a fitted line using a Lorentzian function.

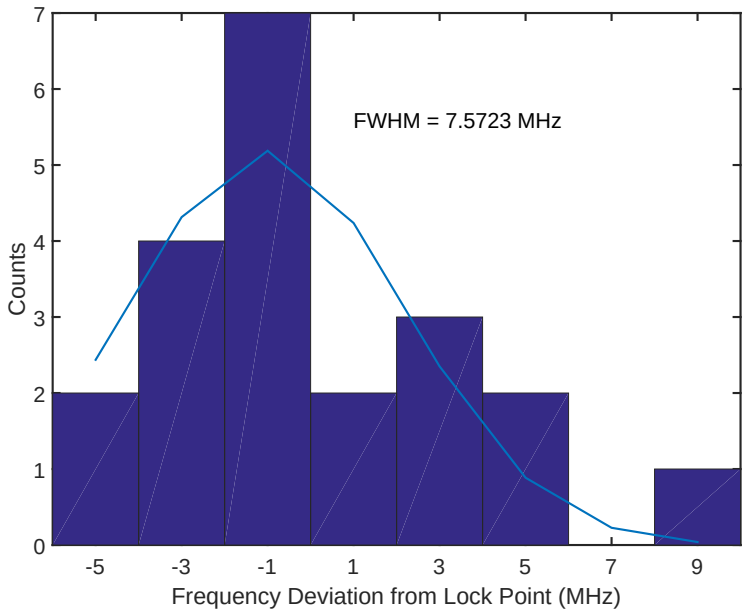

Figure 4.1.2: Ti:sapph laser stability during the scan in Fig. 4.1.1

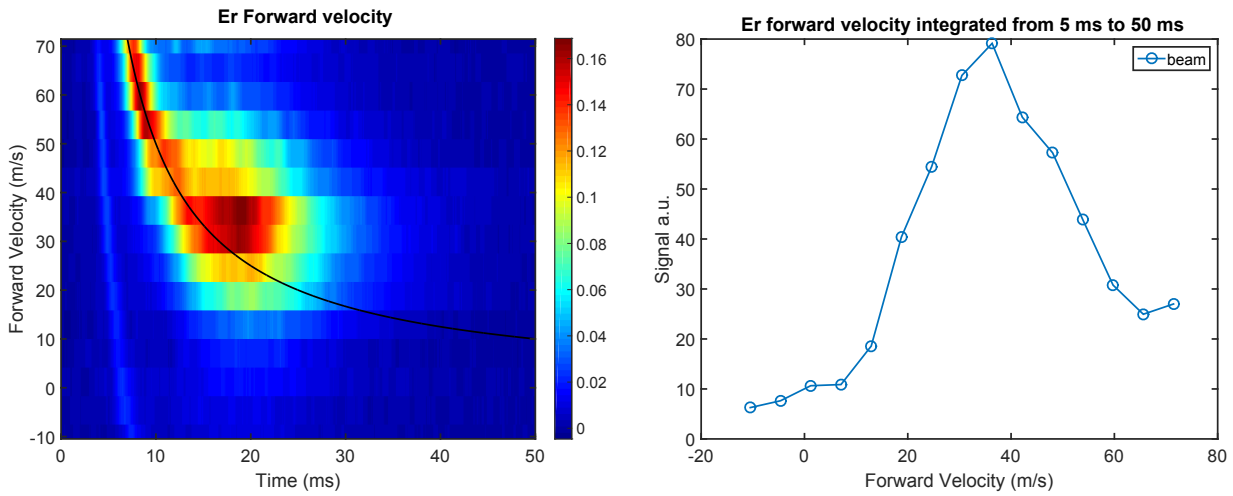

Figure 4.1.3: Forward velocity of Er atoms in the 2nd generation experimental setup. The left figure is 2D plot with both time and velocity information. The time integrated signal from 5 ms to 50 ms is shown in the right plot.

The Er beam forward velocity is shown in Fig. 4.1.3. We see a lot of atoms down to 30 m/s, which is close to the thermal forward velocity of effusive beam of Er at 4 K (20 m/s).

The forward velocity can change dramatically according to the cell geometry. Here, we studied two cases - one without a diffuser and 0.5" distance between the buffer-gas fill line and the target, and the other with the diffuser and 1.25" distance between the buffer-gas fill line and the target. We saw dramatic difference in forward velocity for the two cases. Fig. 4.1.4 shows the two CaF beam velocities with the different geometries. It is clear that the longer distance between the target and buffer-gas line and the diffuser make the molecular beam slower. The more distance the buffer-gas travels in the cell means that the He gas spends more time thermalizing to the cell temperature at 1 K. The diffuser prevents the buffer-gas from going ballistically through the cell. Both of these should help the molecules thermalize better with the buffer-gas and, as a consequence, with the cell.

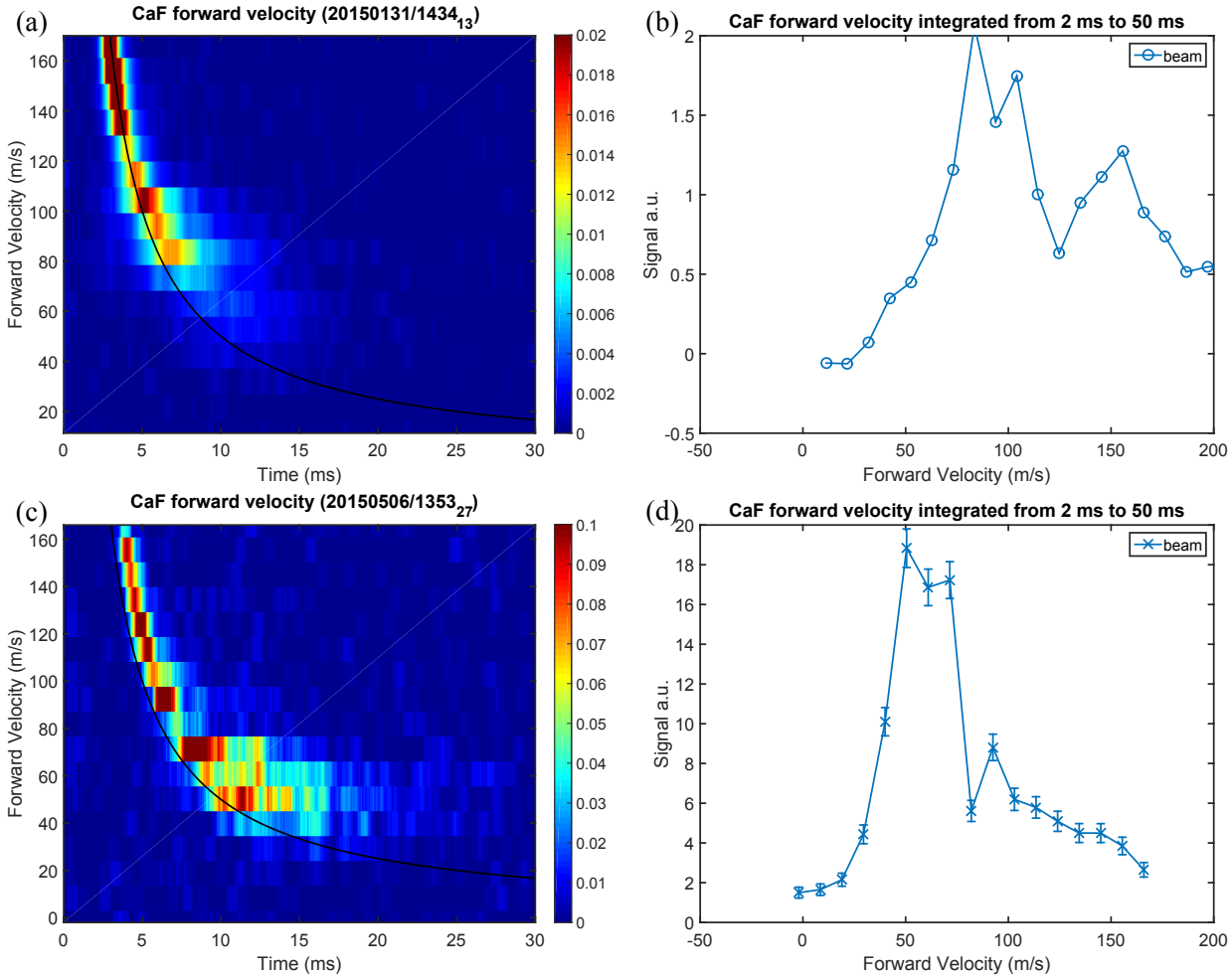

Figure 4.1.4: Forward velocity of CaF molecules for different cell configuration. (a)(b) Cell without the diffuser and 0.5" separation between the fill line and the target. (c)(d) Cell with the diffuser and 1.25" separation between the fill line and the target.

4.2 Magneto-optical traps for atoms directly loaded from slow buffer-gas beam

The buffer-gas beam source inherently has a lot more buffer-gas in the beam than the species we are interested in. One needs to make sure that these ^{4}He atoms don't prevent the atoms/molecules from forming the magneto-optical trap (MOT). There are two kinds of ^{4}He gases in the MOT chamber - one at cold temperature and the other at room temperature after bouncing off the wall.

When a ^{4}He atom at 2 K (thermal velocity v_{thermal} ∼90 m/s) collides with a CaF molecule at rest, the CaF molecule moves at ∼10 m/s after the collision which is about the capture velocity of the expected MOT. However, if the ^{4}He atoms is at 300 K (thermal velocity v_{thermal} ∼1100 m/s), the CaF molecules would gain 140 m/s velocity after the collision and would escape from the trap. There have been studies on the effect of background gas collisions on the MOT [86] but no studies has been done regarding the effect of cold background gas. One first needs to make sure that the buffer-gas beam is compatible with a MOT.

For that, we decided to make a MOT for atoms from the buffer-gas beam. We chose Yb atoms as our first test species due to its excellent ablation properties and laser availability in the lab. Yb atoms are a lot heavier than CaF molecules so that they are more immune to ^{4}He collisions. Collisions with ^{4}He at 2 K and 300 K would change Yb atoms from stationary state to 4 m/s and 50 m/s respectively. 300 K helium atoms would still kick Yb atoms out of the MOT, whose capture velocity is ∼30 m/s. The later MOT for ^{6}Li atoms in Ch. 7 showed that even very light species in a MOT are compatible with the buffer-gas beam source.

One of the powerful properties of buffer-gas beam source is its generality. When multiple targets are placed in the cell, one can generate slow buffer-gas beams of different species by just moving the focus of the YAG laser. This is a big difference from the typical oven source + Zeeman slower setup, where one cannot change species easily. We can even shoot multiple targets at the same time and generate their beams simultaneously. Thanks to this

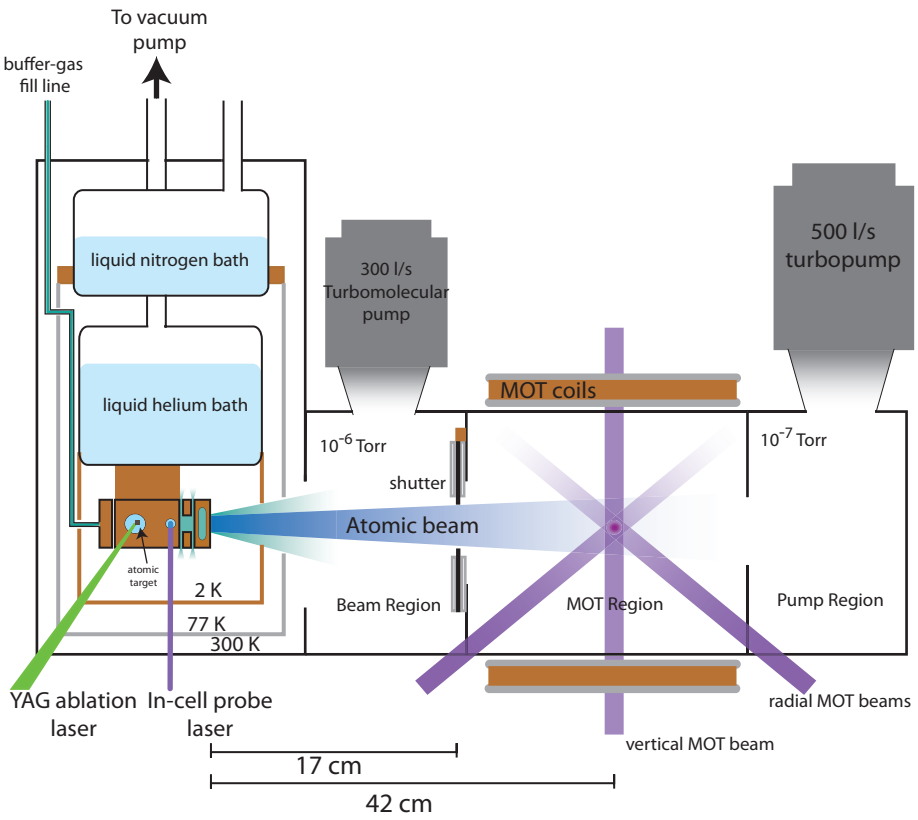

Figure 4.2.1: 1st generation of experimental setup

generality of our source and the tunability of our Ti:sapph laser, we made MOTs for Yb, Er, Tm, and Ho atoms in the same experimental setup, which is shown in Fig. 4.2.1. This work is published in New Journal of Physics [37].

4.2.1 Experimental setup

To confirm the compatibility of the buffer-gas beam with a MOT, we built a small vacuum chamber to make atomic MOTs with buffer-gas beam source (Fig. 4.2.1). This is called the first generation set-up. It has two sections - a cryogenic section and a room temperature section. The cell is mounted to a liquid helium pot, which cools down to 2 K by pumping on it. The 4 K radiation shields are also attached to the helium pot. One more set of radiation shields at 77 K is attached to a liquid nitrogen pot. Once we filled the helium pot (1 liter in volume), we could run the experiment about 2 hours at 2 K. The cryogenic region is directly

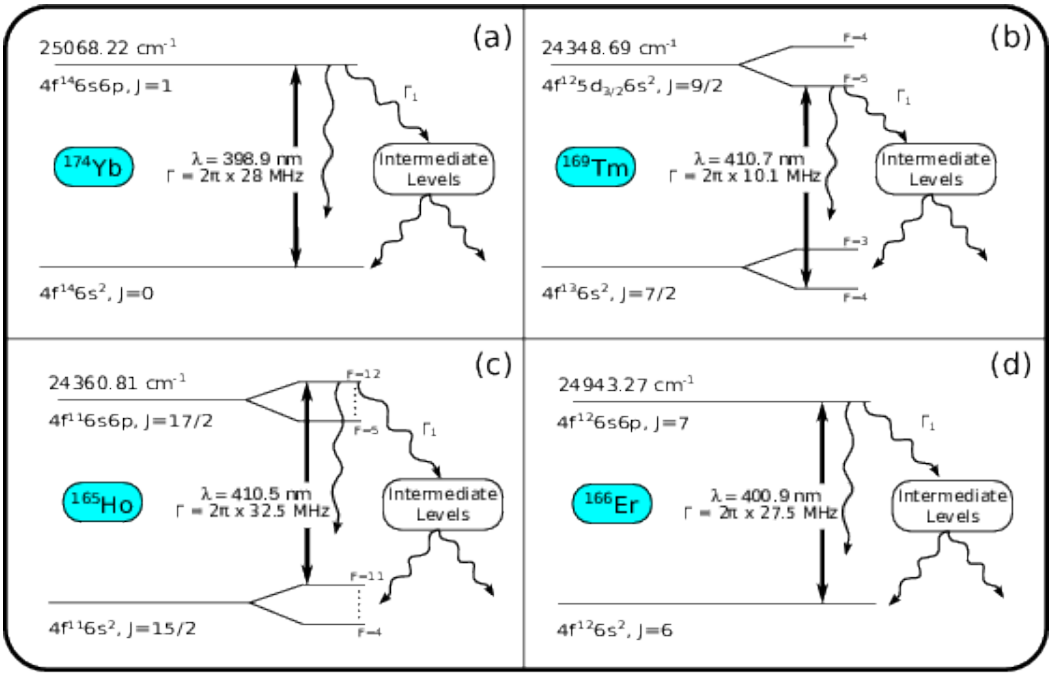

Figure 4.2.2: Schematic energy levels of atoms. The values are from Ref. [87–89]

connected to the room temperature region, which has two big turbo pumps to get rid of the background gas. All chambers are sealed with Viton o-ring seals and the vacuum we get is indicated in Fig. 4.2.1. Two anti-Helmholtz coils are mounted on both sides of the chamber to generate the necessary magnetic field for the MOT. All MOT lasers intersect at the center of the magnetic field. The distance between the two-stage cell last aperture and the MOT center is 40 cm. All the atomic MOTs in Ref. [37] were made in this chamber.

4.2.2 Results

The four atoms' relevant energy levels are depicted in Fig. 4.2.2. All of these lanthanide atoms have intermediate electronic states between the ground state and the excited state that we use for photon-cycling. Despite these intermediate states, people have made MOTs using these blue transitions and those are what we used here as well.

The capture velocity of a MOT is approximately estimated by

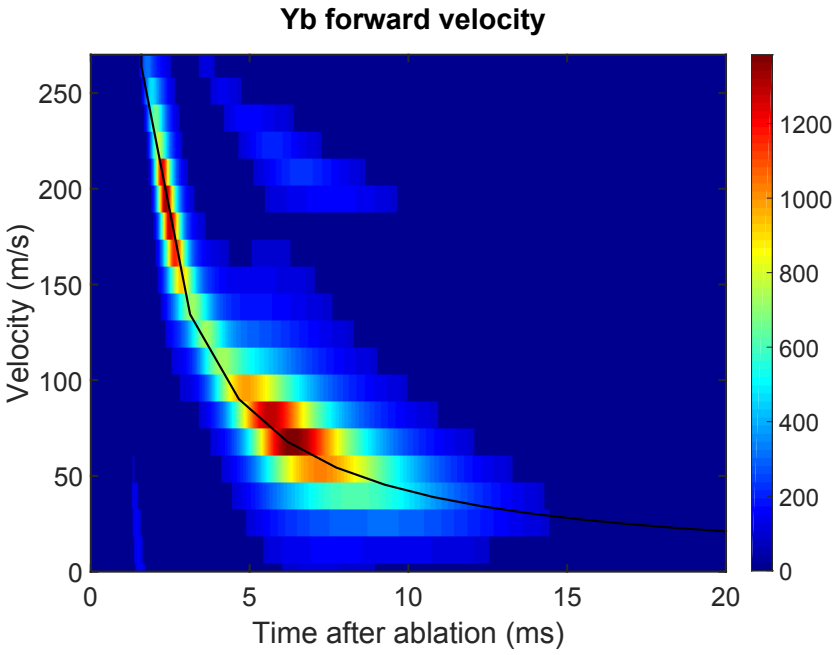

Figure 4.2.3: Forward velocity of ^{174}Yb atoms in 1st generation experimental setup measured 40 cm downstream where the MOT is. Weaker signals above and below the main velocity profile are from other isotopes.

$$v_c = \sqrt{a\, r_c} \tag{4.2.1}$$

[90], where a is acceleration from the laser and r_c is the radius of the laser. For these blue MOTs, the capture velocity is $\lesssim 40$ m/s with reasonable experimental parameters (saturation parameter $s = 1$, $r_c = 0.5$ mm).

The buffer-gas beam of these heavy atoms have peak velocities at about 60 m/s in the 1st generation experimental setup. The measured forward velocity plot of Yb atoms are shown in Fig. 4.2.3. In this slow lanthanide atomic beam, there are atoms slower than the capture velocity of the MOT and they can be captured without further slowing, and we successfully demonstrated MOTs for Yb, Er, Tm, and Ho atoms directly loaded from the slow two-stage buffer-gas beam source without further slowing.

The lifetime of the MOTs are determined by two factors - background gas, which is mostly from the buffer-gas in our case, and the decay to intermediate states. Despite the numerous

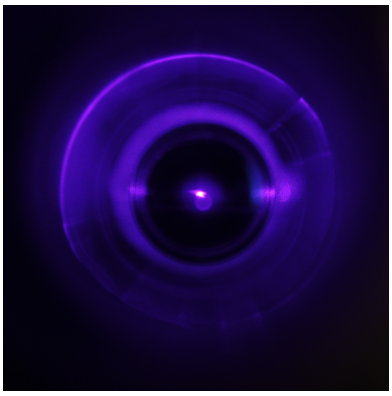

Figure 4.2.4: Photo of ^{174}Yb MOT.

number of intermediate states, one decay constant (Γ_1 in Fig. 4.2.2) which describes the decay rate from the excited state to all intermediate states is enough to describe the time profile of the MOT signals. The buffer-gas atomic beams are pulsed due to the nature of ablation and it makes it easy to observe time decay profile of the MOTs.

The time profile of the MOT can be described by a simple differential equation for the number of atoms inside the trap $n(t)$ [79],

$$\frac{dn}{dt} = R(t) - \alpha\, n(t) - \beta\, n(t)^2 \tag{4.2.2}$$

, where $R(t)$ is the loading rate, α describes the one-body loss due to the background collisions and the decay to the intermediate states, and β describes the two-body loss. In our experiments, no evidence for the two-body effect was observed and this effect is henceforth neglected ($\beta = 0$).

The loading rate $R(t)$ can be approximated with a good agreement to a Gaussian function

$$R(t) = \frac{n_{\mathrm{tot}}}{\sqrt{2}\pi w}\, e^{-\frac{(t-t_0)^2}{2w^2}} \tag{4.2.3}$$

, where the total number of loaded atoms n_{tot} is defined by the normalization

$$\int_{-\infty}^{\infty} dt\, R(t) = n_{\mathrm{tot}} \tag{4.2.4}$$

, t_0 is the pulse arrival time into the MOT region, and w the pulse width.

The one body decay coefficient α can be expressed as a sum of two decay rates - the loss rate due to collisions with the background gas (Γ_0) and the decay rate from the excited state into the intermediate metastable states (Γ_1).

$$\alpha(\Delta) = \Gamma_0 + \Gamma_1 \left(\frac{s_{0,eff}/2}{1 + s_{0,eff} + 4\Delta^2/\Gamma^2} \right) \tag{4.2.5}$$

$s_{0,eff} = \kappa \cdot s_0$ is the effective saturation parameter, Γ is the natural linewidth of the transition, and Δ is the detuning of the laser from the resonance. The decay to the intermediate states depends on the population in the excited state, which is determined by the saturation parameter and the detuning. The effective saturation parameter takes average over Zeeman substates and random light polarization in the MOT region into account, where $\kappa \sim 3 \cdot \frac{2F+1}{2F+3}$ and F corresponds to the hyperfine quantum number of the ground state.

By integrating Eq. 4.2.2, one can derive the number of atoms as a function of time.

$$n(t) = \frac{1}{2}\, n_{\text{tot}}\, e^{\frac{1}{2}\alpha\left(-2(t-t_0)+\alpha w^2\right)} \left(\text{erf}\left(\frac{t_0 + \alpha w^2}{\sqrt{2}w} \right) - \text{erf}\left(\frac{-t + t_0 + \alpha w^2}{\sqrt{2}w} \right) \right) \tag{4.2.6}$$

The error function is defined as $\text{erf}(x) = \frac{2}{\sqrt{\pi}} \int_0^x dt\, e^{-t^2}$.

In this model, we are not considering atoms that come from the intermediate states back to the ground states. The lifetime of the intermediate states are long or comparable compared to our experimental run time scale so that we could safely omit this process.

Fig. 4.2.5 shows typical timetraces of number of atoms in the MOT for each atomic species. The timetraces are fitted using Eq. 4.2.6 (red line in the figure) with excellent agreement. The difference in the lifetimes of different atomic MOTs comes from the different decay rate to the intermediate states for each atoms. The total number of trapped atoms also varies among species due to the different ablation yield and the lifetime. Yb has the longest lifetime of about 100 ms and the most number of trapped atoms $N \sim 10^6$.

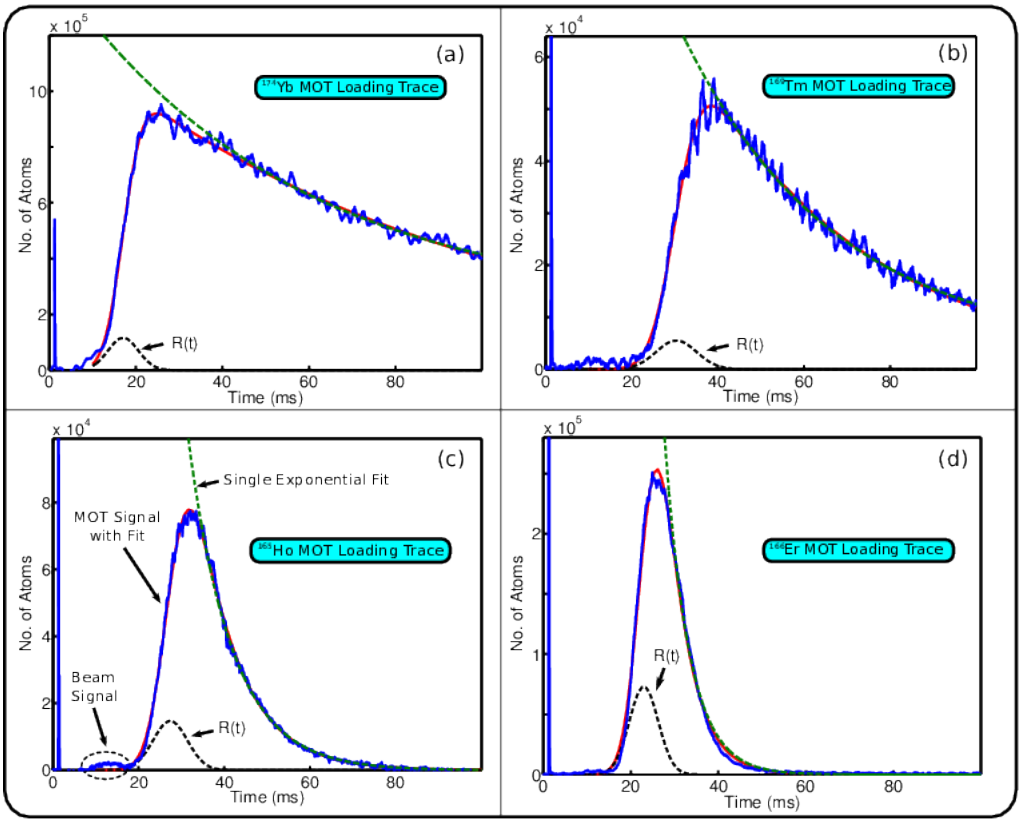

Figure 4.2.5: Timetraces of MOTs for Yb, Tm, Ho, and Er atoms. Blue lines are the experimental data and the red and green lines are fitted lines using Eq. 4.2.6 and a simple exponential function respectively. The loading rate $R(t)$ from the fit is shown as black dotted lines. $t = 0$ ms is when the YAG laser fires.

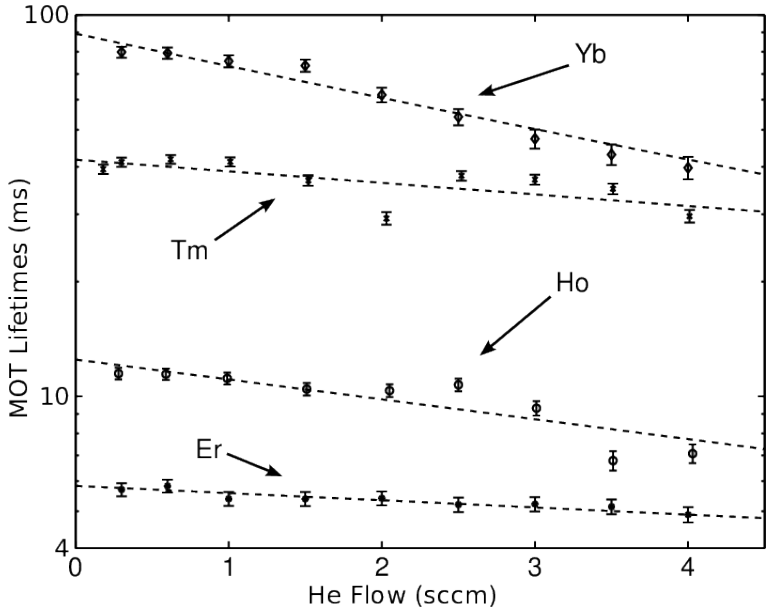

Figure 4.2.6: MOT lifetime ($1/\alpha$) for every species from the fitted timetraces using Eq. 4.2.6. The dashed lines are exponential fits to the data.

From the fitted loading rate $R(t)$, we can roughly estimate the capture velocity of each MOT. For ^{174}Yb, the $R(t)$ starts at ~ 10 ms, which corresponds to the arrival time of 40 m/s. For Tm and Ho, the loading starts at around 20 ms, which means the capture velocity is around 20 m/s. We don't have many atoms around that velocity regime and this could be one of the reasons that we have less number of atoms in the MOTs for Tm and Ho.

To extract Γ_0 and $\Gamma_1$values from the fitted value of α, measurements with different He flow has been performed which only changes the decay rate Γ_0. From the fit in Fig. 4.2.6, the background gas collisional decay rate Γ_0 is extracted.

To get the accurate value of the decay rate to the intermediate states Γ_1, timetraces with different laser detuning Δ is also needed. Fig. 4.2.7 shows the corresponding data we collected for that.

All the parameters and fitted numbers are summarized in Table 4.1. Thanks to the high flux of the buffer-gas beam source, we have also achieved unprecedentedly high loading rate of 2.0 (1.0) $\times 10^{10}$ atoms s^{-1} for ^{174}Yb atoms with a single frequency slowing laser. This lead to the highest number of atoms in the blue MOT for Yb of 1.3 (0.7) $\times 10^{8}$ atoms with

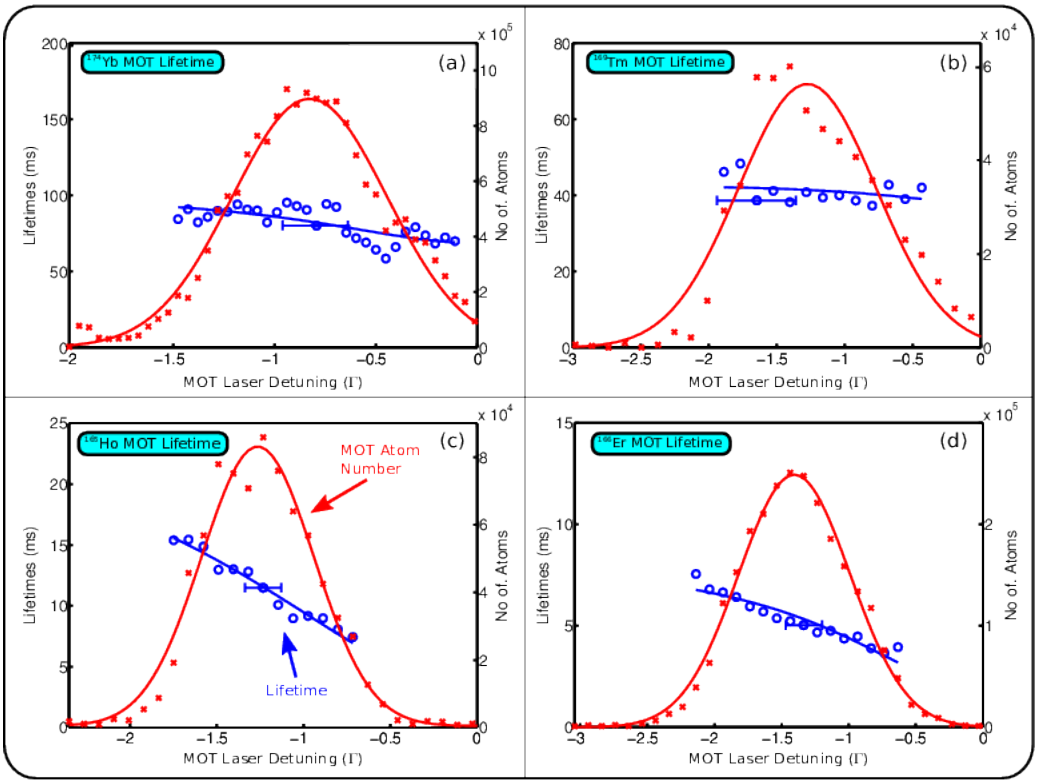

Figure 4.2.7: MOT lifetimes ($1/\alpha$, blue circles) and the number of atoms (red crosses) in the MOTs as functions of the laser detuning with the He flow of 0.3 sccm. Negative values in detuning are red-detuned with respect to the resonance. The blue solid line is a fit to Eq. 4.2.5. Also shown as the red lines are the Gaussian fits to the number of atoms as a guide to the eyes.

	^{174}Yb	^{169}Tm	^{165}Ho	^{166}Er
$\Gamma_0(\mathrm{s}^{-1})$	10 (2)	20 (2)	38 (7)	113 (16)
$\Gamma_1(\mathrm{s}^{-1})$	9 $\binom{+15}{-9}$	12 $\binom{+42}{-12}$	1510 (203)	2071 (753)
$1/\alpha$ (ms)	80 (4)	41 (2)	13 $\binom{+18}{-13}$	5.7 (0.4)
$s_{0,eff}$	1.65	1.60	0.40	0.47
$N_{\max}$	9.2 (4.4) $\times 10^5$	5.0 (2.7) $\times 10^4$	7.7 (3.1) $\times 10^4$	2.5 (1.6) $\times 10^5$

Table 4.1: Parameters and fitted numbers of the atomic MOTs. The data are taken with the experimental conditions of 0.3 sccm He flow rate, 1.1 Hz YAG repetition rate. Both decay rates Γ_0 and Γ_1 are determined via extrapolation to zero He flow rate.

a single frequency slowing laser.

This success with the atomic MOTs directly loaded from the buffer-gas beam source encouraged us to pursue making a MOT for CaF molecules from the buffer-gas beam source with improved setup (generation 2).

Chapter 5

Spectroscopy of CaF Molecules

5.1 Forming a quasi-closed cycling transition

The first step towards laser cooling of molecules is forming a quasi-closed cycling transition to scatter enough number of photons to affect the translational temperature of the molecules. This requires closing of 1. hyperfine and spin-rotational structure, 2. the 1st vibrationally excited state, and 3. the 2nd vibrationally excited state. By observing molecular population transferred to each state, number of photons about 1. a few, 2. 50, and 3. 1000 are guaranteed to be scattered by the molecules. When one counter-propagating photon is scattered by a molecule, the photon decelerates the molecule by 1 cm/s. Therefore, molecules with forward velocity of 50 m/s needs to scatter only 5000 photons to be stopped. This would be easily achieved when we close the leakage to the $v = 2$ state, which would allow the molecule scatter about 10^5 photons. In this chapter, forming this quasi-closed photon cycling is describe accordingly.

In Fig. 5.1.1, fluorescence of CaF molecules excited by single frequency laser that is resonant to the $X\,^2\Sigma$ to $A\,^2\Pi_{1/2}$ transition from each hyperfine states in the ground state is shown in dotted lines. When a laser with four frequencies imprinted by AOMs for all hyperfine states interacts with the molecules, the fluorescence signal became about 10 times

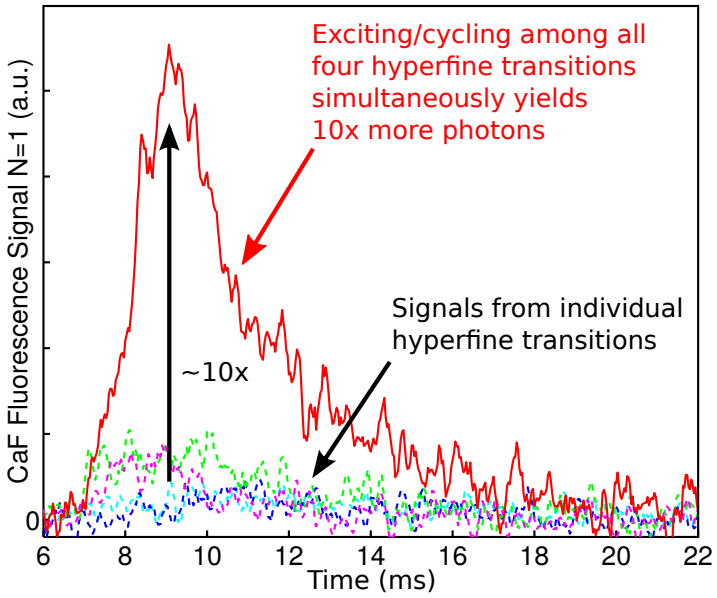

Figure 5.1.1: Closing hyperfine and spin-rotational structure of CaF. The laser intersects with the molecules transversely.

bigger than the sum of the individual fluorescence signals from the molecules, indicating that we succeeded to close the hyperfine and spin-rotation splittings of the molecules and to cycle more than 10 photons per molecule.

The next leakage channel we need to take care is the decay to the first vibrationally excited state, $X\,^2\Sigma(v=1)$. After the molecules scatter about 50 photons, they decay to this state and are lost from the photon cycle. By putting the 1st repump laser which pumps the molecules back to the $X\,^2\Sigma(v=0)$ through the $A\,^2\Pi_{1/2}(v=0)$ state at 628 nm with four hyperfine splittings, the fluorescence at 606 nm (the main) increased by about factor of 4 (Fig. 5.1.2). This tells us that about $50\times4 = 200$ photons are scattered by the molecules which is determined by the size of the laser beam (diameter of 1 cm) that limits the interaction time between the molecules and the photons.

The molecules with forward velocity of 50 m/s interact with the 1 cm laser beam during 0.2 ms, and we roughly estimate the scattering rate to be about 200/0.2 ms $= 1 * 10^6$ $s^{-1} = 2\pi \times 0.16$ MHz. The laser power was 20 mW per hyperfine state which corresponds

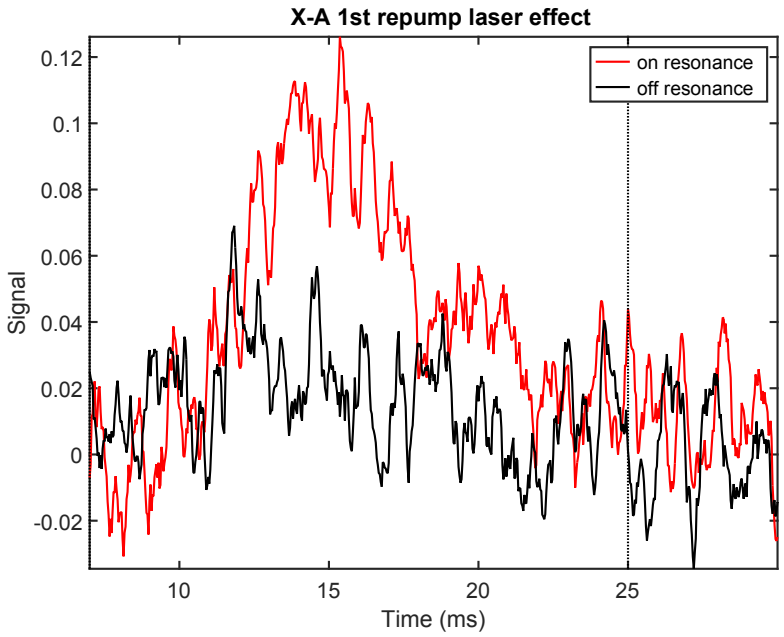

Figure 5.1.2: Closing the leakage to the $X\,^2\Sigma(v=1)$ state of CaF through the $A\,^2\Pi_{1/2}(v=0)$ state. The lasers intersected with the molecules at 45 degrees near the MOT center, which is 50 cm away from the cell. The molecules with 50 m/s were monitored. The YAG fired at 5 ms.

to the saturation parameter of about 1.5. The expected scattering rate with 1.5 saturation parameter is about $2\pi \times 0.7$ MHz which is a few times bigger than what we observed. It is plausible since we didn't actively remix the dark magnetic substates here and the scattering rate could be reduced due to the remixing time scale determined by the Earth field or any stray field. This limit could be overcome by switching the polarization of the detection lasers that is demonstrated in Fig. 5.1.3. The total signal increased by a factor of 2.5 by polarization switching, resulting the scattering rate of $2\pi \times 0.4$ MHz, which is closer to the estimation.

We also confirmed repumping the $X\,^2\Sigma(v=1)$ states back to the $X\,^2\Sigma(v=0)$ state using the $X\,^2\Sigma(v=1) - B\,^2\Sigma(v=0)$ transition at 548 nm (Fig. 5.1.4). Here, the lasers counter-propagated to the molecular beam and the fluorescence signals were detected at 50 cm downstream (MOT center). When the $X - B$ 1st repump laser was off-resonant, all molecules were pumped into the $X\,^2\Sigma(v=1)$ state before reaching the MOT center and

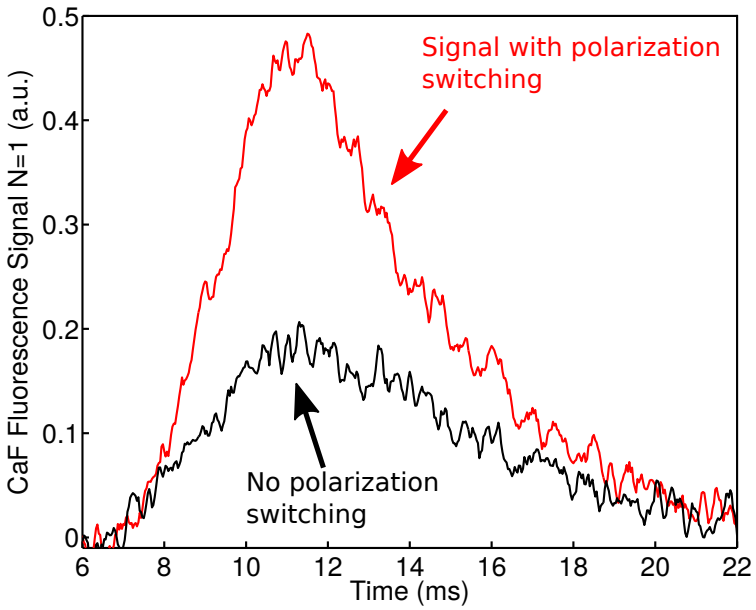

Figure 5.1.3: Increase of the fluorescence signal by the laser polarization switching to actively remix the dark magnetic substate.

no fluorescence was detected (black line in Fig. 5.1.4). With the $X - B$ 1st repump laser on-resonance, 606 nm fluorescence from the molecules were detected (red line in Fig. 5.1.4), showing the molecules were pumped back to the $X\,^2\Sigma(v = 0)$ state.

The final leakage channel to check is the decay to the $X\,^2\Sigma(v = 2)$ state, which requires scattering of about 1000 photons. By watching the fluorescence from lasers with hyperfine sidebands counter-propagating to the molecular beam, we confirmed that the 2nd repump laser from the $X\,^2\Sigma(v = 2)$ state to $A\,^2\Pi_{1/2}(v = 1)$ state increased the main laser fluorescence by factor of 5. This indicates that the molecules scattered about 5000 photons, which is enough to see velocity change by 50 m/s.

5.2 Two-photon transition spectroscopy of CaF molecules

The transition frequencies between the X states and the A and B states have been well studied in the previous literatures, which are summarized in Sec. 2.2.1. However, the necessary transitions between the A states and C or D states for the background-free two-

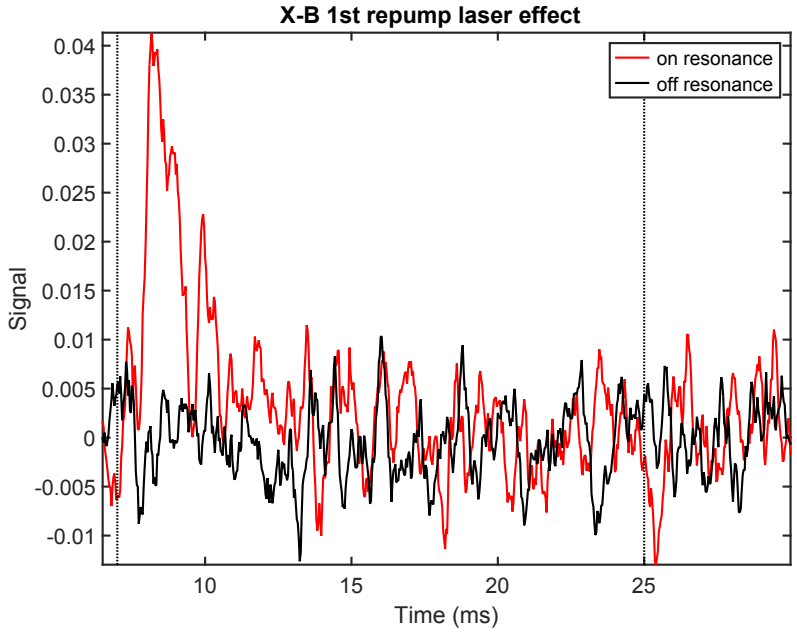

Figure 5.1.4: Closing the leakage to the $X\,^2\Sigma(v=1)$ state of CaF through the $B\,^2\Sigma(v=0)$ state. The lasers counter-propagated to the molecules. The fluorescence from the molecules were detected at 50 cm from the cell. The YAG fired at 5 ms.

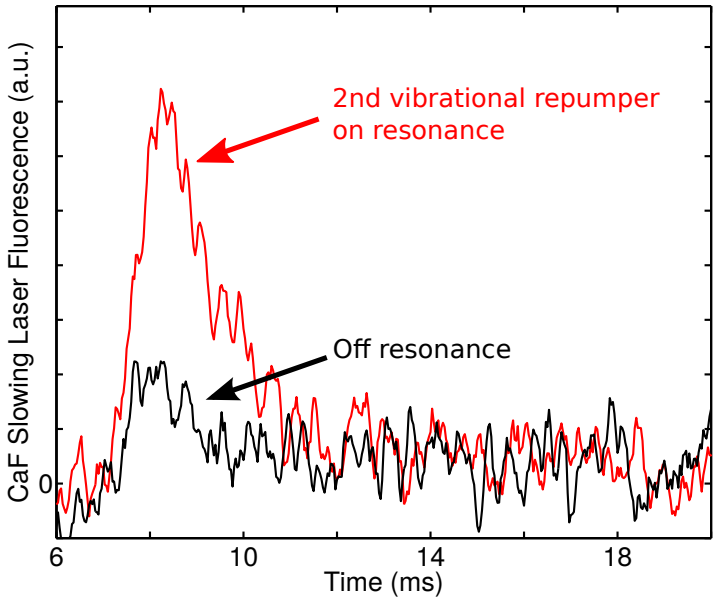

Figure 5.1.5: Closing the leakage to the $X\,^2\Sigma(v=2)$ state of CaF. The lasers counter-propagated to the molecules. The fluorescence from the molecules were detected at 50 cm from the cell. The YAG fired at 5 ms.

photon detection have been measured with precision only of a GHz [74], which is not enough for our purpose. We took full advantage of the tunable Ti:sapph laser and found the necessary lines with the precision of about a few MHz.

To find the transitions, we first excited molecules with 606 nm transition from the ground state $X\,^2\Sigma(N = 1)$ to the intermediate excited state $A\,^2\Pi_{1/2}(J = 1/2, +)$. When the Ti:sapph laser was on the resonance of the $A - C$ or $A - D$ lines, molecules in the A states are pumped to the C or D states. We use ~ 200 mW of the $A - C$, D laser so that the molecules could be excited to higher states within the short lifetime of the A states. We detected 331 nm photons emitted from the molecules decaying from the C or D states back to the ground state X. All the lasers intersected perpendicular to the molecular beam to minimize the Doppler effect. The molecules were optically pumped to the higher vibrational states in the $X\,^2\Sigma(v = 1,\, 2)$ states using the $X\,^2\Sigma(v = 0) - A\,^2\Pi_{1/2}(v = 1)$ and the $X\,^2\Sigma(v = 1) - A\,^2\Pi_{1/2}(v = 2)$ transitions to find the transitions from the $A\,^2\Pi_{1/2}(v = 1,\, 2)$ states to the $C\,^2\Pi_{1/2}(v = 1,\, 2)$ or $D\,^2\Sigma(v = 1,\, 2)$ states (Fig. 5.2.1).

5.2.1 Results

Here, all the $A\,^2\Pi_{1/2} - C\,^2\Pi_{1/2}$ and the $A\,^2\Pi_{1/2} - D\,^2\Sigma$ transitions we found are summarized. The discussion about the splittings in the transitions will be given in the next subsection. Summary of all the transitions are in Fig. 5.2.2.

5.2.1.1 The $A\,^2\Pi_{1/2} - C\,^2\Pi_{1/2}$ transitions

$A\,^2\Pi_{1/2}(v = 0)$ to $C\,^2\Pi_{1/2}(v = 0)$ transitions

- $A\,^2\Pi_{1/2}(v = 0,\, J = 1/2, +)$ to $C\,^2\Pi_{1/2}(v = 0,\, J = 1/2, -)$: $X\,^2\Sigma(v = 0,\, N = 1)$ to $A\,^2\Pi_{1/2}(v = 0,\, J = 1/2, +)$ laser at 494.431940 THz with 4 hyperfine lines
  - 95 % interval of the resonances from the Lorentzian fit : 10.6469 MHz for the first peak and 3.8323 MHz for the second peak

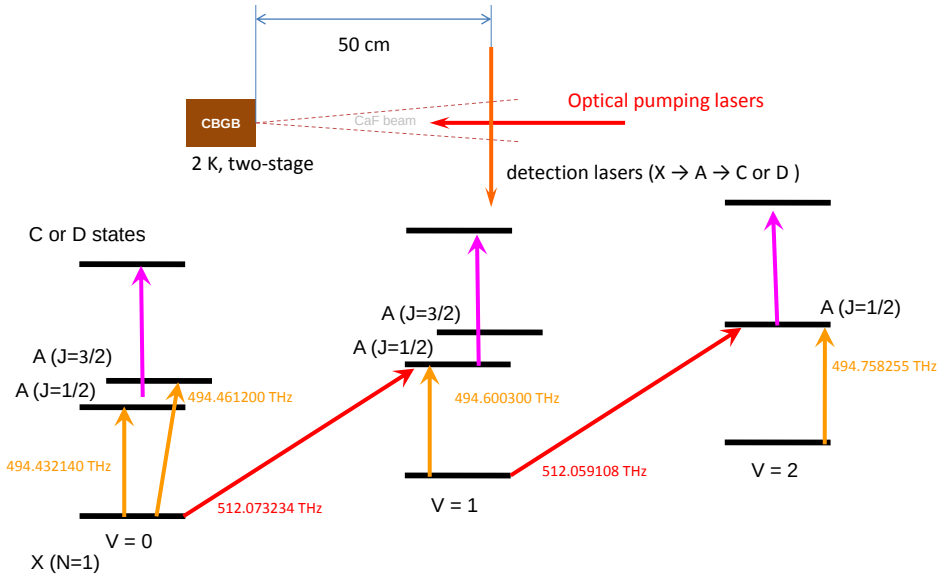

Figure 5.2.1: Schematic overview of the setup for the $A - C,\, D$ transition spectroscopy. CBGB stands for "cryogenic buffer-gas beam".

  - Splitting of the two peaks : 378.22 MHz

- $A\,^2\Pi_{1/2}(v = 0,\, J = 1/2,\, +)$ to $C\,^2\Pi_{1/2}(v = 0,\, J = 3/2,\, -)$: $X\,^2\Sigma(v = 0,\, N = 1)$ to $A\,^2\Pi_{1/2}(v = 0,\, J = 1/2,\, +)$ laser at 494.431940 THz with 4 hyperfine lines

  - 95 % interval of the resonances from the Lorentzian fit : 5.0998 MHz for the first peak and 7.7603 MHz for the second peak

  - Splitting of the two peaks: 95.0961 MHz

- $A\,^2\Pi_{1/2}(v = 0,\, J = 3/2,\, +)$ to $C\,^2\Pi_{1/2}(v = 0,\, J = 1/2,\, -)$ for detection of laser slowing : $X\,^2\Sigma(v = 1,\, N = 1)$ to $A\,^2\Pi_{1/2}(v = 1,\, J = 3/2,\, +)$ laser at 494.460948 THz with 4 hyperfine lines

  - transition for laser slowing detection

  - 95 % interval of the resonances from the Lorentzian fit : 4 MHz for the peak

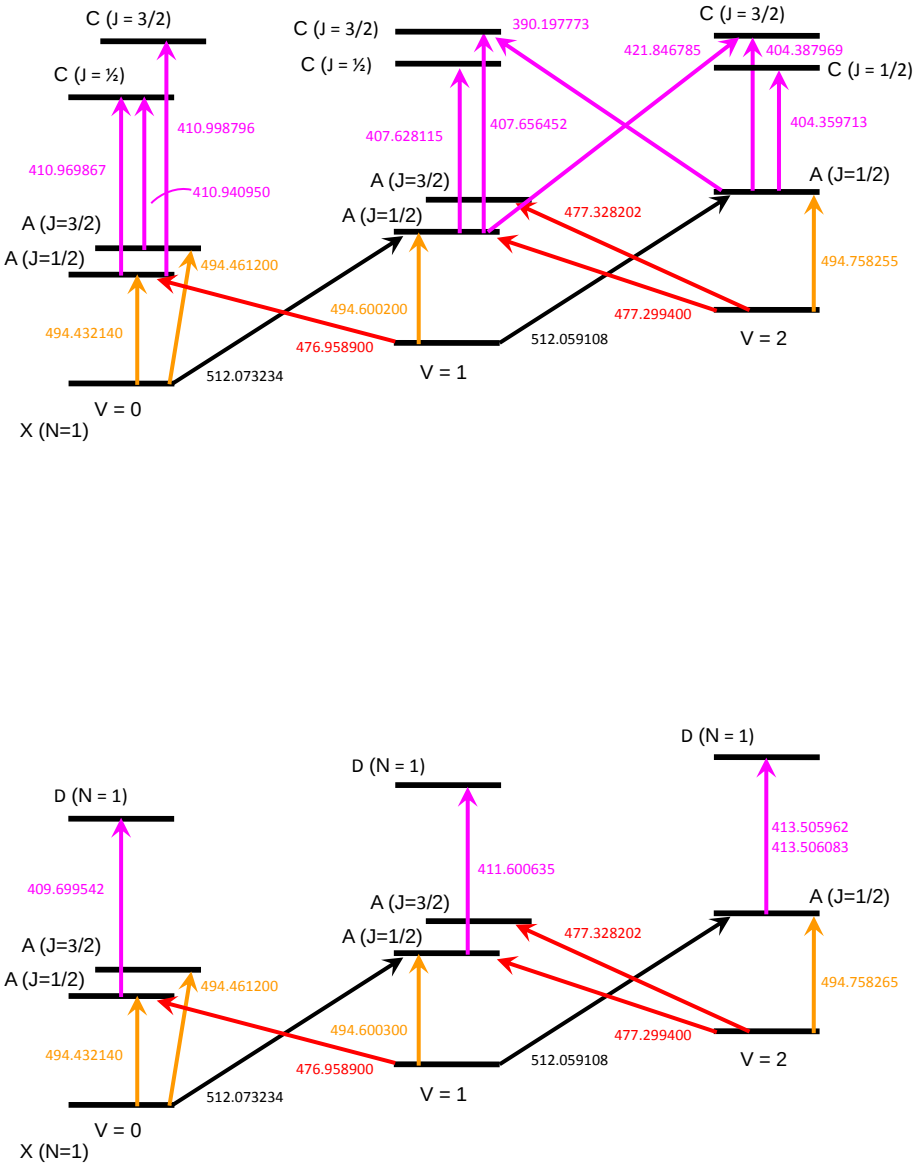

Figure 5.2.2: Summary of the $A - C$, D transitions.

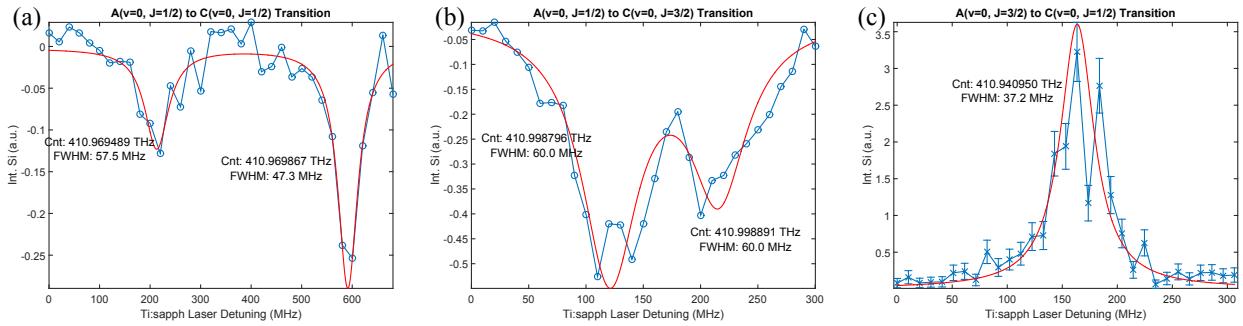

Figure 5.2.3: (a) $A\,^2\Pi_{1/2}(v=0,\, J=1/2,\, +)$ to $C\,^2\Pi_{1/2}(v=0,\, J=1/2,\, -)$ resonances. (b) $A\,^2\Pi_{1/2}(v=0,\, J=1/2,\, +)$ to $C\,^2\Pi_{1/2}(v=0,\, J=3/2,\, -)$ resonances. (c) $A\,^2\Pi_{1/2}(v=0,\, J=3/2,\, +)$ to $C\,^2\Pi_{1/2}(v=0,\, J=1/2,\, -)$ resonance. (a) and (b) were taken on 2014/05/07 using analog mode of the UV PMT (R7600P) in stem region, which is 50 cm downstream from the cell. (c) was taken on 2015/04/09 using photon counting mode of the same PMT, also at 50 cm downstream.

$A\,^2\Pi_{1/2}(v=1)$ to $C\,^2\Pi_{1/2}(v=1)$ transitions

- $A\,^2\Pi_{1/2}(v=1,\, J=1/2,\, +)$ to $C\,^2\Pi_{1/2}(v=1,\, J=1/2,\, -)$: $X\,^2\Sigma(v=1,\, N=1)$ to $A\,^2\Pi_{1/2}(v=1,\, J=1/2,\, +)$ laser at 494.600300 THz with 4 hyperfine lines
  - 95 % interval of the resonances from the Lorentzian fit: 3.9502 MHz for the first peak and 1.7947 MHz for the second peak
  - Splitting of the two peaks: 358.7746 MHz
- $A\,^2\Pi_{1/2}(v=1,\, J=1/2,\, +)$ to $C\,^2\Pi_{1/2}(v=1,\, J=3/2,\, -)$: $X\,^2\Sigma(v=1,\, N=1)$ to $A\,^2\Pi_{1/2}(v=1,\, J=1/2,\, +)$ laser at 494.600285 THz with 4 hyperfine lines
  - 95 % interval of the resonances from the Lorentzian fit: 0.0014 MHz for the peak
  - The scan was not wide enough to see another transition next to it.

$A\,^2\Pi_{1/2}(v=2)$ to $C\,^2\Pi_{1/2}(v=2)$ transitions

- $A\,^2\Pi_{1/2}(v=2,\, J=1/2,\, +)$ to $C\,^2\Pi_{1/2}(v=2,\, J=1/2,\, -)$: $X\,^2\Sigma(v=2,\, N=1)$ to $A\,^2\Pi_{1/2}(v=2,\, J=1/2,\, +)$ laser at 494.758265 THz with 4 hyperfine lines

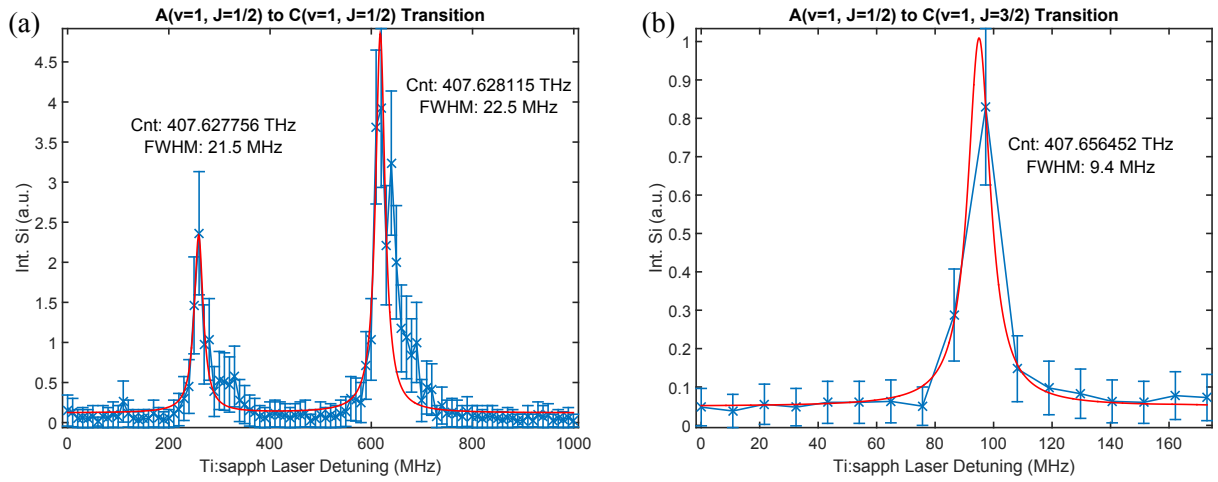

Figure 5.2.4: (a) $A\,^2\Pi_{1/2}(v=1,\ J=1/2,\ +)$ to $C\,^2\Pi_{1/2}(v=1,\ J=1/2,\ -)$ resonances from data taken on 2015/06/23. (b) $A\,^2\Pi_{1/2}(v=1,\ J=1/2,\ +)$ to $C\,^2\Pi_{1/2}(v=1,\ J=3/2,\ -)$ resonance from data taken on 2015/06/03. The 331 nm fluorescence from the molecules were detected by a UV PMT with photon counting mode at 50 cm downstream.

  - 95 % interval of the resonances from the Lorentzian fit: 1.7836 MHz for the first peak and 0.8351 MHz for the second peak
  - Splitting of the two peaks: 359.2872 MHz

- $A\,^2\Pi_{1/2}(v=2,\ J=1/2,\ +)$ to $C\,^2\Pi_{1/2}(v=2,\ J=3/2,\ -)$: $X\,^2\Sigma(v=2,\ N=1)$ to $A\,^2\Pi_{1/2}(v=2,\ J=1/2,\ +)$ laser at 494.758265 THz with 4 hyperfine lines
  - 95 % interval of the resonances from the Lorentzian fit: 0.7159 MHz for the first peak and 2.3052 MHz for the second peak
  - Splitting of the two peaks: 91.1639 MHz

$A\,^2\Pi_{1/2}$ to $C\,^2\Pi_{1/2}$ off-diagonal transitions

- $A\,^2\Pi_{1/2}(v=1,\ J=1/2,\ +)$ to $C\,^2\Pi_{1/2}(v=2,\ J=3/2,\ -)$: $X\,^2\Sigma(v=1,\ N=1)$ to $A\,^2\Pi_{1/2}(v=1,\ J=1/2,\ +)$ laser at 494.600300 THz with 4 hyperfine lines
  - 95 % interval of the resonances from the Lorentzian fit : 2.6712 MHz for the first peak and 4.2096 MHz for the second peak

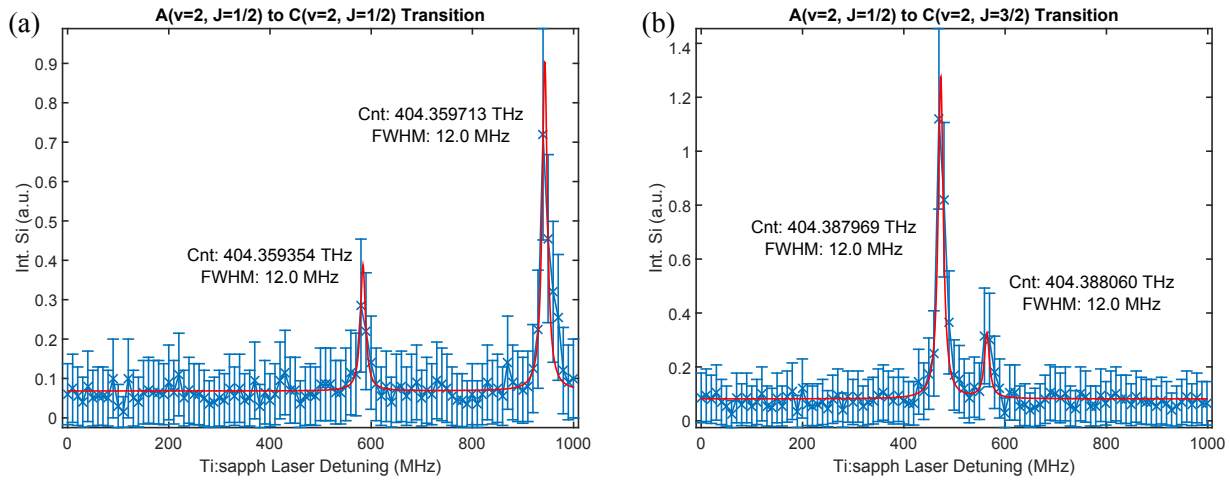

Figure 5.2.5: (a) $A\,^2\Pi_{1/2}(v = 2,\ J = 1/2,\ +)$ to $C\,^2\Pi_{1/2}(v = 2,\ J = 1/2,\ -)$ resonances from data taken on 2015/06/23 (b) $A\,^2\Pi_{1/2}(v = 2,\ J = 1/2)$ to $C\,^2\Pi_{1/2}(v = 2,\ J = 3/2)$ resonances from data taken on 2015/06/23. The 331 nm fluorescence from the molecules were detected by a UV PMT with photon counting mode at 50 cm downstream.

  - Splitting of the two peaks: 88.1259 MHz

- $A\,^2\Pi_{1/2}(v = 2,\ J = 1/2,\ +)$ to $C\,^2\Pi_{1/2}(v = 1,\ J = 3/2,\ -)$: $X\,^2\Sigma(v = 2,\ N = 1)$ to $A\,^2\Pi_{1/2}(v = 2,\ J = 1/2,\ +)$ laser at 494.758255 THz with 4 hyperfine lines

  - 95 % interval of the resonances from the Lorentzian fit : 2.4224 MHz for the first peak and 2.3758 MHz for the second peak
  - Splitting of the two peaks: 11.8104 MHz
  - The scan was not wide enough to see nearby transition

5.2.1.2 The $A\,^2\Pi_{1/2} - D\,^2\Sigma$ transitions

- $A\,^2\Pi_{1/2}(v = 0,\ J = 1/2,\ +)$ to $D\,^2\Sigma(v = 0,\ N = 1)$: $X\,^2\Sigma(v = 0,\ N = 1)$ to $A\,^2\Pi_{1/2}(v = 0,\ J = 1/2,\ +)$ laser at 494.432140 THz with 4 hyperfine lines

  - 95 % interval of the resonances from the Lorentzian fit: 0.0043 MHz for the peak
  - The scan was not wide enough to see nearby transition.

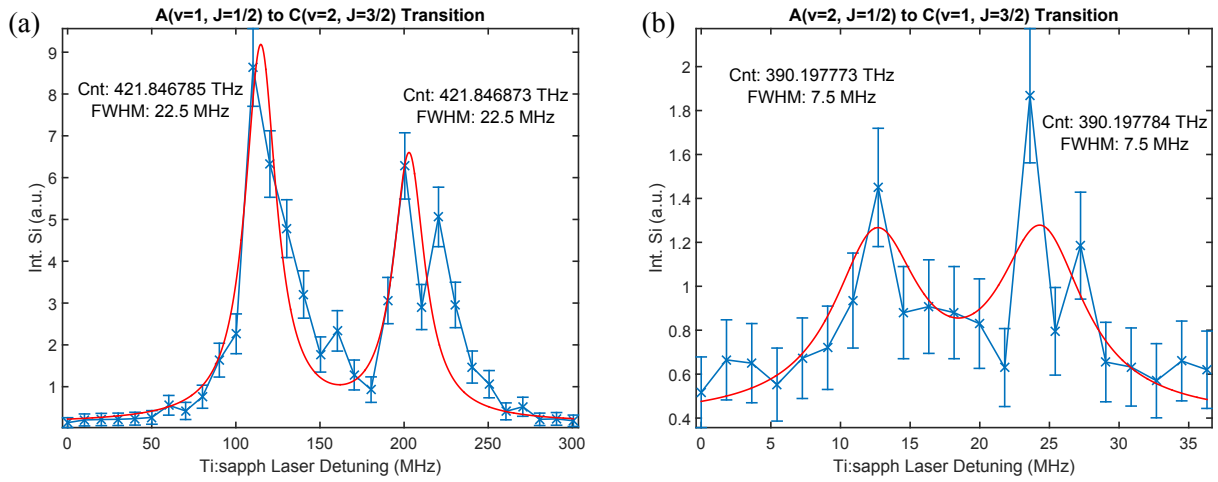

Figure 5.2.6: $A\,^2\Pi_{1/2}(v = 1,\ J = 1/2,\ +)$ to $C\,^2\Pi_{1/2}(v = 2,\ J = 3/2,\ -)$ resonances from data 20150622/1821.13.$A\,^2\Pi_{1/2}(v = 2,\ J = 1/2,\ +)$ to $C\,^2\Pi_{1/2}(v = 1,\ J = 3/2,\ -)$ resonances from data 20150623/1316_39. The 331 nm fluorescence from the molecules were detected by a UV PMT with photon counting mode at 50 cm downstream.

- $A\,^2\Pi_{1/2}(v = 1,\ J = 1/2,\ +)$ to $D\,^2\Sigma(v = 1,\ N = 1)$: $X\,^2\Sigma(v = 1,\ N = 1)$ to $A\,^2\Pi_{1/2}(v = 1,\ J = 1/2,\ +)$ laser at 494.600300 THz with 4 hyperfine lines
  - 95 % interval of the resonances from the Lorentzian fit: 0.0028 MHz for the peak
  - The scan was not wide enough to see nearby transition.
- $A\,^2\Pi_{1/2}(v = 2,\ J = 1/2,\ +)$ to $D\,^2\Sigma(v = 2,\ N = 1)$: $X\,^2\Sigma(v = 2,\ N = 1)$ to $A\,^2\Pi_{1/2}(v = 2,\ J = 1/2,\ +)$ laser at 494.758265 THz with 4 hyperfine lines
  - 95 % interval of the resonances from the Lorentzian fit: 0.8651 MHz for the first peak and 2.5317 MHz for the second peak
  - Splitting of the two peaks : 121.2544 MHz

5.2.2 Discussion

As we can see from the data above, two peaks are found for each transition in the scan where we have enough scan width. The $X - A$ transition laser covers all the spin-rotation

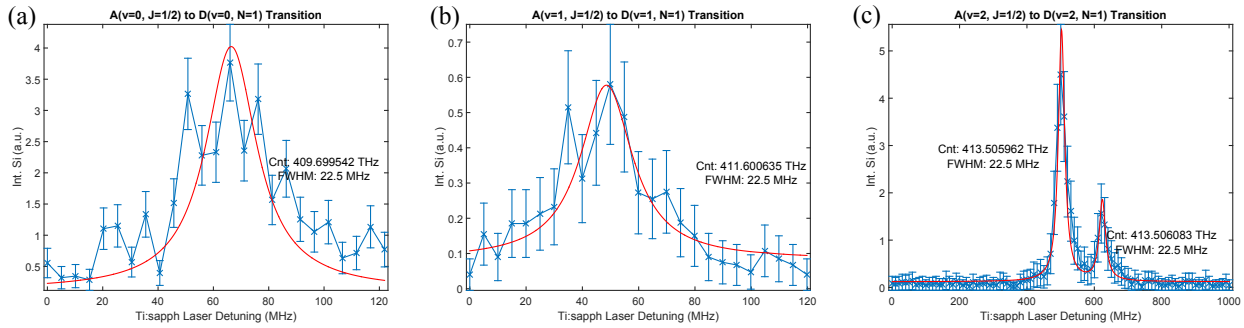

Figure 5.2.7: (a) $A\,^2\Pi_{1/2}(v=0,\, J=1/2,\, +)$ to $D\,^2\Sigma(v=0,\, N=1)$ resonance from data taken on 2015/06/12. (b) $A\,^2\Pi_{1/2}(v=1,\, J=1/2,\, +)$ to $D\,^2\Sigma(v=1,\, N=1)$ resonance from data taken on 2015/06/12. (c) $A\,^2\Pi_{1/2}(v=2,\, J=1/2,\, +)$ to $D\,^2\Sigma(v=2,\, N=1)$ resonances from data taken on 2015/06/23. The 331 nm fluorescence from the molecules were detected by a UV PMT with photon counting mode at 50 cm downstream.

and hyperfine splittings in the $X\,^2\Sigma(N=1)$ states and we don't see these splittings. The $A\,^2\Pi_{1/2}(J=1/2,\, +)$ state hyperfine splitting is measured to be about 5 MHz, smaller than the linewidth of the A states [69]. Therefore, the observed splittings reflect the energy structure of the upper states C or D.

For transitions to the $D\,^2\Sigma(N=1)$ states, it is straight forward to guess that the splittings are from the spin-rotation interaction. In Ref. [74], the spin-rotation coupling constant for the D state has been measured to be -0.00899 cm^{-1} ~ -270 MHz, which would give a splitting of about 405 MHz in the $N=1$ state, which is a lot bigger than the splitting we see. For the $C\,^2\Pi_{1/2}$ states, Λ doubling cannot explain the splittings since we are addressing only $(-)$ parity states in the C states due to the selection rules.

One of the possible explanations is the hyperfine interaction. the $C\,^2\Pi_{1/2}$ have hyperfine structures that the transitions to all the hyperfine states within the J state are allowed ($A\,^2\Pi_{1/2}(J=1/2,\, +,\, F=0,1)$ to $C\,^2\Pi_{1/2}(J=1/2,\, -,\, F=0,1)$). Therefore, it is possible that we have observed the hyperfine structure of the excited C states, although it is unlikely for this highly excited state to have a strong hyperfine interaction unless the Ca^+3d orbital wavefunction, from which the $C\,^2\Pi$ state originates, magically has high probability at the position of fluorine (F) nuclei.

Chapter 6

White-light slowing of ^{6}Li atoms and CaF molecules

In order to load ^{6}Li atoms and CaF molecules from a buffer-gas beam into an AC MOT, they need to be slowed since their velocities out of the two-stage cell are still higher than the capture velocities of the MOT. The results of the white-light slowing of both species are summarized in this chapter.

6.1 Brief description of white-light slowing

In most of atomic experiments, Zeeman slowing is used to slow the atoms down to 0 m/s. A single fixed frequency laser is counter-propagating to atomic beam and Zeeman shift compensates the Doppler shift as the atoms slow down. CaF molecules, on the other hand, have complicated internal structures like spin-rotation coupling and hyperfine coupling which are similar scale to the velocity shift. All different levels with different g factors start being mixed when B field is applied and it is challenging to find a closed cycle with the B field. Alternatively, we use "white-light slowing" where we broaden the slowing laser frequency so that it covers the range of Doppler shifts during the slowing.

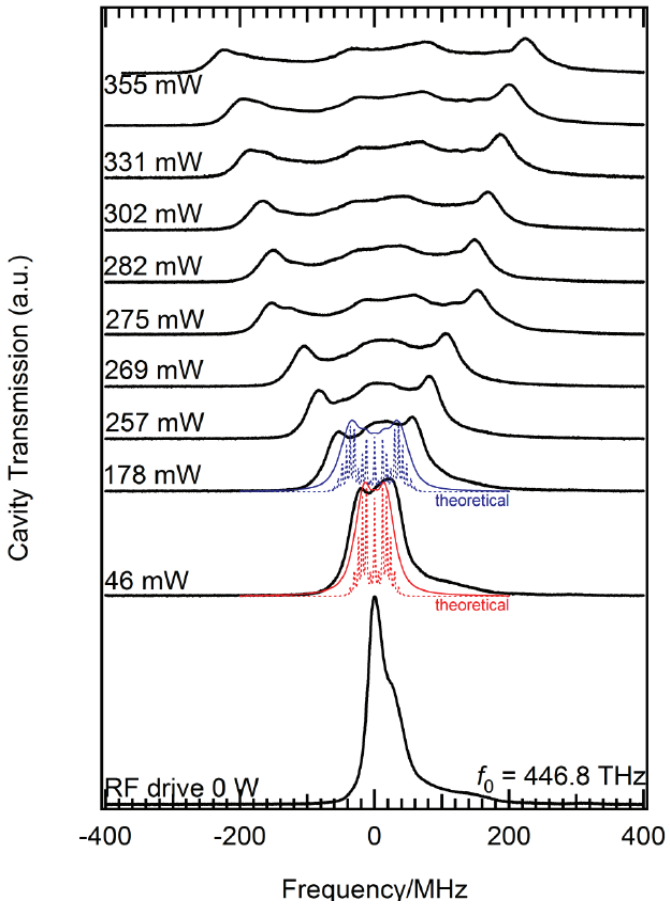

Figure 6.2.1: White-light broadening for ^{6}Li atoms. The limited resolution and asymmetry of the spectrum are results of the poor coupling of the laser to the transverse cavity.

6.2 White-light slowing of ^{6}Li atoms

^{6}Li has a high forward velocity of about 150 m/s out of the two-stage cell due to its light mass (the thermal velocity of ^{6}Li at 4 K is about 105 m/s). This is significantly higher than the capture velocity of the ^{6}Li MOT (about 10 m/s with our magnetic field gradient and the laser beam size). To slow down the atoms below the capture velocity, we applied white-light slowing to the ^{6}Li atoms.

Fig. 6.2.1 shows the broadening of the ^{6}Li slowing laser using the white-light EOM as a

function of the RF power into the EOM. The EOM frequency was tuned to 4.9770 MHz.

The slowing results in Fig. 6.2.2 shows clear effects of the white-light broadening on the velocity change. When the slowing laser was not broadened, only small change in the velocity took place since the slowing laser was not resonant anymore after the atoms got slowed to experience the Doppler shift comparable to the linewidth of the excited state. As we increase the white-light broadening, more and more deceleration takes place and we even saw atoms with negative velocity (= going back to the cell) with the maximum driving power to the EOM.

6.3 White-light slowing of CaF molecules

6.3.1 Laser setup

6.3.1.1 Slowing Laser Broadening

The slowing laser frequency is broadened by two over-driven homemade EOMs. One EOM generates 4.5185 MHz spacing sidebands to cover Doppler shifts (white-light EOM) and the other EOM with 24.841 MHz sidebands to cover the hyperfine structure of CaF ground state (hyperfine EOM). The main and 2 repump lasers are combined and go through the same EOMs with same polarization.

The Fig. 6.3.1 shows the frequency spectrum of broadened main slowing laser measured by a beat-note measurement. The saturation parameter is calculated using the saturation intensity of the $X\,^2\Sigma(v=0,\,N=1)$ to $A\,^2\Pi_{1/2}(v=0,\,J=1/2,\,+)$ transition and the beam size of 1 cm^2. The overall frequency width is 400 MHz, which is a lot more than what we think we need. There may be more room in tuning the frequency region to optimize the slowing.

Assuming effective scattering rate of $2\pi\times1$ MHz, the calculated deceleration that molecules at certain velocity in each hyperfine state receive from the slowing laser are plotted in Fig.

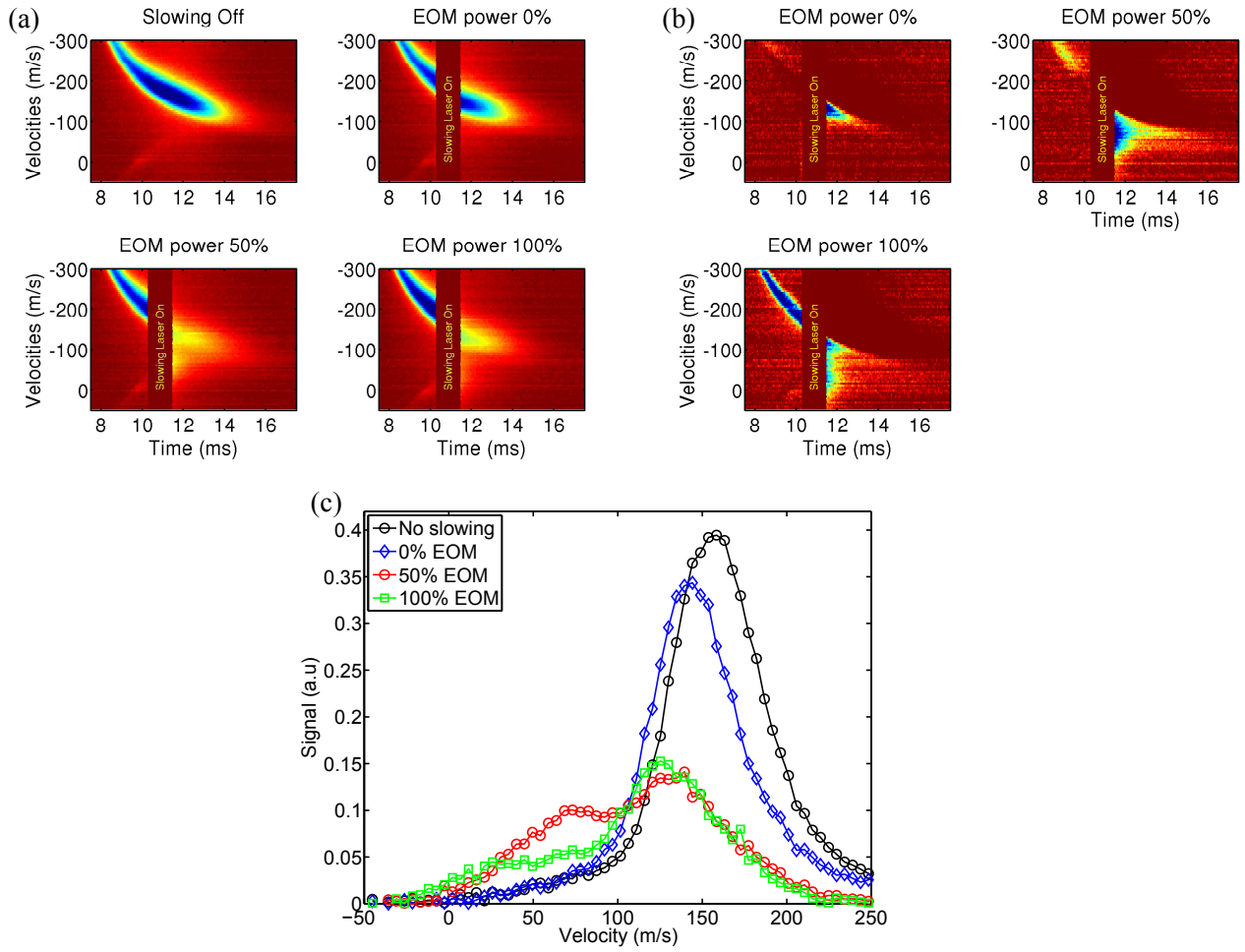

Figure 6.2.2: White-light slowing of ^{6}Li atoms. The YAG laser fires at t =5 ms and the slowing laser is on for t =10.5 - 11.5 ms, which is indicated in the plots. The measurement is done at 1 m downstream from the cell. 100 % EOM power corresponds to the RF power of 355 mW. (a) Beam signal with various slowing laser broadening. The upper left plot shows the beam out of the cell without slowing. (b) Difference the unperturbed beam and the slowed beam. Blue area indicates more atoms with the slowing lasers. The color scale is different from (a). (c) The velocity of ^{6}Li atoms integrated from 11.5 ms to 20 ms.

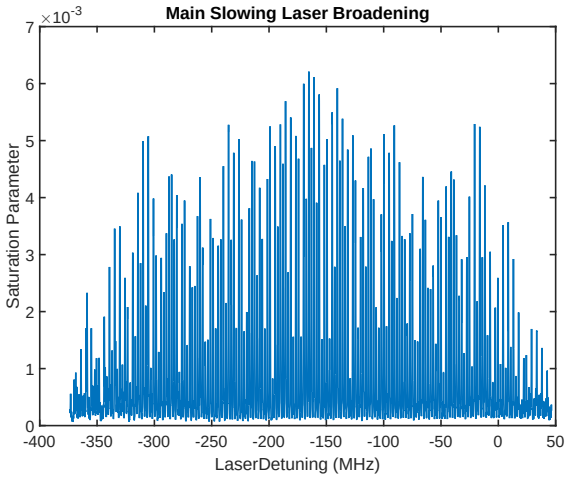

Figure 6.3.1: Main slowing laser broadening from beat note measurement. The main laser intensity into the chamber is 90 mW/cm^2 and the saturation parameter is calculated using the saturation intensity in Ch. 2.2.4. The modulated light by the two EOMs is beat with the unmodulated light shifted by about 220 MHz. 0 MHz in this plot is the resonance of the $X\,^2\Sigma(N=1,\ J=3/2,\ F=2)$ to $A\,^2\Pi_{1/2}(J=1/2,\ +)$ transition.

6.3.2.

The 1st and 2nd repump lasers are also broadened using the same EOMs and their spectra are shown in Fig. 6.3.3.

6.3.2 Optical pumping between vibrational states

To tune the slowing laser parameters in a controlled way, we observed optical pumping between vibrational states using slowing lasers. After successfully pumping a reasonable number of molecules into $X\,^2\Sigma(v=2)$ using the main and the 1st repump lasers, and repumping them back to the cycling transition by the 2nd repump laser, we could detected molecules slowed due to the slowing lasers.

6.3.2.1 Pumping between the $X\,^2\Sigma(v=0)$ state and the $X\,^2\Sigma(v=1)$ state by the main and the 1st repump slowing laser

After scattering about 50 photons from the main slowing laser, most of the molecules are predicted to decay to the $X\,^2\Sigma(v=1)$ state from the Franck-Condon factors. This process

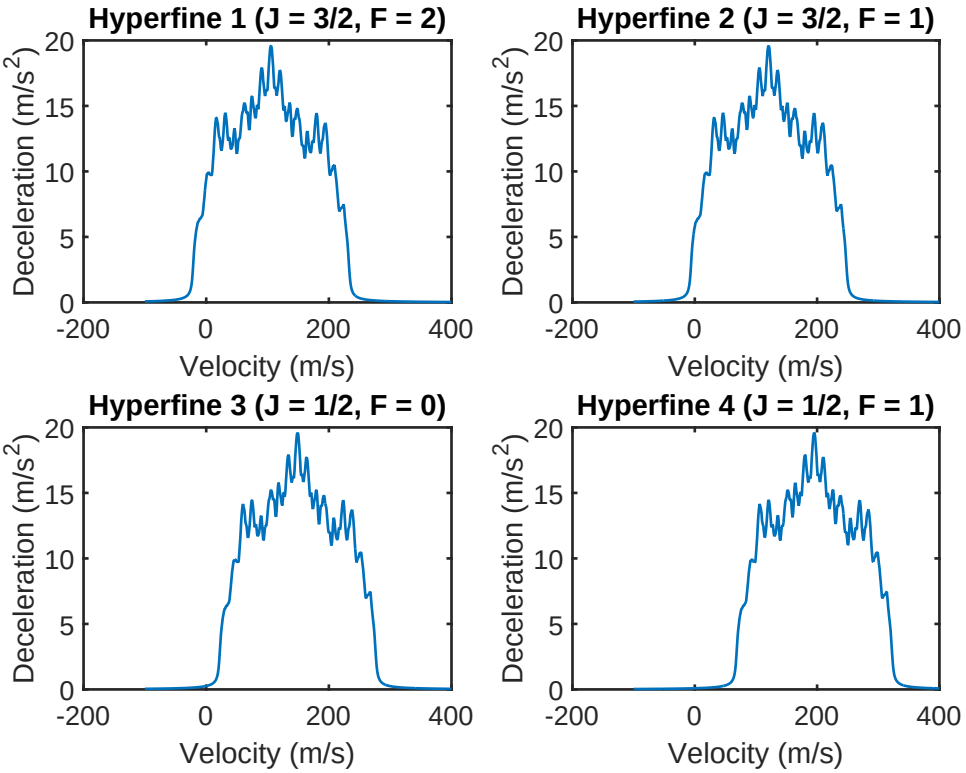

Figure 6.3.2: Deceleration from the slowing laser for each hyperfine state. The broadened slowing laser frequency in Fig. 6.3.1 is used for the calculation.

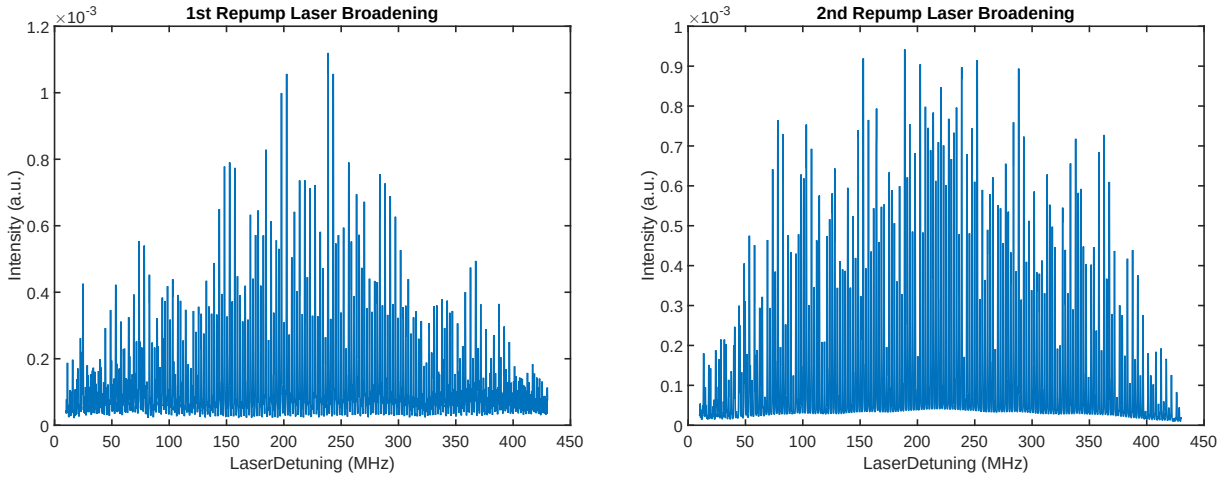

Figure 6.3.3: 1st and 2nd repump laser broadening from beat note measurements. The modulated light by the white-light EOM is beat with the unmodulated light shifted by about 220 MHz. 0 MHz in this plot is the unmodulated laser frequency.

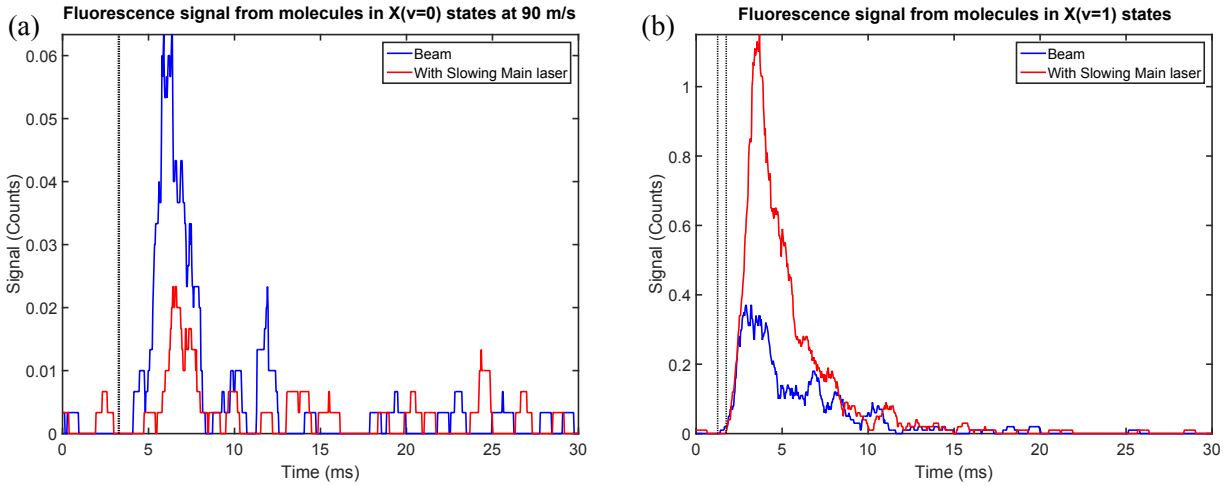

Figure 6.3.4: The YAG laser fires at $t = 0$ ms and generates the molecules. (a) Depletion of $X\,^2\Sigma(v = 0)$ molecules (at about 90 m/s) due to the main slowing laser. Main slowing laser was on for 50 μs at the time indicated as a dotted line. Main slowing laser power out of the fiber was 250 mW. (b) Accumulation of $X\,^2\Sigma(v = 1)$ molecules (all velocity class) due to the main slowing laser. Main slowing laser was on for 500 μs during the time indicated as a dotted line to address all the molecules coming out of the cell. Main slowing laser power out of the fiber was 190 mW. The blue trace shows the natural population in the $X\,^2\Sigma(v = 1)$ state out of the cell.

therefore takes place within a very short interaction time (about 16 μs assuming $2\pi \times 0.5$ MHz scattering rate). We indeed observed immediate depletion of the molecular beam in the $X\,^2\Sigma(v = 0)$ state by the main slowing laser with 50 μs interaction time, which was the shortest time interval limited by the data acquisition system (Fig. 6.3.4 (a)). To verify that the depleted molecules decayed to the $X\,^2\Sigma(v = 1)$ state, we monitored $X\,^2\Sigma(v = 1)$ state population and detected the increase of signal with the main slowing laser, confirming the optical pumping into the first excited vibrational state (Fig. 6.3.4 (b)).

These molecules in the $X\,^2\Sigma(v = 1)$ state come back to the $X\,^2\Sigma(v = 0)$ state when we shine the 1st repump laser. One scattering event of 1st repump photon would put the molecule back to the $v = 0$ state due to the highly diagonal Franck-Condon factor between the $X\,^2\Sigma$ state and $A\,^2\Pi_{1/2}$ state. However, the scattering rate of the 1st repump laser goes down also due to the small Franck-Condon factor between the $X\,^2\Sigma(v = 1)$ state and $A\,^2\Pi_{1/2}(v = 0)$ state. If the 1st repump laser has the same intensity to the main laser, the

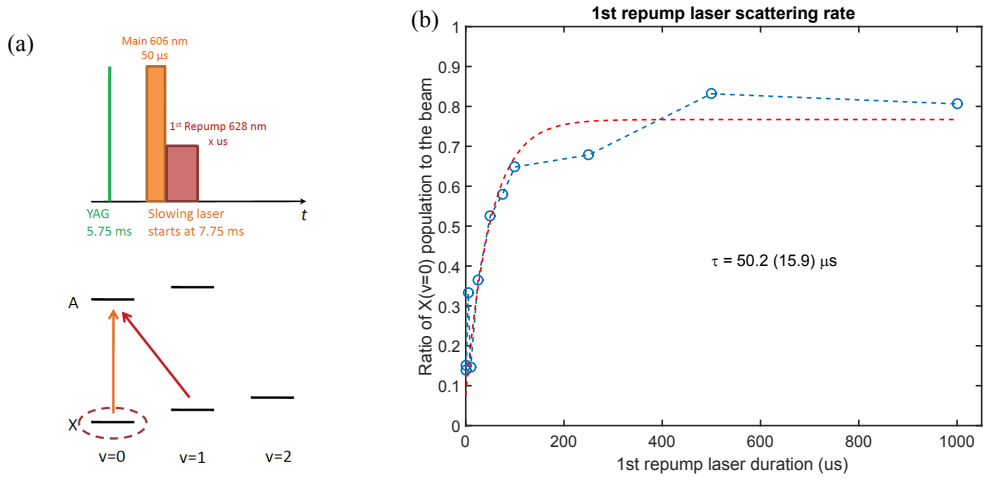

Figure 6.3.5: Scattering rate of slowing 1st repump laser. $\tau = 50.2$ μs with 95 % confidence intervals of 31.8 μs. The big uncertainty of the time constant is mainly due to the beam fluctuation from the ablation.

time constants of the two process - $v = 0$ to $v = 1$, and $v = 1$ to $v = 0$ - should be the same.

By changing the interaction time of the 1st repump lasers, we can extract the time constant of the 1st repump laser with 100 mW to pump the $X\,^2\Sigma(v = 1)$ molecules back to the $X\,^2\Sigma(v = 0)$ state. As one can see from the Fig. 6.3.5, about 50 μs is enough to pump the molecules back to the $X\,^2\Sigma(v = 0)$ state, which is comparable to the timescale of the optical pumping (from $v = 0$ to $v = 1$) due to the main laser considering the power difference.

When the main laser and the 1st repump laser share the same excited state, the probability for the molecule to be in the excited state is at maximum 1/7 (number of the excited states/total number of the states involved). If we can repump the molecules through a different excited state, like the next excited state $B\,^2\Sigma$, the maximum scattering rate of the main transition would increase by a factor of 7/4 since the maximum probability for the molecule to be in the excited state becomes 1/4. This requires fast repumping of the $X\,^2\Sigma(v = 1)$ state population through the $B\,^2\Sigma(v = 0)$ state with the accessible power budget. The $X\,^2\Sigma(v = 1)$ to $B\,^2\Sigma(v = 0)$ transition frequency is at 548 nm, which we can generate with Rhodamine 560 dye. We implemented both repumping schemes and compared them.

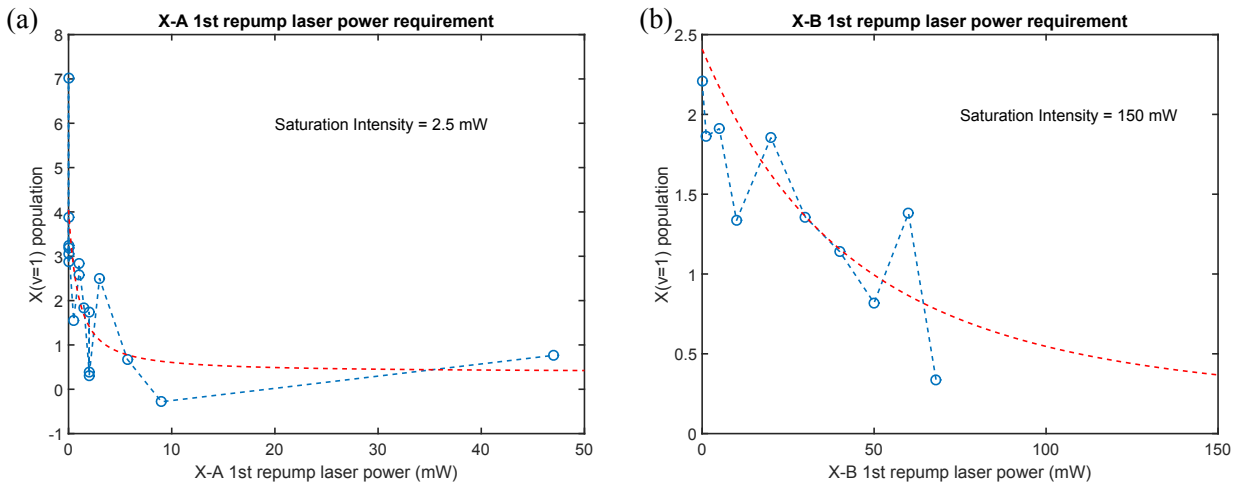

Figure 6.3.6: Comparison of the $X-A$ 1st repump scheme and the $X-B$ 1st repump scheme. All of the molecules are pumped into $X\,^2\Sigma(v=1)$ by the 0.5 ms long main laser pulse 1 ms after the YAG. The repump lasers were applied for 5.5 ms after the main laser to pump the molecules back to the $X\,^2\Sigma(v=0)$ and the $X\,^2\Sigma(v=1)$ population was monitored (blue circles). The red dotted lines are fitted line to a function $a\,\exp\left(-b\frac{I/I_0}{1+I/I_0}\right)+c$, where a, b, c, and I_0(saturation intensity) are free parameters. (a) The $X-A$ 1st repump laser. (b) The $X-B$ 1st repump laser.

To compare the efficiency of the two repump scheme, we first pumped all the molecules to the $X\,^2\Sigma(v=1)$ state by a 0.5 ms long pulse of the main laser and then used a 6 ms long pulse of the 1st repump lasers to pump the molecules back to the $X\,^2\Sigma(v=0)$ state. We monitored the $X\,^2\Sigma(v=1)$ population for the two different repumping schemes as we changed the power of the repump lasers. Unfortunately, the power requirement for the $X-B$ 1st repump laser is a lot more severe than the $X-A$ repump laser. This is due to the very high diagonal Franck-Condon factor between the $X\,^2\Sigma$ and the $B\,^2\Sigma$. The Franck-Condon factor for the $X-B$ 1st repump line is only 0.00134 where one for the $X-A$ 1st repump line is 0.0344, which is about 25 times bigger. Due to the constraint on the laser power, we decided to stick to the $X-A$ repump scheme.

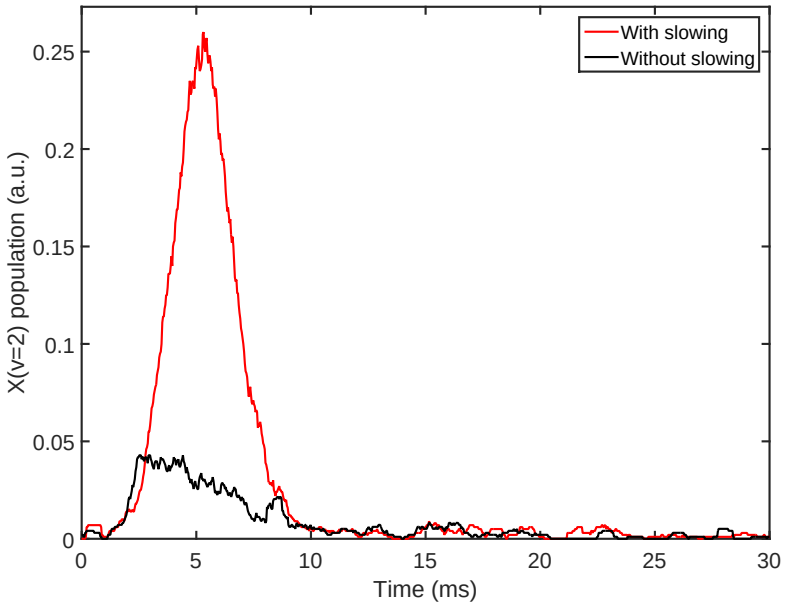

Figure 6.3.7: Accumulation in $X\,^2\Sigma(v=2)$ due to the main and 1st repump slowing lasers, from 0.75 ms to 7.25 ms after the YAG. The slowing lasers were maximum broadened by the white-light EOM and the hyperfine EOM.

6.3.2.2 Optimization of the optical pumping to the $X\,^2\Sigma(v=2)$ state by using the main and the 1st repump slowing laser

After studying the optical pumping between the $X\,^2\Sigma(v=0)$ and $X\,^2\Sigma(v=1)$ states, we put the main and the 1st repump slowing laser together to pump the molecules to the $X\,^2\Sigma(v=2)$ state. About 1000 photon scattering events are required for the molecules to decay to the $X\,^2\Sigma(v=2)$ state which corresponds to about 10 m/s momentum kick. Optimizing the optically pumped population in this $X\,^2\Sigma(v=2)$ state would put us in a good configuration for slowing as well. We monitored $X\,^2\Sigma(v=2)$ molecules using the $X-A-D$ two photon transition as we varied the slowing laser parameters, including the alignment of the slowing lasers. The accumulation in this state was quite sensitive to the slowing laser alignment, which makes sense since the lasers should interact with the molecules over 5 cm long distance in order to scatter about 1000 photons. The $X\,^2\Sigma(v=2)$ population after the optimization is shown in Fig. 6.3.7.

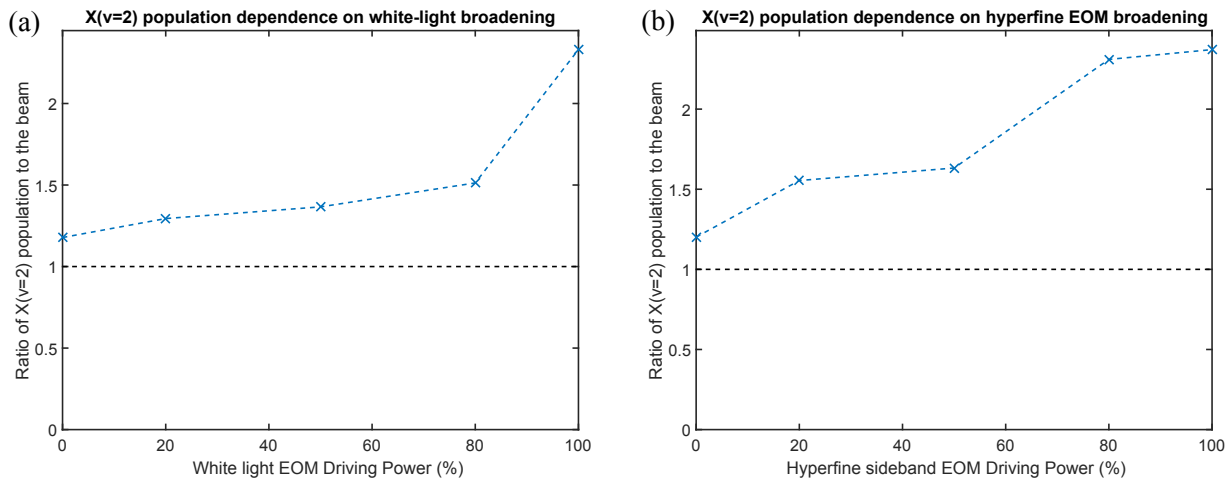

Figure 6.3.8: Accumulation into the $X\,^2\Sigma(v=2)$ state as a function of (a) the white-light EOM broadening with the hyperfine EOM driving power at 50%, (b) the hyperfine sideband EOM broadening with the white-light EOM driving power at 100 %. For both cases, the main and 1st repump lasers were on from 0.75 ms to 2.25 ms after the YAG. The current through the transverse field coils for the dark state mixing was 4 Amp. Ratio above 1 indicates accumulation due to the slowing lasers, and below 1 indicates depletion.

We first scanned the main and the 1st repump lasers to find the frequencies where we saw the maximum accumulation in the $X\,^2\Sigma(v=2)$ state. Then we tried different broadening from each EOM and found the maximum broadening gave the most number of molecules in the $X\,^2\Sigma(v=2)$ state (Fig. 6.3.8).

Next, we tried different time windows for the slowing lasers. Due to the nature of the buffer-gas beam, the molecular beam is pulsed with the envelop length about 1 ms to 5 ms, depending on the forward velocity of the molecules. When the slowing lasers start too early and hit the cell before the molecules come out from the cell, the cell heats up due to the slowing lasers and the molecular beam gets destroyed. If the slowing lasers start too late, the interaction time of the lasers and the molecules may be shortened. The optimal slowing laser time window also depends on where the molecules and the slowing lasers interact the most over the 50 cm long traveling distance.

Fig. 6.3.9 summarized the parameters we explored. By combining all the time space we explored, the time window from 1.5 ms to 3 ms after the YAG seems to be the most

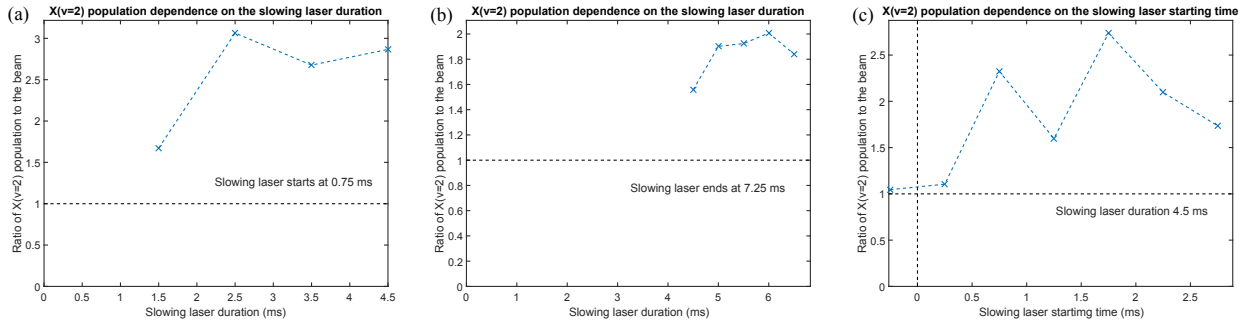

Figure 6.3.9: Accumulation into the $X\,^2\Sigma(v = 2)$ state as a function of (a) the slowing laser duration with the slowing laser starting at 0.75 ms after the YAG, (b) the slowing laser duration with the slowing laser ending at 7.25 ms after the YAG, (c) the slowing laser starting time with the slowing laser duration of 4.5 ms. For all data, the two EOMs were driven with the maximum power. Ratio above 1 indicates accumulation due to the slowing lasers, and below 1 indicates depletion.

critical window for the optical pumping to the $v = 2$ state. However, all the velocity classes were monitored in this measurement and depending on the velocities one wants to target, the slowing laser time window should change. This measurement still gives a good starting point when we look for a slowing signal.

Lastly, we tried different amount of current going through the transverse magnetic field coils to remix the dark substates. We didn't see a clear tendency here. The 4.5 ms of interaction time seems to be long enough to scatter 1000 photons and pump the molecules into the $X\,^2\Sigma(v = 2)$ state with only the Earth's field to remix the dark states.

6.3.3 Redistribution of hyperfine states due to slowing laser

Due to the different Clebsch-Gordan coefficients of the transitions between the excited states and the different hyperfine ground states, redistribution of the hyperfine states occurs due to the optical pumping effect from the slowing lasers. This effect is also molecular velocity dependent because the broadened slowing lasers are counter-propagating to the molecular beam, causing Doppler shifts. Since we are detecting only one of the hyperfine states, we need to consider this effect as well when we compare the data with and without the slowing lasers.

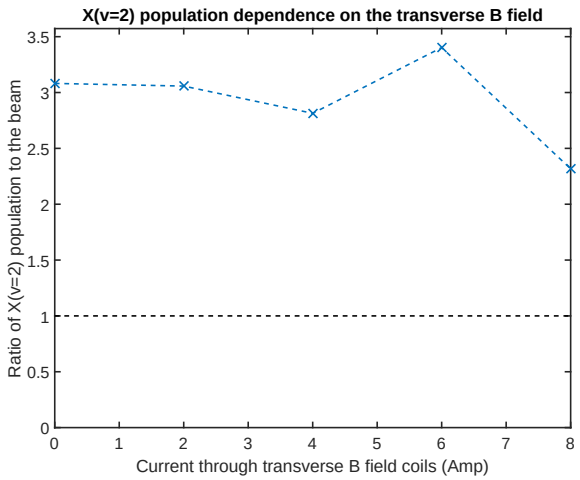

Figure 6.3.10: Accumulation into the $X\,^2\Sigma(v = 2)$ state as a function of the transverse B field. The slowing laser window was from 0.75 ms to 5.25 ms from the YAG. The two EOMs were driven with the maximum power. Ratio above 1 indicates accumulation due to the slowing lasers, and below 1 indicates depletion.

Fig. 6.3.11 is the result of the optical pumping simulation due to the slowing laser after certain amount of photon scattering. The actual spectrum of broadened main slowing laser (Fig. 6.3.1) is used to calculate relative absorption rate for molecules at certain velocity for each hyperfine state. Optical pumping effect occurs very fast and is mostly done after only 20 photon scatters.

The hyperfine state that we are monitoring is $X\,^2\Sigma(v = 0, N = 1, J = 1/2, F = 1)$ state (purple line in Fig.6.3.11), where molecules are accumulated due to the redistribution. Especially for slow velocities, we tuned our slowing laser frequency so that the bluest laser frequency component is resonant with molecules in $X(v = 0, N = 1, J = 1/2, F = 1)$ state with around 50 m/s forward velocity. All molecules slower than that would accumulate in our monitoring state and would not be slowed further.

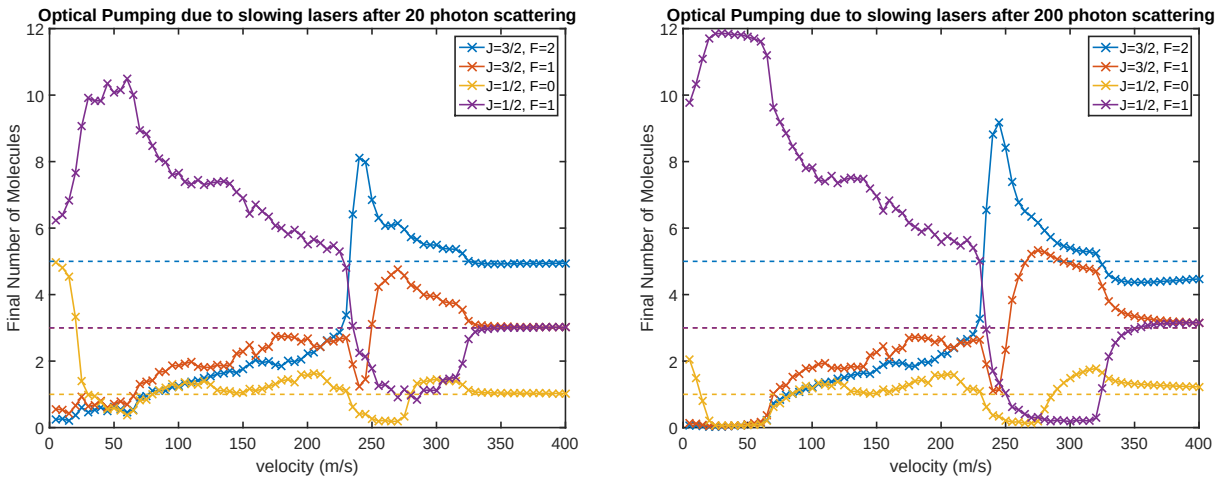

Figure 6.3.11: Redistribution of hyperfine states due to slowing lasers after 20 and 200 photon scattering. Dotted lines are the initial relative population in the hyperfine states considering the number of magnetic substates.

6.3.4 White-light slowing of CaF molecules

6.3.4.1 Simulation

Using the calculated deceleration for each hyperfine state in Fig. 6.3.2 and the slowing laser time window, we can simulate the velocity change for each hyperfine state we would expect. We can see that the $X\,^2\Sigma(v=0, N=1, J=1/2, F=1)$ state that we are monitoring is not affected much below 50 m/s since the slowing laser frequencies are out of resonance below 50 m/s. Similar effect is seen in the $X\,^2\Sigma(v=0, N=1, J=1/2, F=0)$ state below 10 m/s. Molecules in the other $X,\ ^2\Sigma(v=0, N=1, J=3/2, F=1, 2)$ states that are slowed down to these low velocities would be optically pumped to the $X\,^2\Sigma(v=0, N=1, J=1/2, F=0, 1)$ states and wouldn't be slowed further. According to the simulation, most of the slowed molecules arrive at the detection area (MOT center) between 5 ms and 15 ms after the YAG, which agrees with the experiment.

6.3.4.2 Results

Velocity distribution Fig. 6.3.13 summarizes the main result of the laser slowing of CaF molecules. For all slowing measurements, the white-light EOM was driven with 50 % power

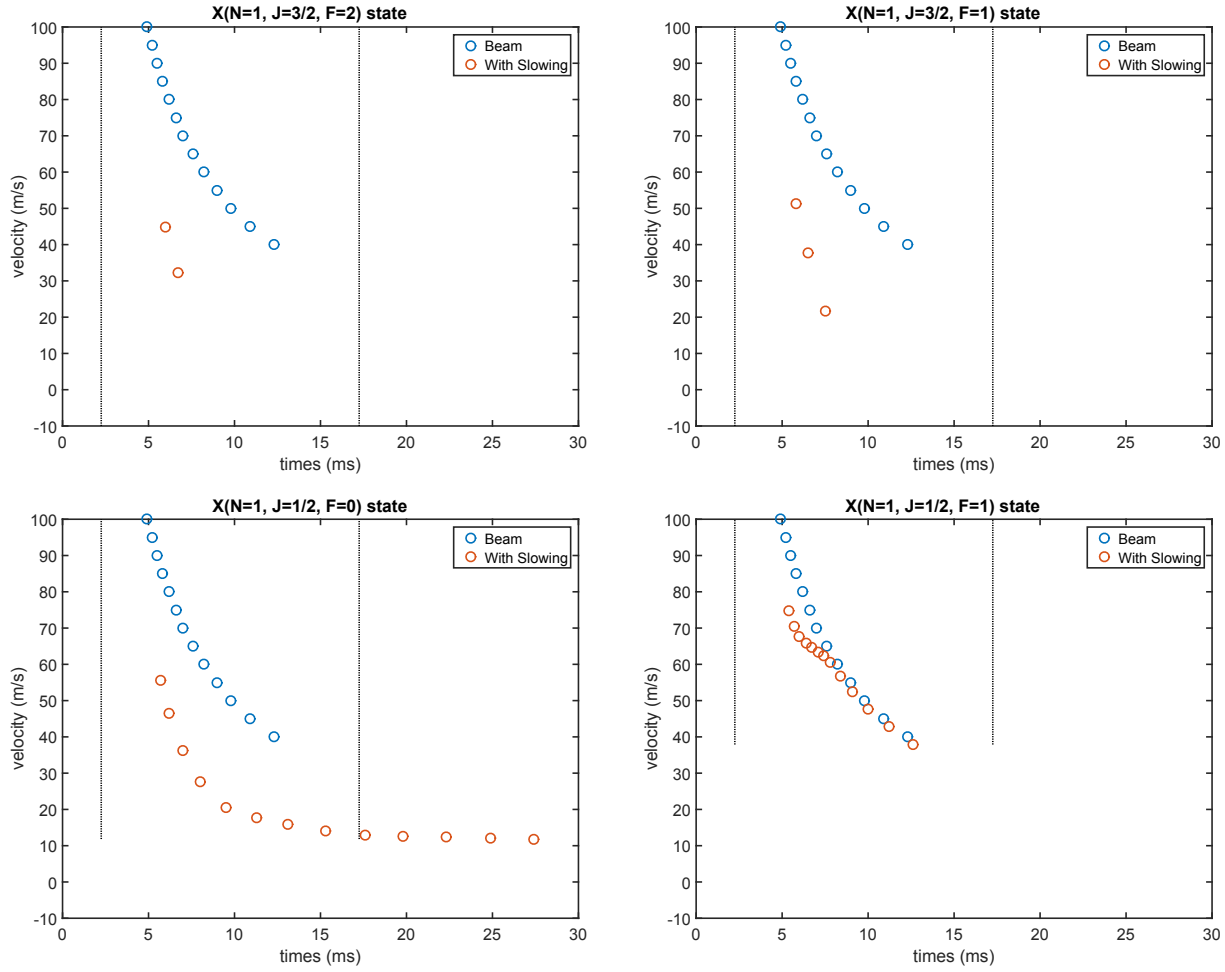

Figure 6.3.12: Time-of-flight simulation for each hyperfine state. The dotted vertical lines are the slowing laser window that we actually used in the experiment. Blue circles are the beam velocities and the corresponding arrival time to the MOT center from the cell. The red circles indicate the velocities and the arrival time when the molecules receive deceleration in Fig. 6.3.2 for each hyperfine during the slowing laser time window.

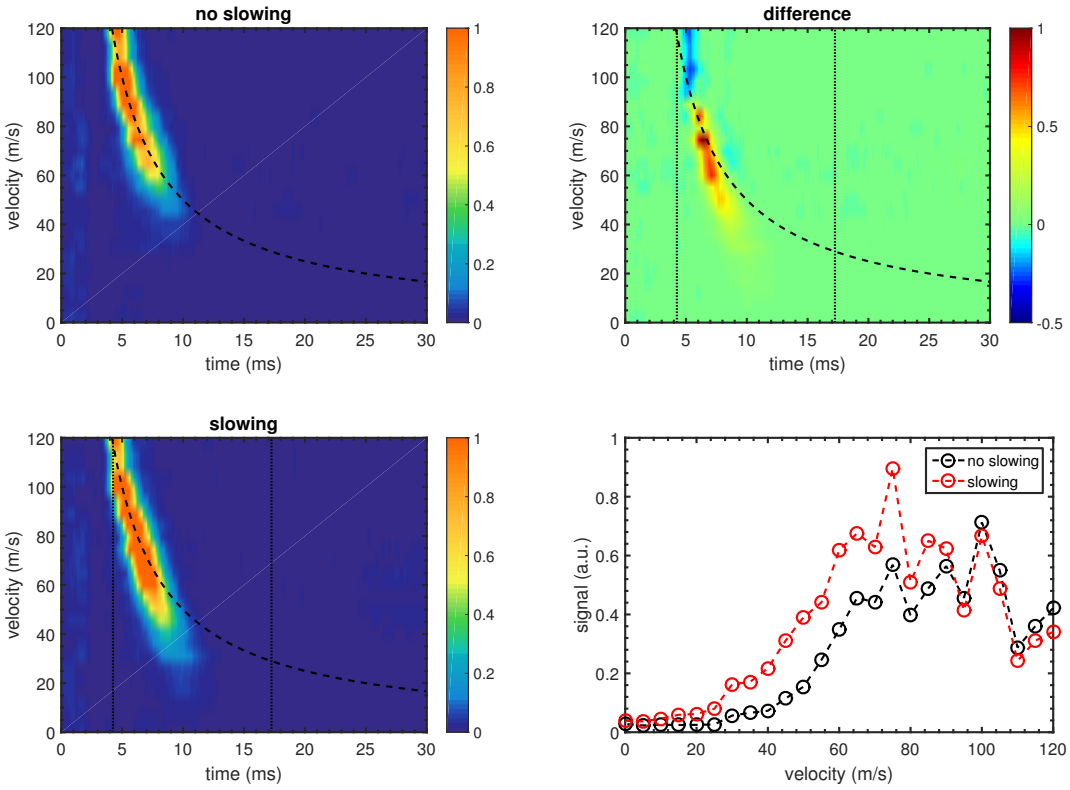

Figure 6.3.13: Velocity scan of the molecular beam with/without slowing lasers and the difference. In the difference plot, the blue area indicates depletion due to the slowing lasers, and the red area indicates accumulation. The bottom right plot is the same data integrated from 2 ms to 50 ms. The dotted vertical lines indicate the time slowing lasers are applied. Data were taken on 2015/07/14, the 2nd day of the run.

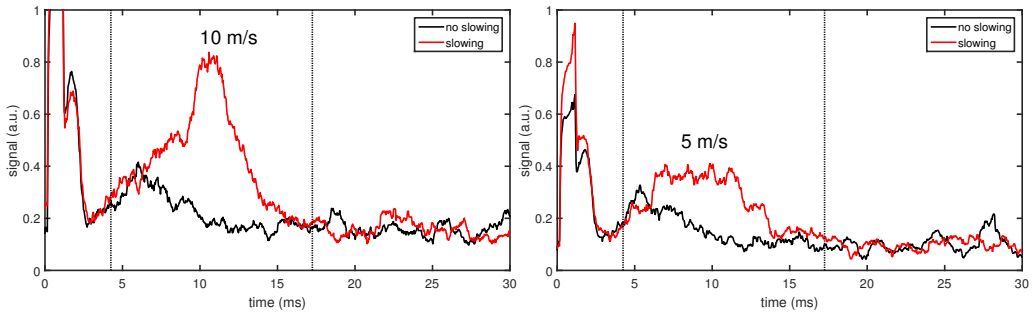

Figure 6.3.14: Timetrace of molecules with forward velocity of 10 m/s and 5 m/s. Red traces are the signal when slowing lasers are applied and the black ones are the beam signal our of the cell. The dotted vertical lines indicate the time slowing lasers are applied. Data were taken on 2015/07/14, the 2nd day of the run. The beam signal (black) at around 5 ms is from some random glow after the YAG, same as signal between 0 ms and 3 ms.

and the hyperfine EOM was driven with 100 % power. It is clear that the higher velocity classes are depleted due to the slowing laser and the slow velocity below 30 m/s appeared. The timetrace for 10 m/s and 5 m/s velocity is shown in Fig. 6.3.14.

Although we haven't seen an effect of the transverse magnetic field for the dark states while monitoring the $X\,^2\Sigma(v = 2)$ state accumulation, we see a clear effect on the slowing efficiency (Fig. 6.3.15). Overall velocity change is less and the fat tail below 40 m/s with the remixing field disappeared without the field.

The slowing is strongly dependent on the slowing laser frequencies. There are three slowing lasers involved (the main, the 1st, and the 2nd repump lasers) and ideally we need to tune all three lasers frequencies independently. However, due to the time constraints (each scan took about 45 minutes), we moved all the slowing laser frequencies together and took three velocity scans with different frequencies (Fig. 6.3.16). As the slowing laser frequencies become higher, the peak velocity after slowing moves to lower velocity since we are addressing slower molecules. There are optimal slowing laser frequencies for maximum number of molecules below 20 m/s, since the initial velocity and the initial flux at that velocity both matter.

We also varied the slowing laser starting time and the results are depicted in Fig. 6.3.17. Only the main slowing laser starting time was varied. Having the slowing on for the time

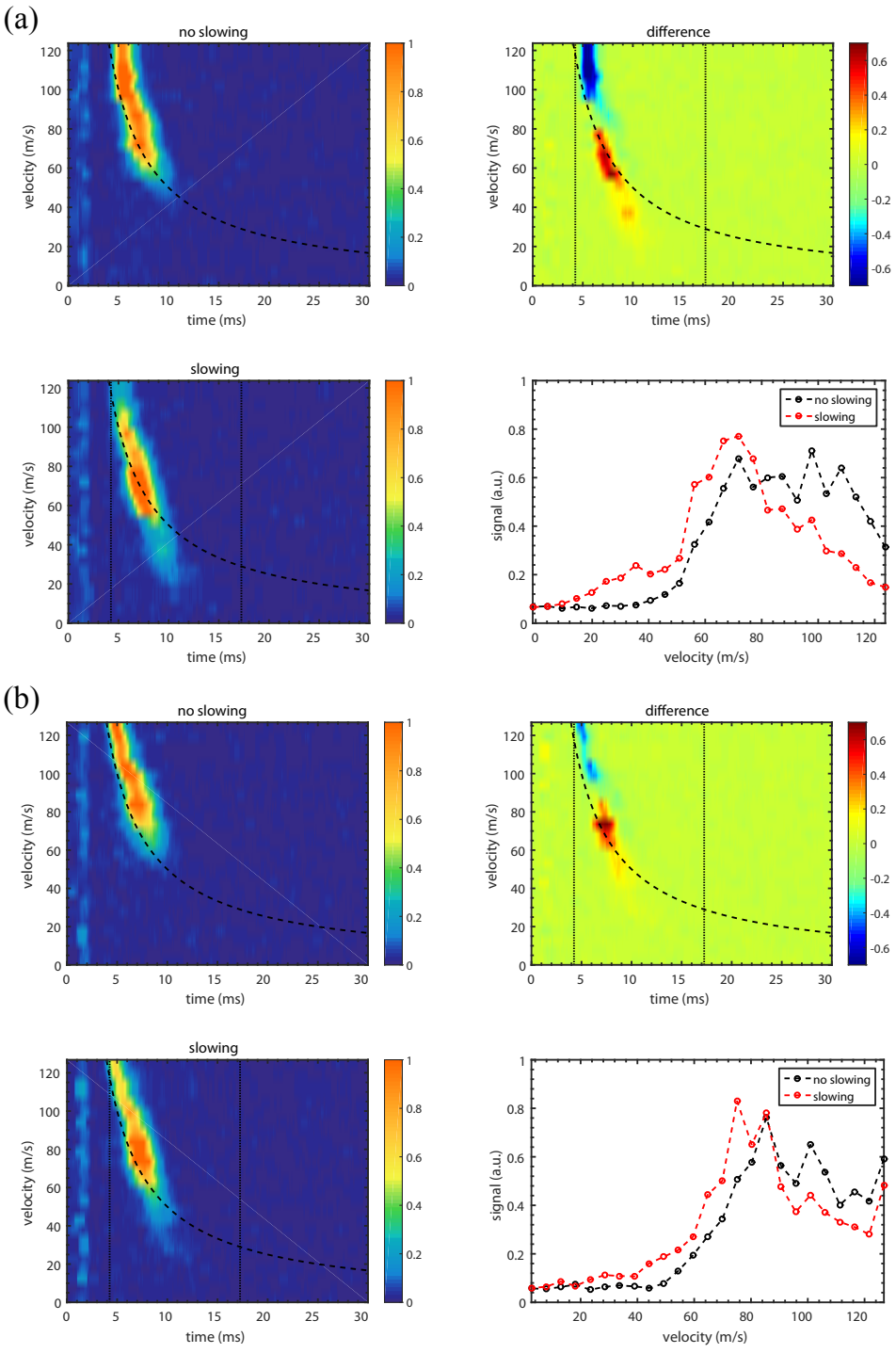

Figure 6.3.15: Effect of the transverse magnetic field. (a) With the transverse magnetic field on (4 Amp current through the coils). (b) Without the transverse magnetic field. More number of molecules are slowed down to below 20 m/s with the field on. Data were taken on 2015/07/15, the 3rd day of the run.

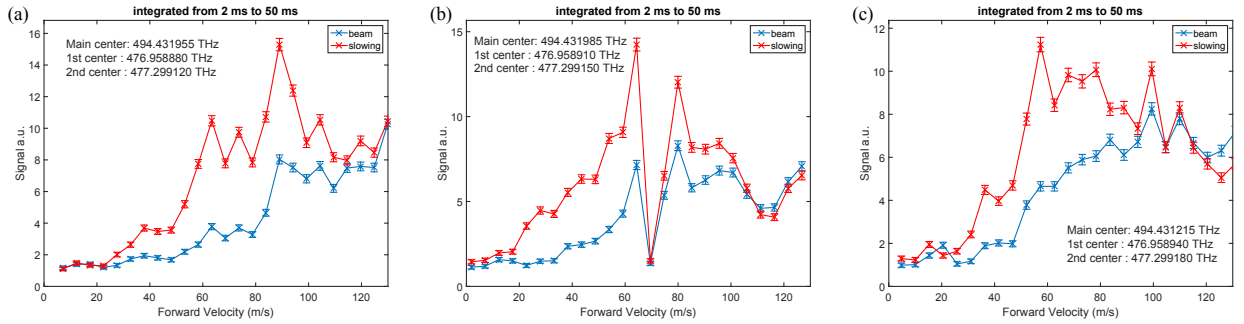

Figure 6.3.16: Slowing lasers detuning dependence. The frequencies of the slowing lasers are indicated in the plot. All data were taken on 2015/07/21, the 4th day of the run.

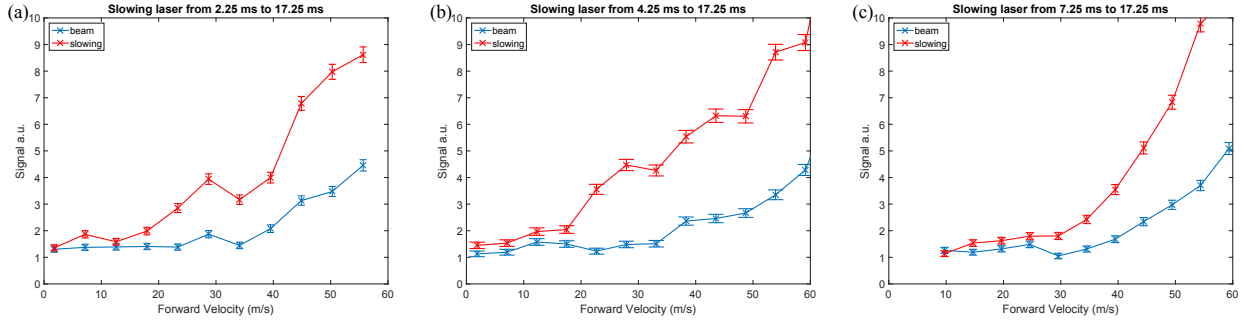

Figure 6.3.17: Slowing laser starting time dependence. (a) main slowing laser from 2.25 ms to 17.25 ms . (b) main slowing laser from 4.25 ms to 17.25 ms. (c) main slowing laser from 7.25 ms to 17.25 ms. All data are taken on 2015/07/21 the 4th day of the run.

window from 4.25 ms to 7.25 ms seems to be crucial to achieve molecules slower than 30 m/s. This is when molecules with the forward velocities of 60 - 100 m/s fly through the entrance of the MOT chamber and we can infer that these are the molecules we slow down to below 30 m/s.

Molecule number estimation Here, we estimate how many molecules we have when we detect 1 count on the PMT (Hamamatsu R7600P). Here are the needed parameters.

- Hamamatsu R7600P quantum efficiency at 331 nm : 25 %
- Hamamatsu R7600P gain at 800 V supply voltage : 2×10^6
- Geometric collection efficiency : ~ 1/50
- Number of photons per molecule : let's assume 0.8 (conservative)

- Filters in front of the PMT : 80 % transmission for a colored glass, 85 % transmission for a interference filter from Semrock (FF01-335/7-25) $\times$ 2

Let's track down the number of molecules. Since we are using photon-counting mode, it should be a lot straight forward compared to the analog mode. From the quantum efficiency of 25 %, there are $1/0.25/0.8/0.85^2 = 7$ photons incident to the PMT when we detect 1 count. That means, assuming the loss from all the optics is ~ 20 %, there were $7 \times 50/0.8 = 440$ photons from the molecules, which indicates that there are > 440 molecules in the detection region.

It is quite difficult to estimate how many photons are emitted per molecule. The upper bound is 1 photon per molecule, which means we excite all the molecules to the C state and all of them decay to the X state within our detection time, which is unrealistic. Since the branching ratio from the C state to other lower excited states ($B\,^2\Delta_{3/2}$, $B\,^2\Sigma$, $A\,^2\Pi_{3/2}$, and $A\,^2\Pi_{1/2}$) are unknown, it is impossible to accurately estimate how many photons we get per molecule. We can crudely estimate the probability for a molecules in the $C\,^2\Pi_{1/2}(J = 1/2, -)$ state to decay back to the ground state (any state in $X\,^2\Sigma$ state) by assuming the dipole matrix element between the C state and other states are all same. Then, the transition probability only depends on the number of states in the final state the molecule can decay to and the wavelength of that transition. This rough estimation gives ~ 80 % probability back to the ground state $X\,^2\Sigma$, leading $440/0.8 \sim 550$ molecules in the $C\,^2\Pi_{1/2}(J = 1/2, -)$ state when we detect one count on the PMT.

The number of averaged counts we detect for 10 m/s, 5 m/s, and 0 m/s molecules are 0.19, 0.23, and 0.02 respectively. These sum up to 0.44 counts, which corresponds to about 240 molecules we excited to the $C\,^2\Pi_{1/2}(J = 1/2, -)$ state and this gives us the lower bound of the number of the ground state molecules. There is still a big unknown factor of what portion of the molecules in the ground state is excited to the C state.

The other approach to calculate the number of molecules below 10 m/s is comparing integrated signal for molecules with forward velocity < 10 m/s to the total integrated signal

for all molecules, assuming we know the number of total number of molecules out of the cell reaching into the MOT region. Assuming we have $\sim 10^9$ molecules out of the two-stage cell [82], $\sim 10^5$ molecules reach to the 50 cm downstream MOT center within 1 cm^3 volume using effusive beam divergence of $\cos\theta$, which is a conservative estimation since our beam is still slightly boosted. The ratio of signal from molecules below 10 m/s to the total number of molecules from the data in Fig. 6.3.13 is ~ $1/(60\times4)$ ~ 0.0042. The factor of 4 comes from the fact that we monitor only single hyperfine state ($J = 1/2$, $F = 1$), which has population of 1/4 of total, for the beam, but we should assume that all molecules slowed down to below 10 m/s are optically pumped into this hyperfine state due to the hyperfine state redistribution from slowing lasers. This number is also quite conservative since the off-resonant fluorescence of faster molecules is also summed to the total signal. From above, we can estimate the number of molecules below 10 m/s is ~ 420, which is consistent with the estimation from the number of detected UV photons.

Chapter 7

AC MOT for ^{6}Li and Progress Towards dual AC MOT for ^{6}Li and CaF

In this chapter, progress towards co-trapping atoms(^{6}Li) and molecules(CaF) in a AC magneto-optical trap are summarized. Due to the complicated structure of the molecules, an AC MOT is required for trapping molecules, and as a consequence, atoms need to be loaded into the same AC MOT. A brief explanation of AC MOT and the results of simulations are shown, followed by experimental results of AC MOT for ^{6}Li.

7.1 Brief description of AC magneto-optical trap

Due to the rotational degree of freedom in CaF molecules, one needs to use $X\,^2\Sigma(N = 1,\, J = 3/2,\, 1/2)$ to $A\,^2\Pi_{1/2}(J = 1/2,\, +)$ transition to form a rotationally closed cycling transition where there are more number of states in the electronic ground state than in the excited state. When this transition ($J \rightarrow J,\, J-1$) is used to form a magneto-optical trap (MOT), this type of MOT is called type II MOT. The typical configuration where the excited state has more number of states than the ground state using $J \rightarrow J+1$ transition is named as type I MOT. Although this type II MOT should not form a trap due to the fast optical pumping to the states which are dark to the trapping light (and bright to the anti-trapping

light), people have made type II MOTs for sodium atoms using D2 line[91] and also D1 line [92], thanks to the existence of multiple excited states and complicated magnetic field configuration in 3D MOTs [93]. However, the type II MOT is hotter and fewer in number of trapped atoms than the usual type I MOT.

To prevent atoms or molecules from staying in the dark states, one can either use an angled transverse magnetic field to let the dark state precess to the bright state, or switch polarization of the light so that the dark states then become bright states [80]. For slowing, we used a transverse magnetic field to mix the dark magnetic substates. However, we cannot use the same strategy since the B field will disturb the MOT field gradient. Instead, we chose to use polarization switch to remix the dark states. At the same time, one also needs to switch the magnetic field gradient direction so that the detuning of the trapping laser is matched with the bright states (Fig. 7.1.1). This type of a MOT is called an AC MOT. The switching of both polarization and B field should happen at the frequency of the scattering rate of photons, which is on the order of MHz, to prevent the dark states from lowering the scattering rate. This AC MOT is also called as a RF MOT when the switching frequency is high so that it is in the radio-frequency regime. The typical MOT with fixed polarization and B field is denoted as a DC MOT.

The AC MOT has been demonstrated at kHz frequencies for potassium atoms [94]. However, the transition that the authors used in that experiment didn't have any dark states and it was more like an extension of a DC MOT. The AC MOT for molecules with dark states was first demonstrated in 2D configuration using YO molecules [53], and recently, a 3D AC MOT for SrF molecules has been reported [59]. The AC MOT SrF improved all aspects of the MOT properties - the number of trapped molecules, the lifetime of the MOT, the temperature of the cloud, the density of the cloud, and the phase space density - compared to the DC MOT for SrF according to Ref. [59]. Most notably, the phase space density has been improved by three orders of magnitude, proving that the AC MOT is the way to go for molecules.

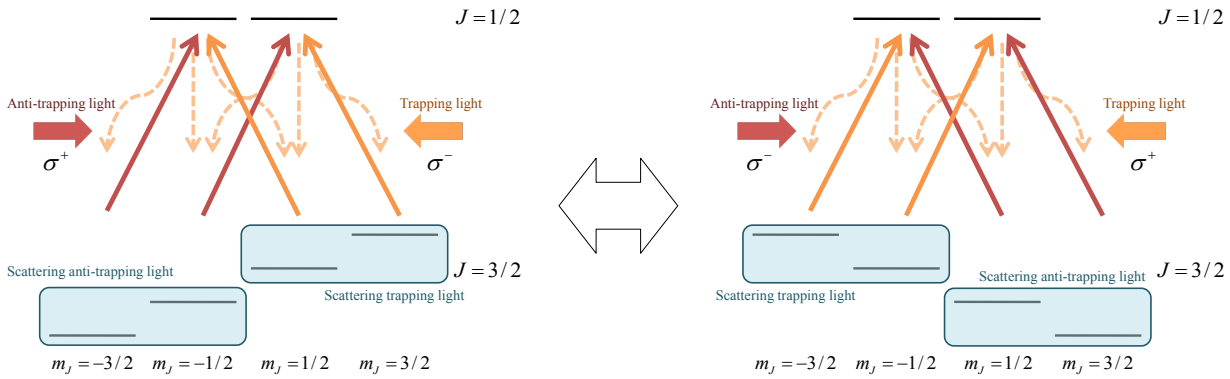

Figure 7.1.1: Schematic of an AC MOT. Switching of the polarization and the B field ensures that all the magnetic substates scatter trapping photons continuously.

The capture velocity of a MOT for a simple atomic system can be estimated using a simple equation

$$v_c = \sqrt{a\, r_c} \tag{7.1.1}$$

, where a is the acceleration from the laser on resonance and r_c is the radius of the MOT beams [90]. By using appropriate parameters for CaF in this experiment, the capture velocity would be ∼14 m/s. To accommodate the complexity of molecular structure, 1D simulation of MOT capture velocity has been performed and summarized in the next section.

7.2 Magneto-optical trap for CaF capture velocity simulation

The force applied to molecules in MOT beams is $\mathbf{F} = \mathbf{F}_+ + \mathbf{F}_-$ where

$$\mathbf{F}_\pm = \hbar \mathbf{k}_\pm \Gamma_{eff} \tag{7.2.1}$$

$$= \hbar \mathbf{k}_{\pm} \gamma \, P_{ex} \frac{s}{1 + s + (2\delta_{\pm}/\gamma)^2} \tag{7.2.2}$$

is the force from the $\sigma^{\pm}$ polarization light with wavevector $\mathbf{k}_{\pm}$, where Γ_{eff} is the effective scattering rate, $\gamma = 2\pi \times 8.29$ MHz is the linewidth of the excited states [69], and s is the saturation parameter. The detuning $\delta_{\pm}$ of each $\sigma^{\pm}$ laser beam is given by

$$\delta_{\pm} = \delta_0 - \mathbf{k}_{\pm} \cdot \mathbf{v} - \mu'_{\pm} B(\mathbf{r})/\hbar$$

due to the Doppler shift and Zeeman shift. The detuning of the laser with respect to the molecules with 0 m/s velocity in a no B field environment is defined $\delta_0 = f - f_0$ where f is the laser frequency and $f_0$is the resonant frequency of the molecule. $-\mathbf{k}_{\pm} \cdot \mathbf{v}$ indicates the Doppler shift of the molecule's resonance and $-\mu'_{\pm} B(\mathbf{r})/\hbar$ indicates the Zeeman shift at the position $\mathbf{r}$. $\mu'_{\pm} \equiv (g_e M_e^{\pm} - g_g M_g^{\pm})\mu_B$ is the effective magnetic moment for the transition used, and the magnetic substate quantum number $M_{e,g}^{\pm}$ indicates the magnetic substate the laser is coupling to with $\sigma^{\pm}$ polarization.

P_{ex} represents the maximum probability for the molecule being in the excited states. In the two level system, $P_{ex} = \frac{1}{2}$. The radiative force to the molecules comes from the spontaneous decay from the excited $A\,^2\Pi_{1/2}(v = 0,\, J = \frac{1}{2},\, +)$ states that are coupled to the ground states of $X\,^2\Sigma(v = 0,\, N = 1)$ and $X\,^2\Sigma(v = 1,\, N = 1)$. Assuming both main and 1st repump transitions are saturated, the molecules spend equal amount of time among all the states above and the P_{ex} becomes

$$\begin{aligned} P_{ex} &= \frac{\text{Number of states in } A\,^2\Pi_{\frac{1}{2}}(v = 0,\, J = \frac{1}{2},\, +)}{\text{Number of all states } (X\,^2\Sigma(v = 0, 1,\, N = 1) \text{ and } A\,^2\Pi_{\frac{1}{2}}(v = 0,\, J = \frac{1}{2},\, +))} \\ &= \frac{4}{28} = \frac{1}{7} \end{aligned} \tag{7.2.3}$$

. Using the saturation parameter of $s = 1$, the effective scattering rate Γ_{eff} on resonance is $2\pi \times 0.59$ MHz.

$X\,^2\Sigma$ states	g_F
$N=1,\ J=\frac{3}{2},\ F=2$	$\frac{1}{2}$
$N=1,\ J=\frac{3}{2},\ F=1$	$\frac{5}{6}$
$N=1,\ J=\frac{1}{2},\ F=0$	0
$N=1,\ J=\frac{1}{2},\ F=1$	$-\frac{1}{3}$

Table 7.1: g_F factors of $X\,^2\Sigma$ states

Zeeman shift from the applied magnetic field differs in different hyperfine states due to the different g_F factor. The molecular Lande-g factor for Hund's case (b) ($X\,^2\Sigma$) states is

$$\begin{aligned} g_F &= \left(\frac{\Lambda^2}{N(N+1)}\frac{J(J+1)+N(N+1)-S(S+1)}{2J(J+1)}+2\frac{J(J+1)-N(N+1)+S(S+1)}{2J(J+1)}\right) \\ &\times\left(\frac{F(F+1)+J(J+1)-I(I+1)}{2F(F+1)}\right) \\ &+g_I\frac{\mu_N}{\mu_B}\frac{F(F+1)-J(J+1)+I(I+1)}{2F(F+1)} \end{aligned} \tag{7.2.4}$$

, and the one for Hund's case (a) ($A\,^2\Pi$) states is

$$g_F=(\Lambda+2\Sigma)\frac{\Omega}{J(J+1)}\frac{F(F+1)+J(J+1)-I(I+1)}{2F(F+1)}+g_I\frac{\mu_N}{\mu_B}\frac{F(F+1)-J(J+1)+I(I+1)}{2F(F+1)} \tag{7.2.5}$$

, where g_I is the g-factor of nucleus [78]. Since $\frac{\mu_N}{\mu_B}$ is on the order of the mass ratio of an electron to a proton, we can ignore the contribution from the nuclear magnetic moment. The excited $A\,^2\Pi_{1/2}$ states that we are interested have $\Lambda=1$ and $\Sigma=-\frac{1}{2}$, forming $\Omega=\frac{1}{2}$. This leads the g_F of the A states to be zero. The g_F of the X states are summarized below in Table 7.1. Note that one of the ground states has the opposite sign of the g_F factor and needs the opposite laser polarization to the others.

To address all the hyperfine states in the ground state, which are separated by 10s of MHz, we have four frequencies in the MOT laser beams generated by acoustic-optic modulators (AOMs). Each hyperfine state has different g_F factor and the detunings are different for each hyperfine state. Furthermore, each laser frequency which is intended for one particular hyperfine affects other hyperfine states also since the spacing of the hyperfine structure

is similar to the Doppler shift and the Zeeman shift from the magnetic field for a MOT. Therefore, the total force on one hyperfine state is the sum of the forces from all frequencies of the two counter-propagating lasers. Assuming the time that the molecules spend in one hyperfine state is equal among different hyperfine states, we can simplify the problem by assuming the molecules would receive the averaged force for all the hyperfine states.

Here, we simulate the trajectory of the CaF molecule entering the MOT region in 1D system. Assuming our laser beam has a diameter d, the molecule starts to feel the force from all three lasers at the position $-d/2$ with the initial velocity v_0 in 3D system and we use these condition as our initial condition.

For each time segment $\Delta t = 1/\gamma$, the molecule receives force $F(x_n)$, which is a function of the velocity and position, from the laser and the velocity and the position of the molecule change.

$$v_{n+1} = \frac{F(v_n,\, x_n)}{M_{CaF}}\,\Delta t + v_n \tag{7.2.6}$$

$$x_{n+1} = v_n\,\Delta t + x_n \tag{7.2.7}$$

where M_{CaF} is the mass of CaF. Here, the position is denoted as x and the velocity as v with the subscript indicating the number of photon scattering events. The molecules are let to evolve 10^5 cycles, which is our photon budget with two vibrational repump lasers.

The results are summarized in Fig. 7.2.1 and Fig. 7.2.2. Two cases with the magnetic field gradient of 10 Gauss/cm and 20 Gauss/cm are studied. The saturation parameter is set to 1 considering the experimental condition. For both cases, the capture velocity is about 13 m/s, which is similar to the simple estimation from Eq. 7.1.1. This indicates that the reduced scattering rate due to the many number of involved states is the limiting factor for the capture velocity.

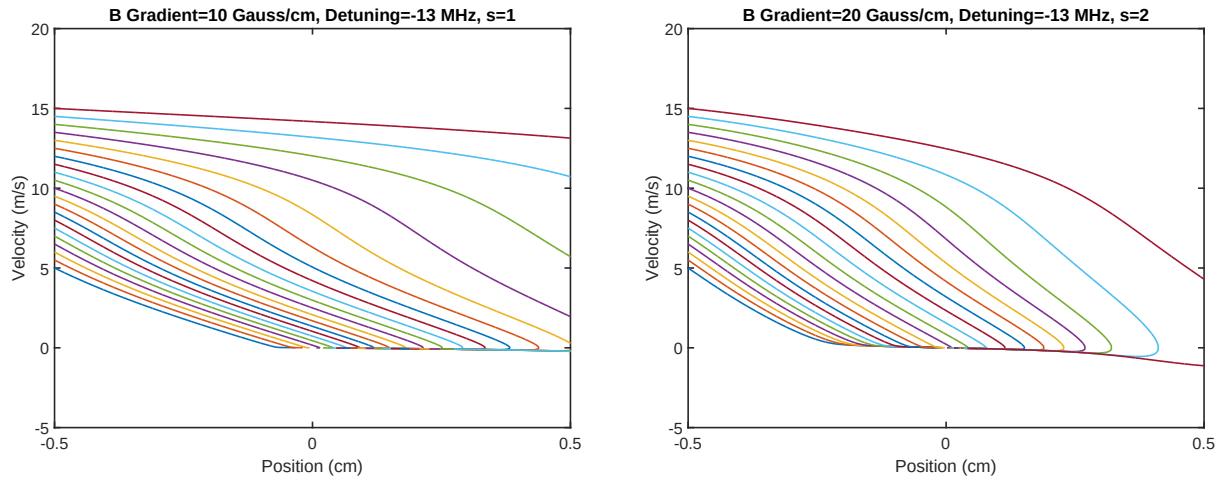

Figure 7.2.1: Examples of the MOT capture velocity 1D simulation. Leftside is with the B field gradient of 10 Gauss/cm, saturation parameter of 1, and δ_0 of 12 MHz. Rightside is with the B field gradient of 20 Gauss/cm, saturation parameter of 1, and δ_0 of 12 MHz. Initial velocities are given from 5 m/s to 15 m/s, with increments of 0.5 m/s. In both cases, the capture velocity is 12 m/s.

7.3 AC MOT for ^{6}Li atoms

We first made a DC MOT of ^{6}Li using the D2 line with the white-light slowing also with the D2 line. Fig. 7.3.1 shows the ^{6}Li DC MOT at the center of the MOT coils. The MOT didn't form when the slowing laser was blocked, showing that the MOT capture velocity is lower than the velocity of the ^{6}Li beam out of the cell due to ^{6}Li's light mass. After we optimized all the parameters - beam alignment and slowing laser frequency - with the D2 line DC MOT, we moved on to make a MOT using D1 transition (addressing $F = 3/2$ state in the excited state).

We made both a DC MOT and an AC MOT of ^{6}Li using D1 transition and saw dramatic difference between the DC and the AC MOTs. The AC MOT showed more number of atoms inside the MOT and longer lifetime of the MOT compared to the DC MOT which met our expectation (Fig. 7.3.2).

Fig. 7.3.3 shows one of the best AC MOT timetraces detected by our PMT (Hamamatsu R8900U-20). The experimental parameters to get this signal were, 1.9 Amp = 19 Gauss/cm

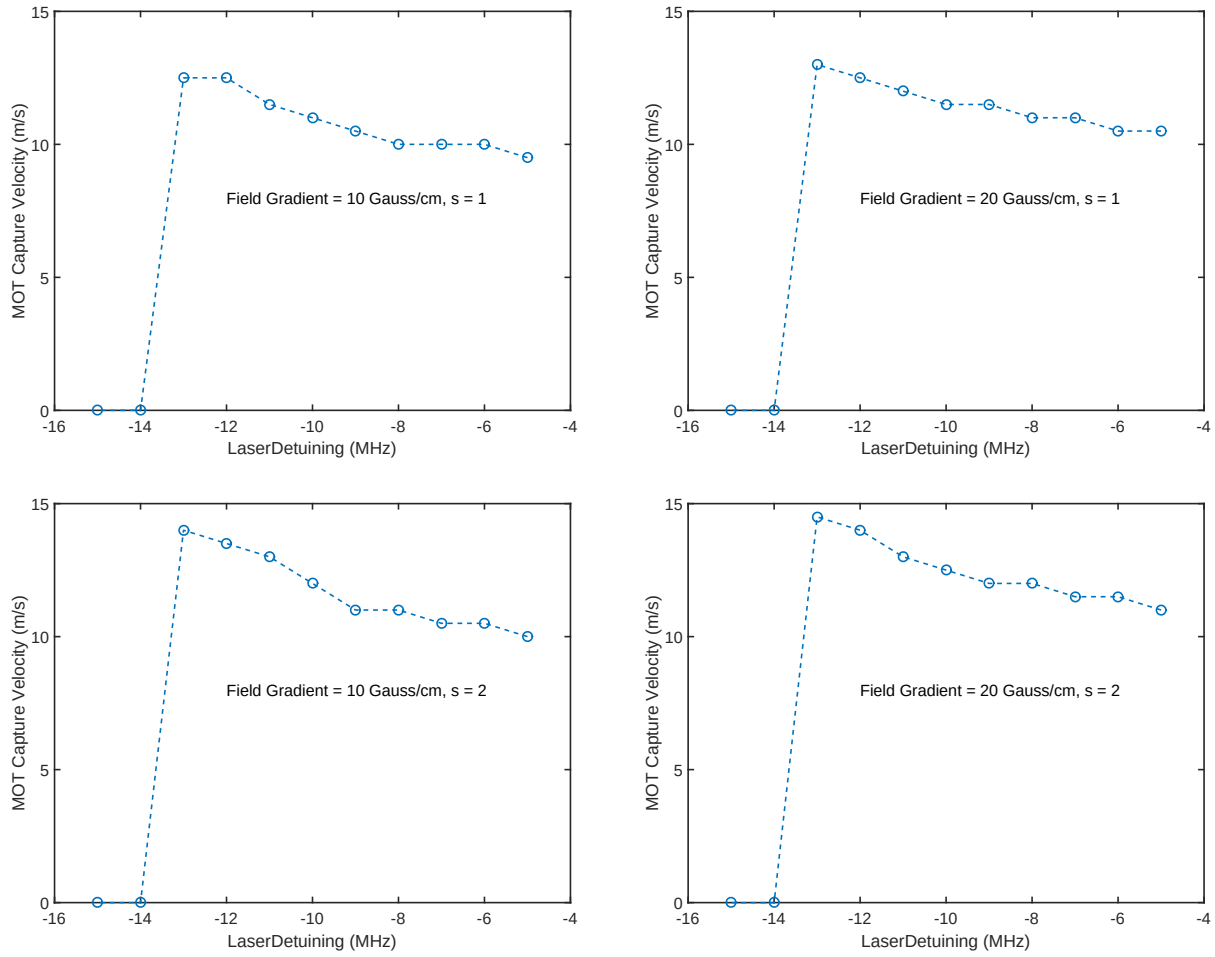

Figure 7.2.2: MOT capture velocity as a function of laser detuning δ_0. The field gradient and the saturation parameter that are used for each calculation are noted in the figures. For all field gradient and saturation parameter cases, the capture velocity is similar to the maximum value of about 13 m/s at about 13 MHz detuning.

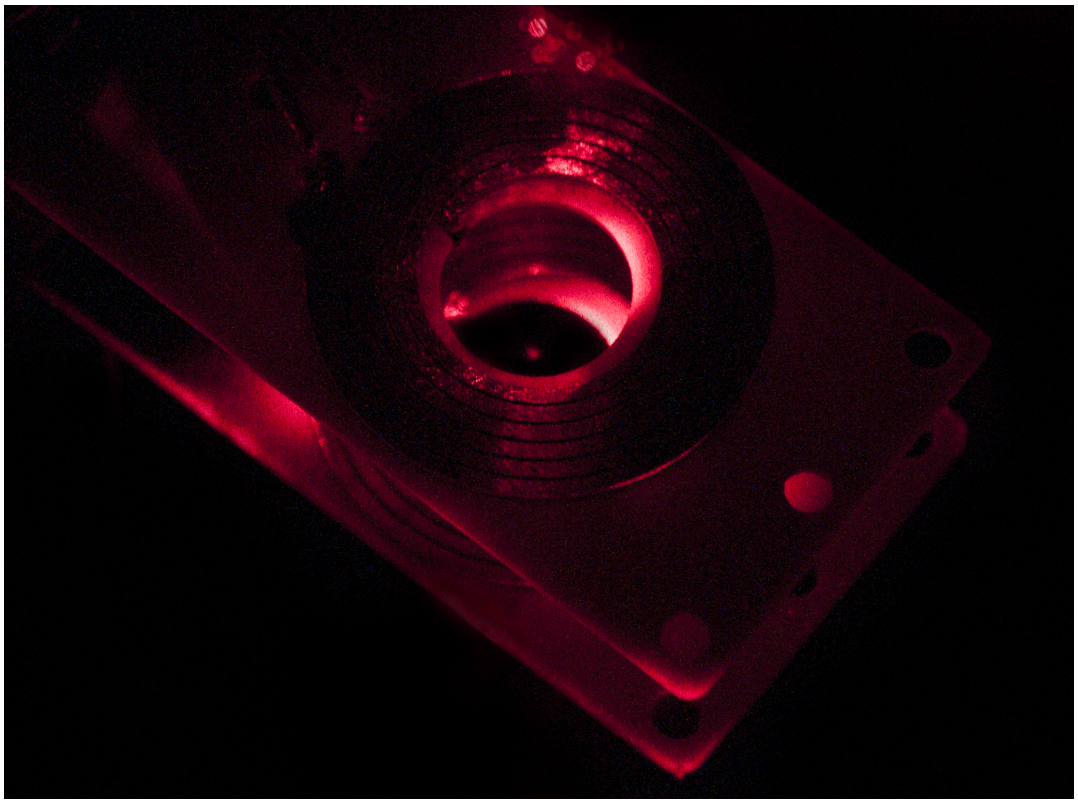

Figure 7.3.1: Photo of ^{6}Li MOT at the center of the MOT coils.

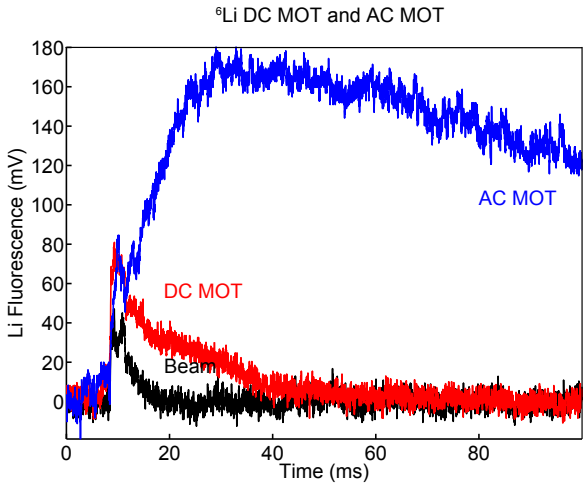

Figure 7.3.2: ^{6}Li beam (black line), DC MOT (red line), and AC MOT (blue line) comparison. The D1 transition was used to make both MOTs and all conditions were kept same except the polarization and the B field switch.

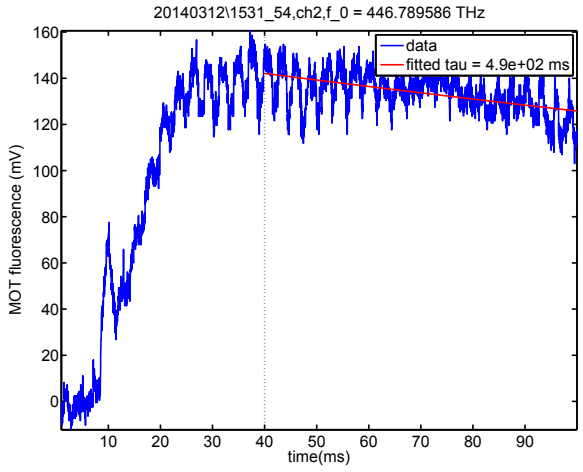

Figure 7.3.3: A timetrace of an AC MOT for ^{6}Li using D1 transition (blue line). Relevant parameters are : B field gradient = 19 Gauss/cm, buffer-gas flow = 1 sccm, YAG repetition rate = 0.56 Hz, YAG energy = 15 mJ, and AC frequency = 5.8 MHz. The data after 40 ms is fitted to an exponential decay to get the lifetime of 490 ms (red line). A sharp peak at around 10 ms is the fluorescence of the fast ^{6}Li atoms ($\sim$100 m/s) passing through the MOT chamber.

field gradient, buffer-gas flow of 1 sccm, YAG energy of 15 mJ, YAG repetition rate of 0.56 Hz, and AC frequency of 5.8 MHz. The slowing laser was broadened with $\sim$300 mW input RF drive power by the white-light EOM with total optical power of 30 mW. The fitted lifetime of the AC MOT was 490 ms but more data at later times are needed to fit more accurately. The expected lifetime of the MOT is $\sim$1 s from the background pressure near the MOT, but the cold He gas may reduce the lifetime of the MOT as well. The FWHM linewidth of the MOT signal was 13 MHz ($\sim 2\gamma$).

Fig. 7.3.5 shows the number of atoms in the AC MOT and the lifetime of the AC MOT as a function of buffer-gas flow. More atoms come out from the cell with higher buffer-gas flow but the forward velocity also increases with the flow. These two compete with each other and as a result, we expect to have an optimal flow rate for maximum number of atoms loaded into the AC MOT. With the experimental parameters we had, buffer-gas flow of 1 sccm gave us the most number of atoms in the trap. Higher buffer-gas flow results in worse vacuum in the MOT chamber and shortens the lifetime of the MOT.

From the saturation parameter of 2 and the transition properties, the acceleration from

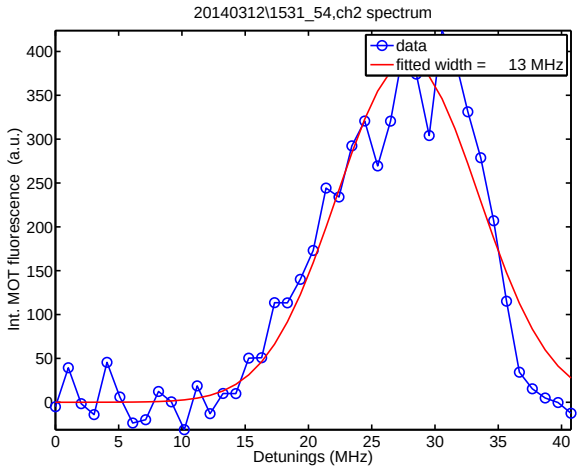

Figure 7.3.4: Frequency scan over the AC MOT transition. Horizontal axis is the detuning from the resonance of the transition. Positive values indicate red-detuning.

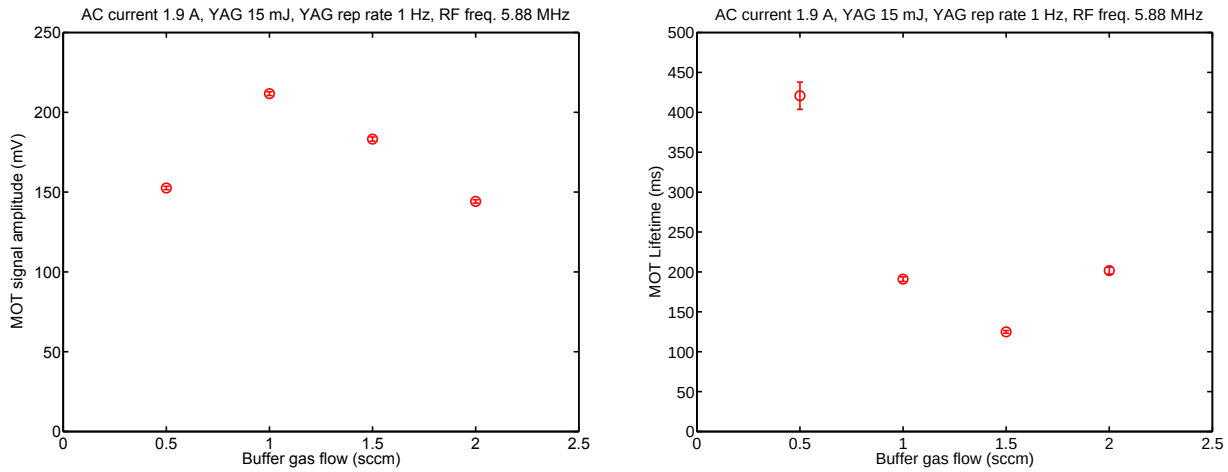

Figure 7.3.5: The number of atoms in the AC MOT (leftside) and the lifetime of the MOT (rightside) as a function of buffer-gas flow. The errorbar indicates the statistical errorbar from the fit. The atomic number fluctuation due to the ablation is bigger than the statistical errorbar.

the laser a is 1×10^6 m/s^2. Combined with the $r_c = 0.5$ cm, the capture velocity is estimated as $v_c \sim 70$ m/s using Eq. 7.1.1. This capture velocity could be achieved with a magnetic field gradient of

$$\begin{aligned} \frac{dB}{dz} &= \frac{\hbar k v_c}{\mu r_c} \\ &\sim 150 \text{ Gauss/cm} \end{aligned} \tag{7.3.1}$$

[90]. Our magnetic field gradient is much smaller than this, < 20 Gauss/cm, and in this regime, we expect the capture velocity increase linearly with the magnetic field gradient

$$v_c = \frac{\mu r_c}{\hbar k} \frac{dB}{dz} \tag{7.3.2}$$

. With the field gradient of 10 Gauss/cm , the capture velocity would become $\sim$5 m/s. Fig. 7.3.6 shows that the number of trapped atoms increased as we applied higher field gradient, indicating the increase of the capture velocity. We didn't see a dramatic dependence of the MOT lifetime on the magnetic field gradient, except the one with 5 Gauss/cm where there weren't enough number of atoms in the trap to fit the decay properly.

The next parameter we varied was the repetition rate of the YAG laser, which generates the atoms in the cell. The YAG laser is one of the main source of heating of the cell and we have seen less number of atoms or molecules out of the cell with high repetition rate, which might lead to a smaller number of atoms in the trap. Nevertheless, we didn't see an obvious dependency on the YAG repetition rate for both the number of atoms in the trap and the lifetime.

Lastly, the dependence of the MOT properties on the AC switching frequency was studied. We couldn't see any definite tendency either. Several groups have studied the effect of the switching frequency on the photon scattering rate in the ion trap [80, 95] and they concluded that the scattering rate would be quite constant across the regime where the switching frequency is from $\sim$0.1 γ to $\sim$1 γ, where γ is the natural linewidth of the excited state. This

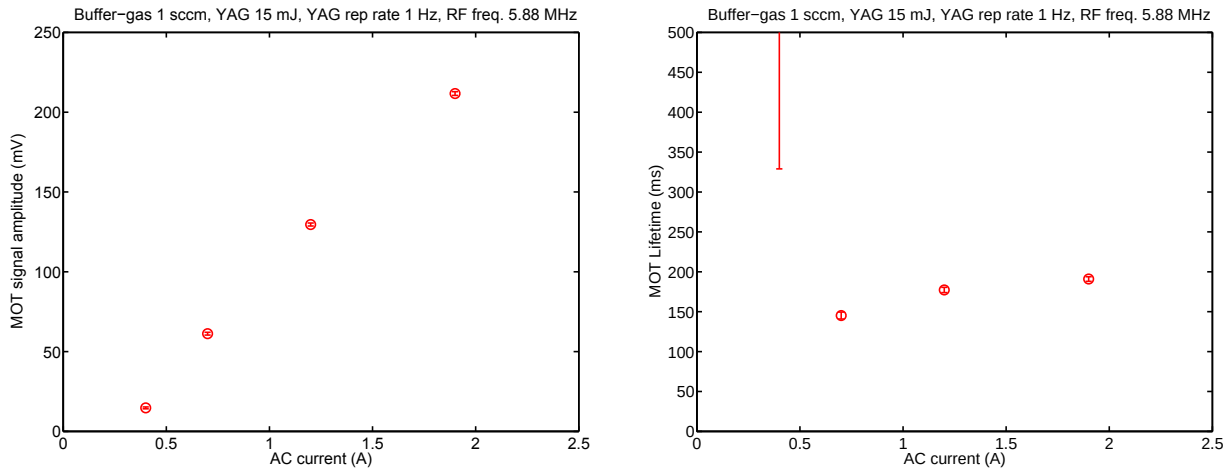

Figure 7.3.6: The number of atoms in the AC MOT (leftside) and the lifetime of the MOT (rightside) as a function of MOT field gradient. 1 Amp current corresponds to 10 Gauss/cm. The errorbar indicates the statistical errorbar from the fit. The atomic number fluctuation due to the ablation is bigger than the statistical errorbar.

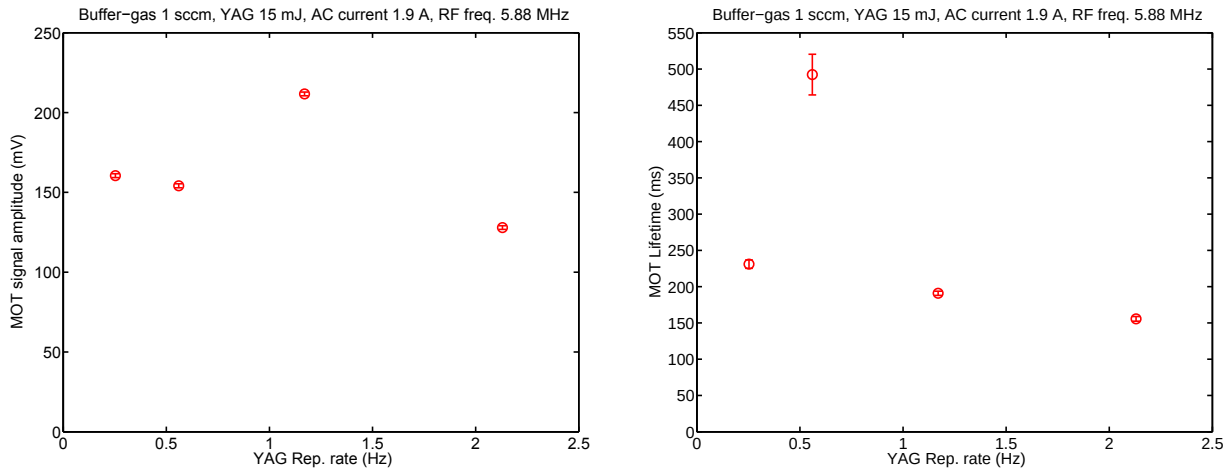

Figure 7.3.7: The number of atoms in the AC MOT (leftside) and the lifetime of the MOT (rightside) as a function of YAG repetition rate. The errorbar indicates the statistical errorbar from the fit. The atomic number fluctuation due to the ablation is bigger than the statistical errorbar.

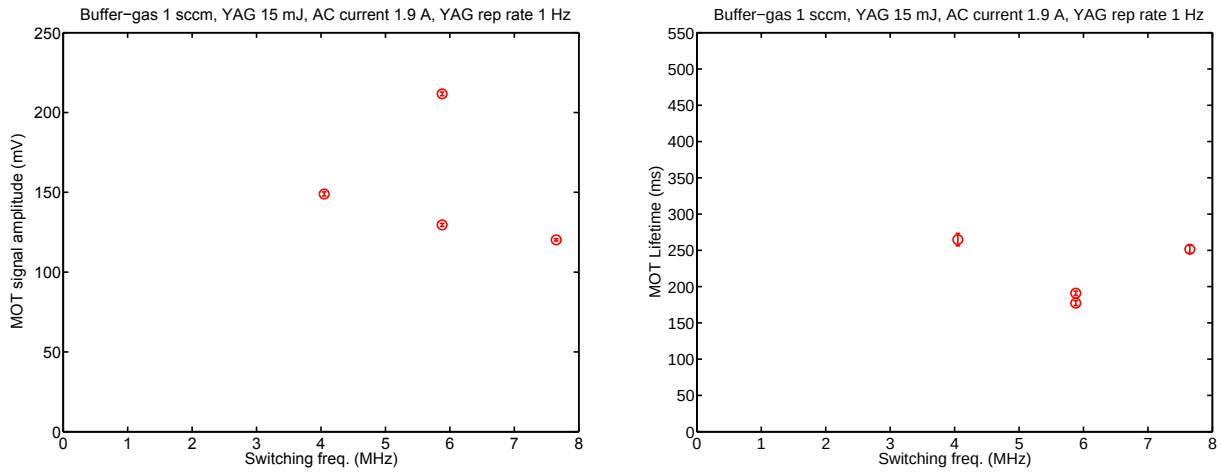

Figure 7.3.8: The number of atoms in the AC MOT (leftside) and the lifetime of the MOT (rightside) as a function of RF frequency of the MOT. The errorbar indicates the statistical errorbar from the fit. The atomic number fluctuation due to the ablation is bigger than the statistical errorbar, which one can see from MOT signal amplitude plot.

is consistent with the recent SrF MOT measurement on the scattering rate as a function of switching frequency [59]. However, the scattering rate does not tell you if the atoms or molecules scattered the trapping photons or the anti-trapping photons. Even with the same scattering rate, if the particles scatters nearly equal number of the anti-trapping photons to the trapping photons, it would not form a trap. This explains why the SrF AC MOT had similar scattering rates with different switching frequencies, yet the number of trapped molecules got increased with faster switching frequency. In this experiment, the switching frequencies we tried were $> 0.67\ \gamma$ and we needed lower switching frequencies to start seeing these effects.

7.3.1 Estimation of the number of atoms in the AC MOT

The necessary parameters to calculate the number of atoms in the trap are as follows.

- PMT gain $= 2.954\times10^{20}\times V_{High}{}^{9.028}$ ($V_{high} = V_{ctrl}\times 250$ (V), V_{high}(high voltage between the anode and the cathode of the PMT), V_{ctrl}(control voltage) $= 1.64$ (V))
- Preamplifier SR570 gain $= 1\times10^{6}$ (V/A)

- PMT sensitivity at 671 nm = 0.5 (mA/W)
- Collection efficiency of the optics from geometry = 0.003
- Energy of one λ =671 nm photon = $h\,c/\lambda$ (J)
- Maximum scattering rate = $\gamma/2$ (s^{-1}), $\gamma = 2\pi \times 5.9$ MHz

From these parameters, a signal of 100 mV on the PMT corresponds to 1×10^6 ^{6}Li atoms and the maximum number of atoms we loaded into the MOT is $\sim 2.1 \times 10^6$.

7.4 Progress towards an AC MOT for CaF

7.4.1 AOM setup for hyperfine splittings of MOT transition

For slowing, we used one EOM to imprint several sidebands with 25 MHz separation to address all the hyperfine states in the electronic ground states of CaF since the polarization of slowing laser doesn't matter. However, the polarization is the key feature of the MOT and we need to take care of it seriously. One of the hyperfine states ($J = 1/2$, $F = 1$) has opposite sign of the g_F factor (Table 7.1) and requires opposite polarization to the others for a MOT. The SrF experiment used an EOM to generate all the hyperfine lines with the same polarization first, and then put one more laser with the opposite polarization for the state with the negative g_F factor to compensate [57]. Unfortunately, we cannot use the same trick since we would need one more dye laser or an OPO-SFG laser to do that. Instead, we chose to use multiple AOMs to imprint sidebands so that we have independent polarization control for all the hyperfine sidebands.

Fig. 7.4.1 depicts the overall setup. There are three AOMs who produce a -1st or 1st order sideband so that there are four frequencies in the end including the 0th order for the four hyperfine states. Thanks to the individual tunability of each AOM's frequency, we can exactly match the hyperfine splittings where there are slight mismatch with the EOM. All

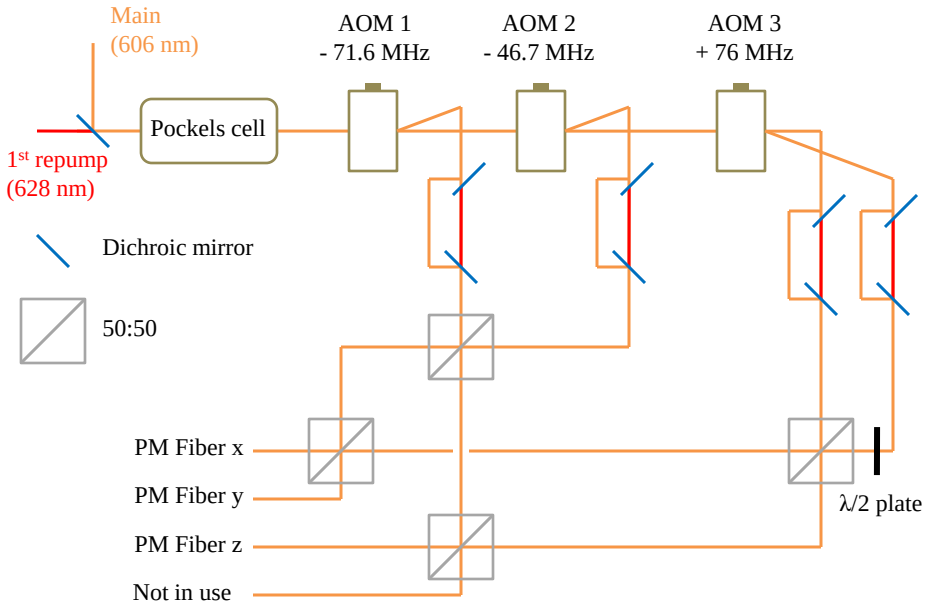

Figure 7.4.1: Hyperfine AOM setup.

the sidebands and the 0th order light are combined using a 50:50 non-polarizing beam splitter and coupled to polarization maintaining single-mode fibers. The sideband for $J = 1/2$, $F = 1$ state (+76 MHz sideband) passes a $\lambda/2$ plate and has the opposite polarization with respect to the others. The Pockels cell for polarization switching is placed at the input of the AOM setup so that all the beams share same polarization switching. The main MOT laser (606 nm) and the 1st repump laser (628 nm) are combined using a dichroic mirror before the Pockels cell. Due to the difference in the wavelength of the two colors, the 1st (or the -1st) order AOM sidebands of the two lasers come out at slightly different angle. This hinders good fiber-coupling for both colors and we again divide the each two colors after the AOMs so that we can couple all the colors more efficiently.

7.4.2 Reducing back-ground scattering - blackening the chamber

We expect to capture around 1000 molecules in the MOT with current setup. To see a MOT with such a low number of molecules, we need to cut down every possible back-ground light

source inside our chamber. The white MOT coils assembly inside the chamber lights up beautifully, but awfully for the experiment, by the total power of ∼500 mW of orange and red MOT beams, the shiny MOT chamber lets the photons bounce around the area. We blackened everything possible inside the chamber to reduce the background photons.

Each MOT beam arm has a nipple with a blackened copper tube with the diameter of 3/4" (CPT-275-075 Copper Pinch-Off Tube from Huntington Mechanical Labs). The blackened copper tube is made by exposing it to basic solution to form a uniform porous oxide layer, which traps light inside. A detailed recipe for blackening copper can be found in Ref. [96]. We also made a copper "curtain" painted with non-conductive, UHV compatible ultra black paint (MH2200 from Alion) using air-brush around the MOT chamber to hide the shiny surface of the chamber. Finally, we painted the white MOT coil Alumina board with the same paint and oxidized the copper coil itself. We tested that the self-resonances of the coil assembly didn't change after the blackening. One can see a dramatic improvement of background scattering after the blackening in Fig. 7.4.2.

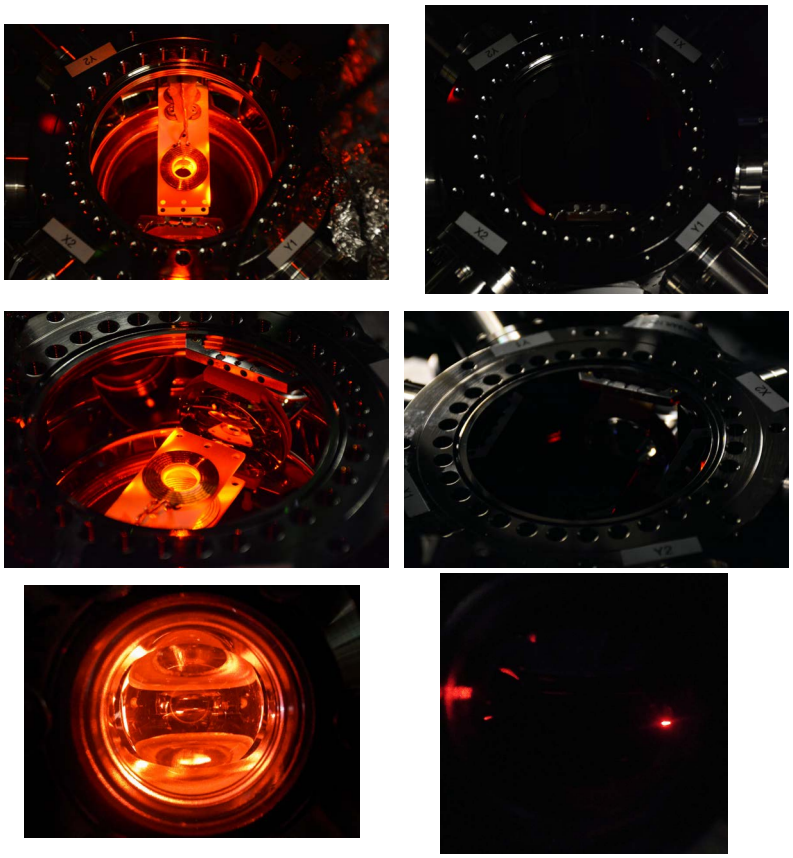

Figure 7.4.2: Photos of the MOT chamber before (leftside) and after (rightside) the blackening. The laser power, the laser alignment, and the camera exposure are kept same.

Chapter 8

Summary and outlook

8.1 AC MOT for CaF

8.1.1 Lifetime estimation

There are two straight-forward major effects that limit the lifetime of a MOT. One is background gas collisions (mostly helium at 300 K), and the other is the limited photon budget the molecules have. Background gas collisions with cold helium from the molecular beam is another possible effect, although we estimate this to be small (see Section 4.2).

When we run the experiment with 4 sccm buffer-gas flow in the chamber without the stem region, the pressure in the MOT chamber, which is 50 cm from the buffer-gas cell) is at around 2.5×10^{-7} Torr (5×10^{-8} Torr on the ion gauge that is divided by the helium gas correction factor of 0.18). The background gas limited lifetime we can estimate to be in this case, assuming the cross-section of He atoms to be 10^{-14} cm^2, about 90 ms. The SrF experiment at Yale uses 5 sccm buffer-gas flow and the pressure in the MOT chamber is reported as 2×10^{-9} Torr [57], which is factor of 10 smaller than our pressure after accounting the cell and the MOT chamber distance difference (50 cm for us, and 140 cm for the SrF experiment). A factor of 10 better vacuum would give us a MOT lifetime of ~ 900 ms, which is longer than the recent lifetime of the SrF MOT, which is 500 ms [59] with three vibrational

repump lasers. We observe the MOT lifetime to be not affected by the buffer-gas flow in linear manner for ^{6}Li MOT in our experiment. The momentum change due to the collisions with the cold buffer-gas is larger for a ^{6}Li atom than for a CaF molecules due to the mass difference. Both ^{6}Li and CaF MOT would have similar capture velocities of 5- 10 m/s from the simple estimation. Therefore we can assume that the cold helium gas wouldn't cause trap loss from the CaF MOT.

With two vibrational repump lasers, the CaF molecules can scatter about 10^5photons before they decay into the $v = 3$ state. Depending on the scattering rate, which should be from $2\pi \times 0.1$ MHz to $2\pi \times 0.5$ MHz with the power and the detuning we plan to use, the lifetime of the MOT would be 160 ms to 30 ms. This time scale should be enough to transfer the molecules from the MOT to another trap. We can easily improve the lifetime by putting the third vibrational repump laser, our photon budget increases to 10^6 photons and the expected lifetime would increase by an order of magnitude to between about 1.6 s and 300 ms.

8.1.2 $A\,^2\Pi_{1/2}$ state parity mixing due to AC MOT

Due to the fast switching (order of MHz) of the current going through the in-vacuum coils, a high voltage difference can form between the top and the bottom coils due to the coils' inductance and capacitance, which highly depends on the coil geometry. This voltage across the coils results in an electric field near the MOT center and the Yale group has seen about RMS 100 V/cm electric field at the switching frequency of 1.9 MHz [59]. This high electric field unfortunately mixes the two opposite parity states in the excited state $A\,^2\Pi_{1/2}(J = 1/2, \pm)$, which are 4 GHz apart for SrF molecules and 1.3 GHz for CaF. The mixing causes the molecules to decay to the other parity states in the ground state $X\,^2\Sigma(N = 0, 2)$ and the molecules are lost unless they are pumped or remixed back to the cycling transition. The SrF revealed the limited lifetime of about 20 ms with the switching frequency at 1.9 MHz due to this loss mechanism. Once they block the leakage to the $X\,^2\Sigma(N = 0, 2)$ states using

microwave remixing (for $N = 0$ state) and another repump laser (for $N = 2$ state), they could observe a long lifetime of 500 ms.

This voltage depends a lot on the coil geometry and material. We have a factor of few smaller coils than the Yale group and the measured voltage across the current input pin and the output pin outside of the vacuum chamber is about RMS 19.5 V at 1 MHz switching. This indicates that the voltage across the coils inside the vacuum is RMS 10 - 19.5 V, resulting the electric field of RMS 10 - 19.5 V/cm, considering the separation of the top and bottom coils are 1 cm in our setup. This is an order of magnitude smaller electric field than the SrF experiment, but the Λ doubling in the $A\,^2\Pi_{1/2}$ state of CaF is also smaller than one of SrF by about factor of 3. We need to compare the two more carefully to predict the CaF AC MOT behavior.

The excited state $A\,^2\Pi_{1/2}$ of SrF has a dipole moment of 2.064 D [97] and the Λ doubling of 4.0 GHz [98]. For CaF molecules, they are 4.1 D [99] and 1.3 GHz [74] respectively. Using the simple first order perturbation, the wavefunctions of the two opposite parity states are mixed by the amount of $\boldsymbol{d} \cdot \mathbf{E}/\Delta E$, where ΔE represents the Λ splitting energy.

$$|\tilde{+}\rangle = \frac{1}{C}\left(|+\rangle + \frac{\boldsymbol{d} \cdot \mathbf{E}}{\Delta E}|-\rangle\right) \tag{8.1.1}$$

C is the normalizing factor. The relative probability for the molecules to decay to the opposite parity states ($N = 0$, 2 states) in the ground state due to the mixing is the square of the mixed amount of the opposite parity wavefunction. From the electric field near the MOT center for each experiment, the probability is 6.7×10^{-4} for SrF with 100 V/cm electric field and $2.5 \times 10^{-4}$to 9.0×10^{-4} for CaF with 10 to 19 V/cm. From this, we can estimate the lifetime of the AC MOT for CaF without mixing of $N = 0$, 2 states would be about 50 ms to 15 ms and we should be able to detect the MOT.

We can eliminate the loss to the $N = 0$, 2 states by remixing the $X\,^2\Sigma(N = 0, 2)$ states with microwaves at 20.5 GHz (for $N = 0$ state) and 41 GHz (for $N = 2$ state). Using another

laser to repump them would be challenging due to the inconvenient wavelength of 606 nm. Microwave remixing was successfully used for laser slowing of YO molecules [53] and SrF AC MOT [59]and we expect same efficiency as them.

8.2 Dual MOTs for CaF and ^{6}Li

Once we achieve the AC MOT of CaF molecules, it would be straight forward to make a dual AC MOT for CaF molecules and ^{6}Li atoms. In the dual MOT , the light-assisted collisions between ^{6}Li atoms and CaF molecules could be studied. The inelastic light-assisted collision occurs because the inter-particle potential changes whether the two particles are both in the ground state or one is in the excited state. By observing the light-assisted collision, one can study the difference of the CaF - Li potential depending on their electronic states. If the loss is mainly from the chemical reaction in the excited state, one can implement controlling the chemical reaction by exciting the reactants.

Since the ^{6}Li AC MOT and CaF AC MOT operate at the same magnetic field gradient, all we need to do is overlapping all the lasers for CaF and ^{6}Li. Thanks to the difference in the wavelength - 606 nm and 628 nm for CaF, 671 nm for ^{6}Li -, the lasers could be overlapped using dichroic mirrors[1]. Since all the dye lasers are currently in use for CaF molecules, two new ^{6}Li lasers (one for the MOT beams and the other for the slowing beam) need to be built. A diode laser [2] and tapered amplifier [3] would give 500 mW output power, which is enough for the purpose.

[1]for example, Di02-R635-25x36 from Semrock

[2]EYP-RWE-0670-00702-1000-SOT02-0000 from eagleyard

[3]EYP-TPA-0670-00500-2003-CMT02-0000 from eagleyard

8.3 Transferring Molecules into a Conservative Trap

Once the AC MOT for CaF is made, we would like to transfer them into a conservative trap, like a magnetic trap, a microwave trap, or a dipole trap. Due to the high temperature (about 1 mK) and the large size (about a few mm) of the expected AC MOT for CaF, a magnetic trap or a microwave trap is a better approach. A CaF molecule has a magnetic moment of one Bohr magneton and the magnetic field of 10 Gauss would form about 0.67 mK deep trap from a simple estimation. Although this estimation is not accurate for every states in this weak or intermediate field regime , it is accurate for the stretched states ($F = 2$, $M_F = \pm 2$). The 20 GHz rotational transition could be used to form a trap for either the $N = 0$ state or the $N = 1$ state depending on the detuning.

The magnetic field coils for the MOT can be used as the magnetic trap coils as they are. By turning off the MOT laser beams, the molecules in the trappable states will be remained in the magnetic trap. We can use a static magnetic field which traps only the low-field seeking states, or we can try an AC magnetic field to make a time-averaged trap for all the states.

8.3.1 Static magnetic trap for low-field seeking states

As we turn off the MOT laser beams, we can stop switching the magnetic filed and load the molecules in the static magnetic field. Only the low-field seeking states can be loaded into a static anti-Helmholtz magnetic trap. Among them, the stretched $F = 2$, $M_F = 2$ state has the maximum trapping potential of 1.4 MHz/Gauss ~ 0.067 mK/Gauss (Fig. 2.2.2). To increase the number of trapped molecules and to clean other states which can introduce the spin-exchange collisions, we can optically pump all the molecules into that state by turning off the laser addressing that state before than other lasers since optical pumping takes place with only tens of photon scatterings. We can also couple the $X\,^2\Sigma(N = 1)$ states to $X\,^2\Sigma(N = 0, F = 1, M_F = 1)$ state, which is the stretched state in the rotationally

ground state. Then we can increase the static magnetic field to 50 Gauss to form a 3.3 mK deep trap.

8.3.2 Microwave trap

In Ref. [48], authors proposed a microwave trap for the absolute ground state molecules that would have no inelastic collisions except the possible chemical reactions. With reasonable experimental setup, a trap with the depth of about 1 K and the size of about 1 cm^{-3}. This is a very promising method to trap molecules. However, co-trapping molecules and atoms would require an additional trap since atoms don't see the microwave trap. One should make sure the the trap for the atoms don't destroy the molecular trap. Also the size of the molecular trap and the atomic trap should be about the same to make use of most of the trapped species.

8.3.3 Increasing the lifetime limited by the background gas

As mentioned earlier, the background-gas limited lifetime of a trap in our current setup is about 90 ms. We can build a cryo-shutter in the 4 K to block the buffer-gas after the pulse of molecules. People have used one in our group and observed 500 ms lifetime of the deep magnetic trap for CaF [36]. The situation is quite different in our case in terms of the surrounding environment (cold vs warm) and the trap depth (K vs mK), but the shutter should help to increase the lifetime of the trap in our case as well. We can also consider putting a shutter in the room temperature area, but the buffer-gas density may increase behind the shutter and lead to degradation of the molecular beam.

8.3.4 Increasing the number of molecules in the trap

The maximum number of molecules trapped in the MOT for SrF is about 2000 molecules after a lot of optimization. Inferring from the number of molecules we slowed, we also expect

similar number of CaF molecules in the MOT. This is a great starting point, but we would like to increase the number of molecules. There are two major parts that are responsible for the low number of trapped molecules - one is the low flux from the beginning, and the other is the inefficient slowing. Many ways of generating CaF molecules have been used and two methods are used in the buffer-gas source, ablation of a CaF_2 pressed target in this group and ablation of Ca metal in a SF_6 environment [100], yielding similar number of molecules in the beam. Using a different target that is denser and has many neighboring Ca and F may generate more molecules when ablated. Natural CaF_2 crystals with impurities with dark colors could be a nice test target since it is the most dense CaF_2 and could absorb a lot of energy from the YAG laser due to the dark color.

Another important part of the experiment that could be improved is the slowing. Zeeman slowing for atoms ensures that the atom is decelerated down to a certain velocity at a fixed position since the detuning is space-dependent. The spread of the atoms is therefore minimized and all the slowed atoms at that position can be trapped by placing the trap there. However, white-light slowing happens all the way along the molecules' pass and the molecules could be spread to the side or even going backwards when they receive too much deceleration. If the molecules are put to elsewhere, in space or in different rotational states, as soon as their forward velocity becomes at around 10 m/s, that would increase the number of molecules in the trap. We can use a microwave or magnetic guide for slow molecules so that they don't spread out much. By bending the guide, we can even separate the slow molecules from the remaining buffer-gas and the slowing laser. Once the trap is placed at the end of the trap, we can trap most of the molecules out of the guide and will achieve longer lifetime thanks to the better vacuum. We may be able to load the molecules multiple times if the lifetime of the trap is long enough and the next pulse of the molecules don't affect the trapped molecules.

8.4 Collisional studies

Here, the current studies about the collisions of $^2\Sigma$ molecules is summarized. The ground state of the CaF molecule is the $^2\Sigma$ state and these would give us general ideas about the collisional properties of the CaF molecules.

$^2\Sigma$ molecule + atom The collision between spin-polarized $^2\Sigma$ molecules and $S-$state atoms are investigated in Ref. [38] which would be similar to the case of CaF + ^{6}Li. Here, the authors mainly studied the case of CaH + Li. The CaH + Li $\rightarrow$ LiH + Ca reaction is exothermic by 0.67 eV and has been observed in the cold buffer-gas environment [62]. However, this reaction is forbidden when the two are spin-polarized, which is the case in a strong magnetic field, and the only inelastic collision left would be the spin-relaxation collision. The result reveals that the elastic to inelastic collisional ratio γ is > 100 in the temperature range of 10 μK to 10 mK for CaH molecules in the $X\,^2\Sigma(v = 0, N = 0)$ state, which predicts the sympathetic cooling of CaH molecules with Li atoms will be successful. However, the magnetic field used in this research for polarizing and trapping the molecules and atoms is about 0.1 T, which is a lot bigger than the field we are planning to use. The γ decreases as the magnetic field decreases and further study is needed for the weak field regime.

Lim et al. investigated the possibility of the sympathetic cooling of the CaF molecules in their absolute ground state with Li and Rb atoms [39]. Rb atoms are a promising candidate, expected to cool the molecules down to 1 μK within about 30 s. To trap the molecules in the absolute ground state, a microwave trap should be used for molecules in this case.

$^2\Sigma$ molecule + $^2\Sigma$ molecule In Ref. [101], the authors presents shielding of collisions among $^2\Sigma$ molecules using an external electric field. The repulsive dipolar energy can be engineered using an electric field so that it can form a barrier at long range to prevent molecules from going to the short-range where many inelastic/chemical collisional channels

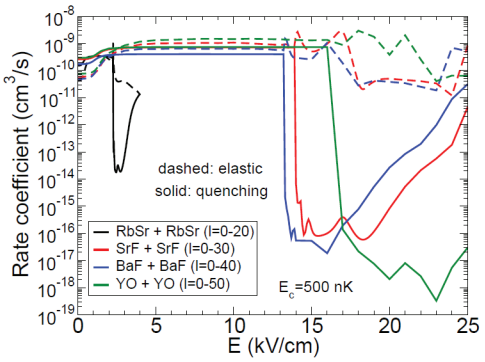

FIG. 7: (Color online) Quenching (solid lines) and elastic (dashed lines) rate coefficients of $^{84}Sr^{19}F$ + $^{84}Sr^{19}F$ (red), $^{138}Ba^{19}F$ + $^{138}Ba^{19}F$ (blue) and $^{89}Y^{16}O$ + $^{89}Y^{16}O$ (green) collisions as a function of the electric field, for a fixed collisions energy of $E_c = 500$ nK. The range of partial waves is respectively $l = 0-30$, $l = 0-40$, $l = 0-50$. The curve from Fig. 5 for RbSr has been added for comparison.

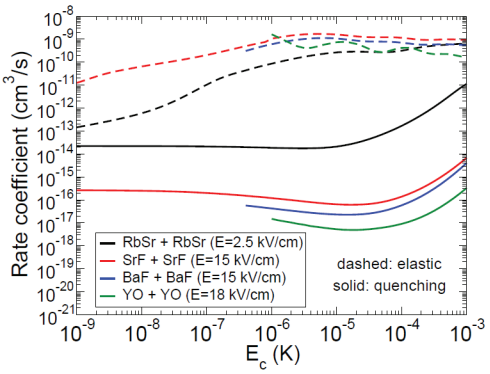

FIG. 8: (Color online) Same as Fig. 7 but as a function of the collision energy for a fixed electric field of $E = 15$ kV/cm for the SrF and BaF molecules, and $E = 18$ kV/cm for the YO molecules. The curve from Fig. 6 for RbSr has been added for comparison.

Figure 8.4.1: Calculated collision rate for various $^2\Sigma$ molecules. Figure take from Ref. [101].

exist. With an electric field about 15 - 18 kV/cm, they showed that the elastic to inelastic collisional ratio γ is > 10000 in the collisional energy range of 1 μK - 1 mK for SrF, BaF, and YO in the $X\,^2\Sigma(v = 0, N = 1)$ state. One needs to make sure that the electric field doesn't harm the trap for the molecules.

Appendix A

Transforming Hund's case (b) to Hund's case (a)

Following Mol. Phys. 31, 1517 (1976) by J. M. Brown and B. J. Howard.

- step (1) : Decouple rotation N and spin S

$$|\Lambda, N, S, J, M_J\rangle = \sum_{M_N\, M_S} (-1)^{-N+S-M_J} \sqrt{2J+1} \times \begin{pmatrix} N & S & J \\ M_N & M_S & -M \end{pmatrix} |\Lambda, N, M_N, S, M_S\rangle \tag{A.0.1}$$

- step (2) : replace $|N\, M_N\, \Lambda\rangle$and $|S\, M_S\rangle$ using below

$$|N, (\Lambda), M_N\rangle = \sqrt{\frac{2N+1}{8\pi^2}} D^{(N)}_{M_N\,\Lambda}(\omega)^* \tag{A.0.2}$$

$$|S, M_S\rangle = \sum_{\Sigma} D^{(S)}_{M_s\,\Sigma}(\omega)^*\, |S, \Sigma\rangle\,. \tag{A.0.3}$$

and then (**??**) becomes

$$|\Lambda, N, S, J, M_J\rangle = \sum_{M_N\, M_S\, \Sigma} |\Lambda, S, \Sigma\rangle\, (-1)^{-N+S-M_J}\, \sqrt{2J+1}\sqrt{\frac{2N+1}{8\pi^2}} \times \begin{pmatrix} N & S & J \\ M_N & M_S & -M \end{pmatrix} D^{(N)}_{M_N\,\Lambda}(\omega)^* D^{(S)}_{M_S\,\Sigma}(\omega)^* \quad \text{(A.0.4)}$$

We insert $1 = \int d\omega \sum_{J'M'\Omega'} |J', \Omega', M'_J\rangle \langle J', \Omega', M'_J|$ and use

$$\langle J', \Omega', M'_J| = \sqrt{\frac{2J'+1}{8\pi^2}} D^{(J')}_{M'_J\,\Omega'}(\omega) \quad \text{(A.0.5)}$$

to get

$$|\Lambda, N, S, J, M_J\rangle = \int d\omega \sum_{M_N\, M_S\, \Sigma} \sum_{J'\, M'_J\, \Omega} |\Lambda, S, \Sigma, J', \Omega', M'_J\rangle\, (-1)^{-N+S-M_J}\, \sqrt{2N+1} \times \begin{pmatrix} N & S & J \\ M_N & M_S & -M \end{pmatrix} \frac{\sqrt{(2J+1)(2J'+1)}}{8\pi^2} \times D^{(N)}_{M_N\,\Lambda}(\omega)^* D^{(S)}_{M_S\,\Sigma}(\omega)^* D^{(J)}_{M_J\,\Omega}(\omega). \quad \text{(A.0.6)}$$

From Parker (B42)

$$\int d\omega D^{(N)}_{M_N\,\Lambda}(\omega)^* D^{(S)}_{M_S\,\Sigma}(\omega)^* D^{(J')}_{M'_J\,\Omega'}(\omega) = 8\pi^2 (-1)^{N-S+\Omega'} \begin{pmatrix} N & S & J' \\ \Lambda & \Sigma & -\Omega' \end{pmatrix} \cdot \times (-1)^{N-S+M'_J} \begin{pmatrix} N & S & J' \\ M_N & M_s & -M'_J \end{pmatrix} \quad \text{(A.0.7)}$$

Therefore,

$$
\begin{aligned}
|\Lambda, N, S, J, M_J\rangle &= \sum_{M_N\, M_S\, \Sigma\, J'\, M'_J\, \Omega} |\Lambda, S, \Sigma, J', \Omega', M'_J\rangle\, (-1)^{N-S-M_J+\Omega+M'_J} \\
&\quad \times\sqrt{(2N+1)(2J+1)(2J'+1)} \begin{pmatrix} N & S & J \\ M_N & M_S & -M \end{pmatrix}. \\
&\quad \times \begin{pmatrix} N & S & J' \\ \Lambda & \Sigma & -\Omega' \end{pmatrix} \begin{pmatrix} N & S & J' \\ M_N & M_s & -M'_J \end{pmatrix} \qquad \text{(A.0.8)}
\end{aligned}
$$

3j symbol has a following property (orthogonality).

$$
\sum_{M_N M_S} \begin{pmatrix} N & S & J \\ M_N & M_s & -M_J \end{pmatrix} \begin{pmatrix} N & S & J' \\ M_N & M_s & -M'_J \end{pmatrix} = \frac{1}{2J+1} \delta_{J'J} \delta_{M'_J M_J} \qquad \text{(A.0.9)}
$$

As a result, (substituting Ω' to Ω),

$$
\begin{aligned}
|\Lambda, N, S, J, M_J\rangle &= \sum_{\Sigma} \sum_{\Omega} |\Lambda, S, \Sigma, J, \Omega, M_J\rangle\, (-1)^{N-S+\Omega} \\
&\quad \times\sqrt{2N+1} \begin{pmatrix} N & S & J \\ \Lambda & \Sigma & -\Omega \end{pmatrix}. \qquad \text{(A.0.10)}
\end{aligned}
$$

Appendix B

Eigenstates of the electronic ground state X of CaF

Here, the eigenstates of the electronic ground state X of a CaF molecule are ordered by energy, from high to low. We use constants from Ref. [73], ignoring the high order terms for rotational state change ($B = 10267.46$ MHz, $\gamma = 39.49809$ MHz, $b = 108.4764$ MHz, $c = 39.5899$ MHz for the below calculation, normalized by Mathematica default precision).To name the eigenstates, we use the closest pure states and put ˜ to indicate that these are not real pure states.

$$
\begin{aligned}
\left|N=3, J=\widetilde{\frac{5}{2}}, F=2, M_F=2\right\rangle &= |\Lambda=0, N=3, J=5/2, F=2, M_F=2\rangle \\
&\quad +0.0000945435\,|\Lambda=0, N=1, J=3/2, F=2, M_F=2\rangle \\
\left|N=3, J=\widetilde{\frac{5}{2}}, F=2, M_F=1\right\rangle &= |\Lambda=0, N=3, J=5/2, F=2, M_F=1\rangle \\
&\quad +0.0000945435\,|\Lambda=0, N=1, J=3/2, F=2, M_F=1\rangle \\
\left|N=3, J=\widetilde{\frac{5}{2}}, F=2, M_F=0\right\rangle &= |\Lambda=0, N=3, J=5/2, F=2, M_F=0\rangle \\
&\quad +0.0000945435\,|\Lambda=0, N=1, J=3/2, F=2, M_F=0\rangle \\
\left|N=3, J=\widetilde{\frac{5}{2}}, F=2, M_F=-1\right\rangle &= |\Lambda=0, N=3, J=5/2, F=2, M_F=-1\rangle \\
&\quad +0.0000945435\,|\Lambda=0, N=1, J=3/2, F=2, M_F=-1\rangle
\end{aligned}
$$

$$
\begin{aligned}
\left|N=3, J=\widetilde{\frac{5}{2}}, F=2, M_F=-2\right\rangle &= |\Lambda=0, N=3, J=5/2, F=2, M_F=-2\rangle \\
&\quad +0.0000945435\,|\Lambda=0, N=1, J=3/2, F=2, M_F=-2\rangle \\
\left|N=2, J=\widetilde{\frac{5}{2}}, F=2, M_F=2\right\rangle &= -0.906567\,|\Lambda=0, N=2, J=5/2, F=2, M_F=2\rangle \\
&\quad +0.422062\,|\Lambda=0, N=2, J=3/2, F=2, M_F=2\rangle \\
\left|N=2, J=\widetilde{\frac{5}{2}}, F=2, M_F=1\right\rangle &= -0.906567\,|\Lambda=0, N=2, J=5/2, F=2, M_F=1\rangle \\
&\quad +0.422062\,|\Lambda=0, N=2, J=3/2, F=2, M_F=1\rangle \\
\left|N=2, J=\widetilde{\frac{5}{2}}, F=2, M_F=0\right\rangle &= -0.906567\,|\Lambda=0, N=2, J=5/2, F=2, M_F=0\rangle \\
&\quad +0.422062\,|\Lambda=0, N=2, J=3/2, F=2, M_F=0\rangle \\
\left|N=2, J=\widetilde{\frac{5}{2}}, F=2, M_F=-1\right\rangle &= -0.906567\,|\Lambda=0, N=2, J=5/2, F=2, M_F=-1\rangle \\
&\quad +0.422062\,|\Lambda=0, N=2, J=3/2, F=2, M_F=-1\rangle \\
\left|N=2, J=\widetilde{\frac{5}{2}}, F=2, M_F=-2\right\rangle &= -0.906567\,|\Lambda=0, N=2, J=5/2, F=2, M_F=-2\rangle \\
&\quad +0.422062\,|\Lambda=0, N=2, J=3/2, F=2, M_F=-2\rangle \\
\left|N=2, J=\widetilde{\frac{3}{2}}, F=1, M_F=1\right\rangle &= |\Lambda=0, N=2, J=3/2, F=1, M_F=1\rangle \\
&\quad +0.000151635\,|\Lambda=0, N=0, J=1/2, F=1, M_F=1\rangle \\
\left|N=2, J=\widetilde{\frac{3}{2}}, F=1, M_F=0\right\rangle &= |\Lambda=0, N=2, J=3/2, F=1, M_F=0\rangle \\
&\quad +0.000151635\,|\Lambda=0, N=0, J=1/2, F=1, M_F=0\rangle \\
\left|N=2, J=\widetilde{\frac{3}{2}}, F=1, M_F=-1\right\rangle &= |\Lambda=0, N=2, J=3/2, F=1, M_F=-1\rangle \\
&\quad +0.000151635\,|\Lambda=0, N=0, J=1/2, F=1, M_F=-1\rangle \\
\left|N=2, J=\widetilde{\frac{3}{2}}, F=2, M_F=2\right\rangle &= 0.906567\,|\Lambda=0, N=2, J=3/2, F=2, M_F=2\rangle \\
&\quad +0.422062\,|\Lambda=0, N=2, J=5/2, F=2, M_F=2\rangle \\
\left|N=2, J=\widetilde{\frac{3}{2}}, F=2, M_F=1\right\rangle &= 0.906567\,|\Lambda=0, N=2, J=3/2, F=2, M_F=1\rangle \\
&\quad +0.422062\,|\Lambda=0, N=2, J=5/2, F=2, M_F=1\rangle \\
\left|N=2, J=\widetilde{\frac{3}{2}}, F=2, M_F=0\right\rangle &= 0.906567\,|\Lambda=0, N=2, J=3/2, F=2, M_F=0\rangle \\
&\quad +0.422062\,|\Lambda=0, N=2, J=5/2, F=2, M_F=0\rangle \\
\left|N=2, J=\widetilde{\frac{3}{2}}, F=2, M_F=-1\right\rangle &= 0.906567\,|\Lambda=0, N=2, J=3/2, F=2, M_F=-1\rangle \\
&\quad +0.422062\,|\Lambda=0, N=2, J=5/2, F=2, M_F=-1\rangle \\
\left|N=2, J=\widetilde{\frac{3}{2}}, F=2, M_F=-2\right\rangle &= 0.906567\,|\Lambda=0, N=2, J=3/2, F=2, M_F=-2\rangle
\end{aligned}
$$

$$
\begin{aligned}
& & & +0.422062\,|\Lambda=0,N=2,J=5/2,F=2,M_F=-2\rangle \\
\left|N=1,J=\widetilde{\frac{3}{2}},F=2,M_F=2\right\rangle &=& & |\Lambda=0,N=1,J=3/2,F=2,M_F=2\rangle \\
& & & -0.0000945435\,|\Lambda=0,N=3,J=5/2,F=2,M_F=2\rangle \\
\left|N=1,J=\widetilde{\frac{3}{2}},F=2,M_F=1\right\rangle &=& & |\Lambda=0,N=1,J=3/2,F=2,M_F=1\rangle \\
& & & -0.0000945435\,|\Lambda=0,N=3,J=5/2,F=2,M_F=1\rangle \\
\left|N=1,J=\widetilde{\frac{3}{2}},F=2,M_F=0\right\rangle &=& & |\Lambda=0,N=1,J=3/2,F=2,M_F=0\rangle \\
& & & -0.0000945435\,|\Lambda=0,N=3,J=5/2,F=2,M_F=0\rangle \\
\left|N=1,J=\widetilde{\frac{3}{2}},F=2,M_F=-1\right\rangle &=& & |\Lambda=0,N=1,J=3/2,F=2,M_F=-1\rangle \\
& & & -0.0000945435\,|\Lambda=0,N=3,J=5/2,F=2,M_F=-1\rangle \\
\left|N=1,J=\widetilde{\frac{3}{2}},F=2,M_F=-2\right\rangle &=& & |\Lambda=0,N=1,J=3/2,F=2,M_F=-2\rangle \\
& & & -0.0000945435\,|\Lambda=0,N=3,J=5/2,F=2,M_F=-2\rangle \\
\left|N=1,J=\widetilde{\frac{3}{2}},F=1,M_F=1\right\rangle &=& & -0.772496\,|\Lambda=0,N=1,J=3/2,F=1,M_F=1\rangle \\
& & & +0.63502\,|\Lambda=0,N=1,J=1/2,F=1,M_F=1\rangle \\
\left|N=1,J=\widetilde{\frac{3}{2}},F=1,M_F=0\right\rangle &=& & -0.772496\,|\Lambda=0,N=1,J=3/2,F=1,M_F=0\rangle \\
& & & +0.63502\,|\Lambda=0,N=1,J=1/2,F=1,M_F=0\rangle \\
\left|N=1,J=\widetilde{\frac{3}{2}},F=1,M_F=-1\right\rangle &=& & -0.772496\,|\Lambda=0,N=1,J=3/2,F=1,M_F=-1\rangle \\
& & & +0.63502\,|\Lambda=0,N=1,J=1/2,F=1,M_F=-1\rangle \\
\left|N=1,J=\widetilde{\frac{1}{2}},F=0,M_F=0\right\rangle &=& & |\Lambda=0,N=1,J=1/2,F=0,M_F=0\rangle \\
\left|N=1,J=\widetilde{\frac{1}{2}},F=1,M_F=1\right\rangle &=& & 0.772496\,|\Lambda=0,N=1,J=1/2,F=1,M_F=1\rangle \\
& & & +0.63502\,|\Lambda=0,N=1,J=3/2,F=1,M_F=1\rangle \\
\left|N=1,J=\widetilde{\frac{1}{2}},F=1,M_F=0\right\rangle &=& & 0.772496\,|\Lambda=0,N=1,J=1/2,F=1,M_F=0\rangle \\
& & & +0.63502\,|\Lambda=0,N=1,J=3/2,F=1,M_F=0\rangle \\
\left|N=1,J=\widetilde{\frac{1}{2}},F=1,M_F=-1\right\rangle &=& & 0.772496\,|\Lambda=0,N=1,J=1/2,F=1,M_F=-1\rangle \\
& & & +0.63502\,|\Lambda=0,N=1,J=3/2,F=1,M_F=-1\rangle \\
\left|N=0,J=\widetilde{\frac{1}{2}},F=1,M_F=1\right\rangle &=& & |\Lambda=0,N=0,J=1/2,F=1,M_F=1\rangle \\
& & & -0.000151635\,|\Lambda=0,N=2,J=3/2,F=1,M_F=1\rangle
\end{aligned}
$$

$$\left|N=0, J=\widetilde{\frac{1}{2}}, F=1, M_F=0\right\rangle = |\Lambda=0, N=0, J=1/2, F=1, M_F=0\rangle$$
$$-0.000151635\,|\Lambda=0, N=2, J=3/2, F=1, M_F=0\rangle$$
$$\left|N=0, J=\widetilde{\frac{1}{2}}, F=1, M_F=-1\right\rangle = |\Lambda=0, N=0, J=1/2, F=1, M_F=-1\rangle$$
$$-0.000151635\,|\Lambda=0, N=2, J=3/2, F=1, M_F=-1\rangle$$
$$\left|N=0, J=\widetilde{\frac{1}{2}}, F=0, M_F=0\right\rangle = |\Lambda=0, N=0, J=1/2, F=0, M_F=0\rangle$$

Appendix C

Mathmatica Code for Branching Ratio Calculation

The relevant codes are

- CaF_Branching_Ratio_Quantum.nb : main note
- CaFXstateFullHamiltonian_Quantum.nb : calculate eigenstates of CaF X state full Hamiltonian in Hund's case (b) basis
- HundsCaseBtoA_Quantum.nb : transform Hund's case (b) basis to Hund's case (a) basis
- CaFAstateEigenstates_Quantum.nb : eigenstates of CaF A state in Hund's case (a) basis
- ElectricDipoleOperatorMatrix_HundsA_Quantum.nb : calculate ratios of matrix elements of electric dipole operator in Hund's case (a) basis.

To run these codes, one needs to install 'Quantum package' of Mathematica first. This package in the folder 'Mathematica_Quantum_Toolbox' under the 'Branching Ratio' folder. One needs to copy this folder to the 'application' folder of your Mathematica directory and

change the folder's name to 'Quantum'. For more information, please read 'Mathematica_Quantum_Toolbox/Documentation/English/installation.nb'.

Open 'CaF_Branching_Ratio_Quantum.nb' and follow comments there and run relevant codes.

Bibliography

[1] K. Davis, M. Mewes, M. Andrews, N. van Druten, D. Durfee, D. Kurn, and W. Ketterle, Physical Review Letters **75**, 3969 (1995).

[2] M. H. Anderson, J. R. Ensher, M. R. Matthews, C. E. Wieman, and E. A. Cornell, Science (New York, N.Y.) **269**, 198 (1995).

[3] I. Bloch, J. Dalibard, and S. Nascimbène, Nature Physics **8**, 267 (2012).

[4] S. Braun, J. P. Ronzheimer, M. Schreiber, S. S. Hodgman, T. Rom, I. Bloch, and U. Schneider, Science **339**, 52 (2013).

[5] M. Saffman, T. G. Walker, and K. Mølmer, Reviews of Modern Physics **82**, 2313 (2010).

[6] A. D. Ludlow, M. M. Boyd, J. Ye, E. Peik, and P. O. Schmidt, Reviews of Modern Physics **87**, 637 (2015).

[7] C. Chin, R. Grimm, P. Julienne, and E. Tiesinga, Reviews of Modern Physics **82**, 1225 (2010).

[8] L. Tarruell, D. Greif, T. Uehlinger, G. Jotzu, and T. Esslinger, Nature **483**, 302 (2012).

[9] M. Aidelsburger, M. Atala, M. Lohse, J. T. Barreiro, B. Paredes, and I. Bloch, Physical Review Letters **111**, 185301 (2013).

[10] G.-B. Jo, J. Guzman, C. K. Thomas, P. Hosur, A. Vishwanath, and D. M. Stamper-Kurn, Physical Review Letters **108**, 045305 (2012).

[11] J. R. Abo-Shaeer, C. Raman, J. M. Vogels, and W. Ketterle, Science **292**, 476 (2001).

[12] M. Lu, N. Q. Burdick, and B. L. Lev, Physical Review Letters **108**, 215301 (2012).

[13] K. Aikawa, S. Baier, A. Frisch, M. Mark, C. Ravensbergen, and F. Ferlaino, Science **345**, 1484 (2014).

[14] L. D. Carr, D. DeMille, R. V. Krems, and J. Ye, New Journal of Physics **11**, 55049 (2009).

[15] M. a. Baranov, M. Dalmonte, G. Pupillo, and P. Zoller, Chemical reviews **112**, 5012 (2012).

[16] H. P. Buchler, E. Demler, M. Lukin, A. Micheli, N. Prokofev, G. Pupillo, and P. Zoller, Physical Review Letters **98**, 060404 (2007).

[17] A. Micheli, G. Brennen, and P. Zoller, Nature Physics **2**, 341 (2006).

[18] A. André, D. DeMille, J. Doyle, M. Lukin, S. Maxwell, P. Rabl, R. Schoelkopf, and P. Zoller, Nature Physics **2**, 636 (2006).

[19] D. DeMille, Physical Review Letters **88**, 67901 (2002).

[20] P. Rabl, D. DeMille, J. M. Doyle, M. D. Lukin, R. J. Schoelkopf, and P. Zoller, Physical Review Letters **97**, 33003 (2006).

[21] J. Baron, W. C. Campbell, D. Demille, J. M. Doyle, G. Gabrielse, Y. V. Gurevich, P. W. Hess, N. R. Hutzler, E. Kirilov, I. Kozyryev, et al., Science (New York, N.Y.) **343**, 269 (2014).

[22] D. DeMille, S. B. Cahn, D. Murphree, D. A. Rahmlow, and M. G. Kozlov, Physical Review Letters **100**, 023003 (2008).

[23] M. Schnell and G. Meijer, Angewandte Chemie International Edition **48**, 6010 (2009).

[24] K. K. Ni, S. Ospelkaus, D. Wang, G. Quéméner, B. Neyenhuis, M. H. G. de Miranda, J. L. Bohn, J. Ye, and D. S. Jin, Nature **464**, 1324 (2010).

[25] S. Ospelkaus, K. K. Ni, D. Wang, M. H. G. de Miranda, B. Neyenhuis, G. Quéméner, P. S. Julienne, J. L. Bohn, D. S. Jin, and J. Ye, Science (New York, N.Y.) **327**, 853 (2010).

[26] K. K. Ni, S. Ospelkaus, M. H. G. de Miranda, A. Pe'er, B. Neyenhuis, J. J. Zirbel, S. Kotochigova, P. S. Julienne, D. S. Jin, and J. Ye, Science (New York, N.Y.) **322**, 231 (2008).

[27] B. Yan, S. A. Moses, B. Gadway, J. P. Covey, K. R. A. Hazzard, A. M. Rey, D. S. Jin, and J. Ye, Nature **501**, 521 (2013).

[28] S. A. Moses, J. P. Covey, M. T. Miecnikowski, B. Yan, B. Gadway, J. Ye, and D. S. Jin, Science (New York, N.Y.) **350**, 659 (2015).

[29] J. W. Park, S. A. Will, and M. W. Zwierlein, Physical Review Letters **114**, 205302 (2015).

[30] T. Takekoshi, L. Reichsöllner, A. Schindewolf, J. M. Hutson, C. R. Le Sueur, O. Dulieu, F. Ferlaino, R. Grimm, and H.-C. Nägerl, Physical review letters **113**, 205301 (2014).

[31] J. Riedel, S. Hoekstra, W. Jäger, J. J. Gilijamse, S. Y. T. Meerakker, and G. Meijer, The European Physical Journal D **65**, 161 (2011).

[32] S. Hoekstra, M. Metsälä, P. Zieger, L. Scharfenberg, J. Gilijamse, G. Meijer, and S. van de Meerakker, Physical Review A **76**, 063408 (2007).

[33] J. H. Blokland, J. Riedel, S. Putzke, B. G. Sartakov, G. C. Groenenboom, and G. Meijer, The Journal of Chemical Physics **135**, 114201 (2011).

[34] H. Bethlem, G. Berden, F. Crompvoets, R. Jongma, van Roij AJ, and G. Meijer, Nature **406**, 491 (2000).

[35] N. R. Hutzler, H.-I. Lu, and J. M. Doyle, Chemical Reviews **112**, 4803 (2012).

[36] H.-I. Lu, I. Kozyryev, B. Hemmerling, J. Piskorski, and J. M. Doyle, Physical Review Letters **112**, 113006 (2014).

[37] B. Hemmerling, G. K. Drayna, E. Chae, A. Ravi, and J. M. Doyle, New Journal of Physics **16**, 063070 (2014).

[38] T. V. Tscherbul, J. Klos, and A. A. Buchachenko, Physical Review A **84**, 40701 (2011), 1106.1492.

[39] J. Lim, M. D. Frye, J. M. Hutson, and M. R. Tarbutt, Physical Review A **92**, 053419 (2015).

[40] S. van de Meerakker, P. Smeets, N. Vanhaecke, R. Jongma, and G. Meijer, Physical Review Letters **94**, 023004 (2005).

[41] M. Zeppenfeld, B. G. U. Englert, R. Glöckner, A. Prehn, M. Mielenz, C. Sommer, L. D. van Buuren, M. Motsch, and G. Rempe, Nature **491**, 570 (2012).

[42] W. C. Campbell, E. Tsikata, H.-I. Lu, L. D. van Buuren, and J. M. Doyle, Physical Review Letters **98**, 213001 (2007).

[43] M. Hummon, T. Tscherbul, J. Klos, H.-I. Lu, E. Tsikata, W. Campbell, A. Dalgarno, and M. Doyle, John, Physical Review Letters **106**, 053201 (2011).

[44] J. D. Weinstein, R. DeCarvalho, T. Guillet, B. Friedrich, and J. M. Doyle, Nature **395**, 148 (1998).

[45] M. Stoll, J. Bakker, T. Steimle, G. Meijer, and A. Peters, Physical Review A **78**, 032707 (2008).

[46] B. C. Sawyer, B. K. Stuhl, M. Yeo, T. V. Tscherbul, M. T. Hummon, Y. Xia, J. Klos, D. Patterson, M. Doyle, John, and J. Ye, Physical Chemistry Chemical Physics **13**, 19059 (2011).

[47] B. K. Stuhl, M. T. Hummon, M. Yeo, G. Quéméner, J. L. Bohn, and J. Ye, Nature **492**, 396 (2012).

[48] D. DeMille, D. R. Glenn, and J. Petricka, The European Physical Journal D **31**, 375 (2004).

[49] B. K. Stuhl, B. C. Sawyer, D. Wang, and J. Ye, Physical Review Letters **101**, 243002 (2008).

[50] M. D. Rosa, The European Physical Journal D **31**, 395 (2004).

[51] E. S. Shuman, J. F. Barry, D. R. Glenn, and D. DeMille, Physical Review Letters **103**, 223001 (2009).

[52] E. S. Shuman, J. F. Barry, and D. Demille, Nature **467**, 820 (2010).

[53] M. T. Hummon, M. Yeo, B. K. Stuhl, A. L. Collopy, Y. Xia, and J. Ye, Physical Review Letters **110**, 143001 (2013).

[54] J. F. Barry, E. S. Shuman, E. B. Norrgard, and D. DeMille, Physical Review Letters **108**, 103002 (2012).

[55] M. Yeo, M. T. Hummon, A. L. Collopy, B. Yan, B. Hemmerling, E. Chae, J. M. Doyle, and J. Ye, Physical Review Letters **114**, 223003 (2015).

[56] V. Zhelyazkova, A. Cournol, T. E. Wall, A. Matsushima, J. J. Hudson, E. A. Hinds, M. R. Tarbutt, and B. E. Sauer, Physical Review A **89**, 053416 (2014).

[57] J. F. Barry, D. J. McCarron, E. B. Norrgard, M. H. Steinecker, and D. DeMille, Nature **512**, 286 (2014).

[58] D. J. McCarron, E. B. Norrgard, M. H. Steinecker, and D. DeMille, New Journal of Physics **17**, 035014 (2015).

[59] E. B. Norrgard, D. J. McCarron, M. H. Steinecker, M. R. Tarbutt, and D. DeMille, arXiv: 1511.00930 (2015).

[60] T. V. Tscherbul and A. A. Buchachenko, New Journal of Physics **17**, 035010 (2015).

[61] S. K. Tokunaga, W. Skomorowski, P. S. Å»uchowski, R. Moszynski, J. M. Hutson, E. A. Hinds, and M. R. Tarbutt, The European Physical Journal D **65**, 141 (2011).

[62] V. Singh, K. S. Hardman, N. Tariq, M.-J. Lu, A. Ellis, M. J. Morrison, and J. D. Weinstein, Physical Review Letters **108**, 203201 (2012).

[63] J. M. Brown and A. Carrington, *Rotational Spectroscopy of Diatomic Molecules* (Cambridge, 2003).

[64] I. V. Hertel and C.-P. Schulz, *Atoms, Molecules and Optical Physics 2* (Springer Berlin / Heidelberg, 2015).

[65] J. L. Dunham, Physical Review **41**, 721 (1932).

[66] F. Hund, Handbuch der Physik **24**, 561 (1933).

[67] L. A. Kaledin, J. C. Bloch, M. C. McCarthy, and R. W. Field, Journal of Molecular Spectroscopy **197**, 289 (1999).

[68] W. J. Childs, L. S. Goodman, U. Nielsen, and V. Pfeufer, The Journal of Chemical Physics **80**, 2283 (1984).

[69] T. Wall, J. Kanem, J. Hudson, B. Sauer, D. Cho, M. Boshier, E. Hinds, and M. R. Tarbutt, Physical Review A **78**, 062509 (2008).

[70] P. J. Dagdigian, H. W. Cruse, and R. N. Zare, The Journal of Chemical Physics **60**, 2330 (1974).

[71] F. Charron, B. Guo, K. Q. Zhang, Z. Morbi, and P. F. Bernath, Journal of Molecular Spectroscopy **171**, 160 (1995).

[72] Erratum, Journal of Molecular Spectroscopy **176**, 444 (1996).

[73] W. J. Childs, G. L. Goodman, and L. S. Goodman, Journal of Molecular Spectroscopy **86**, 365 (1981).

[74] J. Verges, C. Effantin, A. Bernard, A. Topouzkhanian, A. R. Allouche, J. D'Incan, and R. F. Barrow, Journal of Physics B: Atomic, Molecular and Optical Physics **26**, 279 (1993).

[75] C. M. Gittins, N. A. Harris, R. W. Field, J. Verges, C. Effantin, A. Bernard, J. Dincan, W. E. Ernst, P. Bundgen, and B. Engels, Journal of Molecular Spectroscopy **161**, 303 (1993).

[76] M. Pelegrini, C. S. Vivacqua, O. Roberto-Neto, F. R. Ornellas, and F. B. C. Machado, Brazilian Journal of Physics **35**, 950 (2005).

[77] M. Dulick, P. F. Bernath, and R. W. Field, Canadian Journal of Physics **58**, 703 (1980).

[78] R. A. Frosch and H. M. Foley, Physical Review **88**, 1337 (1952).

[79] C. Foot, *Atomic Physics* (Oxford University Press, 1992).

[80] D. J. Berkeland and M. G. Boshier, Physical Review A **65**, 033413 (2002).

[81] M. E. Gehm, Ph.D. thesis, Duke University (2003).

[82] H.-I. Lu, Ph.D. thesis, Harvard University (2013).

[83] H.-I. Lu, J. Rasmussen, M. J. Wright, D. Patterson, and J. M. Doyle, Physical Chemistry Chemical Physics **13**, 18986 (2011).

[84] H. Ball, M. W. Lee, S. D. Gensemer, and M. J. Biercuk, The Review of Scientific Instruments **84**, 063107 (2013).

[85] D. Budker, D. F. Kimball, and D. P. DeMille, *Atomic physics.* (Oxford University Press, 2004).

[86] D. E. Fagnan, J. Wang, C. Zhu, P. Djuricanin, B. Klappauf, J. Booth, and K. Madison, Physical Review A **80**, 022712 (2009).

[87] Y. Ralchenko, A. E. Kramida, J. Reader, and b. A. S. D. Team, National Institute of Standards and Technology, Gaithersburg, MD (2013).

[88] G. Nave, Journal of Optical Society of America B **20**, 2193 (2003).

[89] W. J. Childs, D. R. Cok, and L. S. Goodman, Journal of Optical Society of America **73**, 151 (1983).

[90] T. Loftus, Ph.D. thesis, University of Oregon (2001).

[91] E. L. Raab, M. Prentiss, A. Cable, S. Chu, and D. E. Pritchard, Physical Review Letters **59**, 2631 (1987).

[92] J. Flemming, A. Tuboy, D. Milori, L. Marcassa, S. Zilio, and V. Bagnato, Optics Communications **135**, 269 (1997).

[93] A. M. L. Oien, I. T. McKinnie, P. J. Manson, W. J. Sandle, and D. M. Warrington, Physical Review A **55**, 4621 (1997).

[94] M. Harvey and A. J. Murray, Physical Review Letters **101**, 173201 (2008).

[95] T. Lindvall, M. Merimaa, I. Tittonen, and A. A. Madej, Physical Review A **86**, 033403 (2012).

[96] J. F. Barry, Ph.D. thesis, Yale University (2013).

[97] J. Kändler, T. Martell, and W. Ernst, Chemical Physics Letters **155**, 470 (1989).

[98] P. M. Sheridan, J.-G. Wang, M. J. Dick, and P. F. Bernath, The Journal of Physical Chemistry A **113**, 13383 (2009).

[99] S. F. Rice, H. Martin, and R. W. Field, The Journal of Chemical Physics **82**, 5023 (1985).

[100] H. Williams, *Private conversation.*

[101] G. Quéméner and J. L. Bohn, arXiv: 1510.06601 (2015).